
Thermally-driven Circulation and Convection over a Mountainous Tropical Island

by Chun-Chih Wang, Dept. of
Atmospheric and Oceanic Science,
McGill University, Montreal

supervised by Prof. Daniel Kirshbaum
Assistant Professor

July, 2014

A thesis submitted to McGill University in partial fulfillment of the requirements
of the degree of Master of Science
© Chun-Chih Wang, 2014

Contents

Abstract	iii
Acknowledgement	vi
List of Figures	vii
List of Tables	viii
List of Equations	ix
Abbreviations	ix
Symbols	x
1. Introduction	1
1.1 Overview	1
1.2 Dynamics of atmospheric convection	2
1.2.1 Conditional instability	3
1.2.2 Potential instability	4
1.2.3 Entrainment with Unsaturated Surrounding	5
1.3 Topographically-induced convection	6
1.3.1 Mechanical lifting	7
1.3.2 Obstacle effects	8
1.3.3 Thermal lifting	9
1.3.3.1 Elevated heating over mountains	9
1.3.3.2 Sea/land breezes	13
1.4 Cloud and precipitation feedbacks	15
1.4.1 Cloud shadowing	15
1.4.2 Cloud latent-heat release	16
1.4.3 Precipitation	17
1.5 Motivation	17
2. DOMEX Observations	20
2.1 Datasets	20
2.1.1 Field campaign data	20
2.1.2 Operational data	23
2.2 Overview of DOMEX observations	24
2.3 Analysis of thermally-driven events	26
2.4 Conclusions from the observations	42

3. Numerical Simulations	43
3.1 Model description	43
3.2 Model verification	46
3.2.1 General description	46
3.2.2 Surface verification	50
3.2.3 Flight track comparison	53
3.3 Mechanical vs. thermal forcing	58
3.4 Background wind velocity	65
3.5 Cloud and precipitation feedbacks	70
3.6 Cloud layer stability	74
3.7 Heat-engine theory	79
4. Conclusion	86
Appendix	xii
A1. Island-scale horizontal divergence	
A2. Vertically-integrated island-scale horizontal mass flux	
A3. Integrated vertical cloud mass flux	
Bibliography	xiv

Abstract

Observational data from the 2011 Dominica Experiment (DOMEX) and cloud-resolving numerical simulations are exploited in order to acquire a better understanding of controlling parameters of thermally-driven circulation and convection over a mountainous tropical island. Four weak (<4 m/s) background wind days are investigated to obtain a preliminary diagnosis of the conditions favorable for diurnally-forced shallow cumulus convection over the island. The observations suggest that the degree of solar heating before the first cumulus development largely controls the amount of low-level forcing and the vigor of shallow cumulus, rather than the moist stability of the background flow.

A “golden” case from DOMEX with a clear diurnal cycle in cumulus convection is studied using quasi-idealized numerical simulations (with full model physics and a realistic terrain profile) to better understand the mechanisms and sensitivities of island thermal circulations and cumulus convection. Simulations at different grid spacings reveal that large-eddy grid spacing (~ 100 m) provides the most accurate representation of the in-situ measurements from DOMEX and other observations. Sensitivity tests reveal that mechanical forcing played little role in convection initiation on this day since the Froude number (Fr) was < 1 . Surprisingly, even though thermal circulations develop earlier over a mountainous island, they are ultimately weaker than those over a flat island possibly due to their elevated outflows undergo stable descent over a high terrain. Background wind velocity also has a significant impact on thermal circulations, which tend to weaken as the cross-barrier wind increases. Cloud shadowing and precipitation both have a negative feedback on thermal circulations, with the former being the stronger mechanism. In addition, cloud latent-heat release over the island strengthens thermal circulations, which also explains why circulations intensify when cumulus vigor is enhanced by greater moist instability.

The simulations allow for the evaluation of thermal-circulation-strength predictions from thermodynamic heat engine theory. While the theory predicts the strength of thermal circulations reasonably well over a mountainous terrain, it fails to capture the sensitivity to terrain height likely because its assumption that the entire circulation is confined within the mixed layer is invalid.

Des données d'observations de l'expérimentation Dominicaine (DOMEX, 2011) et des simulations de model atmosphérique sont exploités dans le but d'acquérir une meilleur compréhension des paramètres contrôlant la circulation et la convection thermique au dessus d'une ile tropicale montagneuse. Quatre jours de vent faible (<4 m/s) sont analysés afin d'obtenir un diagnostic préliminaire des conditions favorable au développement de cumulus de convection peu profonde généré par forçage thermique diurne au dessus de l'île. Les observations montrent que l'augmentation de la température dut au radiation solaire précédent le développement du cumulus contrôle largement le forçage de basse altitude ainsi que la vigueur du cumulus. la stabilité du courant global joue un role moins important.

Une étude de cas provenant de DOMEX montrant clairement un cycle diurne de formation de cumulus par convection a été spécialement sélectionné pour être étudié avec des simulations numérique quasi-idéalisé (avec l'ensemble des équations atmosphérique du model ainsi qu'une représentation réaliste du profil topographique) afin de mieux comprendre les mécanismes et sensibilités de la circulation thermique générée par l'île ainsi que la formation de cumulus par convection. Les résultats de simulations utilisant différentes résolutions ont révélé que les représentations les plus fidèle aux observations de DOMEX sont obtenues lors de simulations à haute résolution horizontale (~ 100 m). Des tests de sensibilité réalisés montrent que le forçage mecanique joue un rôle mineur dans l'initiation de la convection lors de ce cas où le nombre de Froude (Fr) était < 1 . Etonament, même si la circulation thermique se développe plus tôt au dessus de l'île montagneuse, Elle est toujours plus faible qu'au dessus de l'île plate, cela peut être expliqué par le fait que les ecoulements de haute altitude subissent une stable descente au-dessus de terrain élevé. La vitesse du vent global a un impact non négligeable sur les circulations thermique, cette dernière tend a s'affaiblir alors que le courant horizontal au sommet de la topographie accélère.. La couverture nuageuse et les précipitations affaiblisse tous les deux la circulation thermique, bien que le premier mécanisme soit le plus efficace. En plus, le relâchement de chaleur latente par le nuage au dessus de l'île renforce la circulation thermique, ce qui explique également pourquoi la circulation s'intensifie lorsque l'activité du cumulus s'accélère , qui est dans ce dernier cas généré par une plus grande instabilité de l'air humide.

Les simulations permettent la comparaison des prédictions de la puissance de la circulation thermique avec celle réalisée grâce à la théorie de l'engin de chaleur thermodynamique. Alors que la théorie prédit relativement bien la circulation thermique au dessus d'une région montagneuse, elle ne capture pas la sensibilité due à l'élévation de la topographie, sûrement car l'hypothèse que la totalité de la circulation est confinée dans la couche homogène est invalide.

Acknowledgements

First of all I would like to thank my supervisor, Prof. Daniel (Dan) Kirshbaum, for providing me such a great opportunity to learn from this research experience. I truly appreciate the amount of time he devoted to explain difficult scientific, computational, and numerical concepts to me, which would definitely benefit me during my future career. In addition, I appreciate his help with modifying the codes for our numerical simulations. Most importantly, as a student new to the field of scientific research, I want to thank him for his helpful guidance on scientific writing. Last but not least, I would also like to thank him (and Michael Havas) for providing me the necessary computing resources to complete my project.

I would also like to thank Prof. Ron Smith of Yale and Prof. Justin Minder of SUNY-Albany for their involvement in the 2011 DOMEX field campaign. My research would never be possible without the data provided by them and other project investigators of the field campaign.

Finally, I want to shout out big thanks to my family and friends, both at McGill and Penn State, for encouraging and guiding me through the difficult times. It would have been a far less enjoyable MS.c career if you guys were not there for me. Thanks Thomas for translating the abstract to French. Thank You Xiaoli, Sisi, and Ya-Chien, for celebrating all of the Chinese festive holidays together. I look forward to keep the tradition going as I continue onto Ph.D here at McGill.

List of Figures

1.1	Schematic of convection initiation or enhancement as a conditionally unstable flow undergoes mechanically-forced ascent along an orography, taken from Houze Jr. (2012)	7
1.2	Streamlines around a 3-D orography in a low Fr regime with no solar heating, taken from Smolarkiewicz and Rotunno (1989)	8
1.3	Schematic cross-section of thermally-driven circulations over a heated mountain under weak large-scale winds, taken from Demko et al. (2009)	11
1.4	Schematic diagrams illustrating the effects of wind velocity on the initiation location of convective storms during the 2007 COPS, taken from Hagen et al. (2011)	13
1.5	Map of the Caribbean and geographies of Dominica, b. and c. taken from Kirshbaum and Smith (2009)	19
2.1	A map of the DOMEX field campaign instrument setup and WKA aircraft flight, taken from Smith et al. (2012)	21
2.2	DOMEX observations during RF13 taken from Smith et al. (2012)	25
2.3	DOMEX observations during RF07 taken from Smith et al. (2012)	26
2.4	Skew-T soundings from the four DOMEX weak trade-wind cases.	28
2.5	Selected satellite images for the four DOMEX weak trade-wind cases at 10, 13, 16, and 19 UTC	29
2.6	WCR reflectivity and Doppler vertical velocity along selected legs of the four DOMEX weak trade-wind cases	31
2.7	Radar-derived accumulated rainfall ending at 21 UTC	32
2.8	An illustration of procedures for constructing the sea-level pressure time-series at the ocean sounding site.	35
2.9	FWL observations during the four DOMEX weak trade-wind cases.	37
3.1	Diurnal evolution of the first model-level horizontal winds, first model-level flow divergence, and vertically-integrated cloud water mixing ratio from the 250-m grid spacing control simulation	47
3.2	First model-level horizontal winds, first model-level flow divergence, and cloud liquid water path from the four control simulations of different grid spacings at 18 UTC	49
3.3	Simulated 2-m horizontal winds and 0.01 g kg ⁻¹ isosurfaces of cloud water mixing ratio from the four control simulations at 18 UTC	50
3.4	Simulated surface conditions at Freshwater Lake from the four control simulations plotted against the observations	51
3.5	Simulated surface conditions at Melville Hall airport from the four control simulations plotted against the observations	52
3.6	Simulated vertical velocity variance averaged separately along all Leg 3s and Leg 4s for the whole simulation.	54
3.7	First model-level horizontal winds, first model-level flow divergence, and cloud liquid water path from the four control simulations at 17 UTC	56

3.8	First model-level horizontal winds, flow divergence, and cloud liquid water path for the pure mechanical forcing vs. pure thermal forcing sensitivity test at 12 UTC	59
3.9	Simulated WKA flight level flow and cloud parameters for the pure mechanical forcing vs. pure thermal forcing sensitivity test	61
3.10	First model-level horizontal winds, first model-level flow divergence, and cloud liquid water path from the 250-m grid spacing control and pure thermal forcing simulations at 14 UTC	62
3.11	3-hrly. island-scale horizontal mass flux profile from the pure mechanical forcing vs. pure thermal forcing sensitivity tests	64
3.12	First model-level horizontal winds, first model-level flow divergence, cloud liquid water path for the wind-sensitivity test at 18 UTC	66
3.13	Simulated WKA flight level flow and cloud parameters for the wind sensitivity test	68
3.14	First model-level horizontal winds, first model-level flow divergence, cloud liquid water path for the moist convection feedbacks sensitivity test at 18 UTC	71
3.15	Simulated WKA flight level flow and cloud parameters for the cloud and precipitation feedbacks sensitivity tests	72
3.16	Simulated WKA flight level flow and cloud parameters for the cloud layer stability sensitivity test	76
3.17	Locations of vertical cross-sections for the simulated circulation strength diagnosis	80
3.18	A schematic diagram of representative thermal circulation strength diagnosis from the simulation	81
3.19	Simulated Island and ocean surface air temperatures, island-averaged mixed layer height, and simulated vs. heat-engine predicted thermal circulation strength for the heated mountain case without microphysics parameterization	83
3.20	Simulated Island and ocean surface air temperatures, island-averaged mixed layer height, and simulated vs. heat-engine predicted thermal circulation strength for the flat island case without microphysics parameterization	84
3.21	First model-level horizontal winds and flow divergence for the flat island case without microphysics parameterization at 15 UTC	84
3.22	Perturbation wind and potential temperature along one of the cross-sections from the mountain and flat-island no microphysics cases	85
A1.	Dominica's 1-m elevation contour as represented in the simulations	xii
A2.	A schematic illustration of the 1-m elevation contours at every model level above Dominica	xiii

List of Tables

2.1	Upstream flow conditions during the four DOMEX weak trade-wind cases	27
2.2	A summary of FWL surface observations for the four DOMEX weak trade-wind cases	37
2.3	Input parameters of heat-engine theory	39

2.4 WKA Legs 3 and 4 measurements from the four DOMEX weak trade-wind cases	41
3.1 Observed vs. simulated Leg 3 flow and in-cloud measurements in four different grid spacings	55
3.2 Observed vs. simulated Leg 4 flow and in-cloud measurements in four different grid spacings	55
3.3 Maximum and averaged island rainfall from the four control simulations compared to the Guadeloupe radar-derived rainfall	57
3.4 Maximum and averaged island rainfall, time-integrated horizontal mass flux up to the lowest level of non-divergence, and time-integrated WKA flight-level vertical cloud mass flux for the pure mechanical forcing vs. pure thermal forcing sensitivity test	63
3.5 Maximum and averaged island rainfall, time-integrated horizontal mass flux up to the lowest level of non-divergence, and time-integrated WKA flight-level vertical cloud mass flux for the wind sensitivity test	69
3.6 Maximum and averaged island rainfall, time-integrated horizontal mass flux up to the lowest level of non-divergence, and time-integrated WKA flight-level vertical cloud mass flux for the cloud and precipitation sensitivity test	72
3.7 Maximum and averaged island rainfall, time-integrated horizontal mass flux up to the lowest level of non-divergence, and time-integrated WKA flight-level vertical cloud mass flux for the cloud layer stability sensitivity test	77

List of Equations

1.1 Vertical momentum equation	2
1.2 Definition of buoyancy	2
2.1 Z-R relationship for the Meteo France radar on Guadeloupe	32
2.2 Hypsometric equation	34
2.3 Non-adiabatic temperature difference between Freshwater Lake and the ocean sounding site	39
2.4 Heat-engine theory predicted thermal circulation strength	39
2.5 Distance-normalized vertical cloud mass flux along the flight legs	42
3.1 Square of the Brunt-Vaisala frequency for the mixed layer height calculation	81
A1. Divergence theorem	xiii
A2. Vertically-integrated island-scale horizontal mass flux	xiv
A3. Vertical cloud mass flux	xiv

Abbreviations

PGF	pressure gradient force
LCL	lifting condensation level

LFC	level of free convection
LNB	level of neutral buoyancy
CAPE	convective available potential energy
CIN	convective inhibition
LES	large-eddy simulation
FWL	Freshwater Lake
MH	Melville Hall
TFFR	Guadeloupe
TFFF	Martinique
WKA	Wyoming King Air research aircraft
WCR	Wyoming Cloud Radar
UTC	Universal Standard Time
LST	local standard time
SLP	sea-level pressure
PBL	planetary boundary layer

Symbols

Fr	Froude number
N	Brunt-Vaisala frequency
h	terrain height
U	horizontal wind speed
B	buoyancy
g	gravitation acceleration
W (w)	vertical velocity
ρ	air density
q	mixing ratio
T	temperature
θ	potential temperature
θ_e	equivalent potential temperature
R	rain rate
σ_w^2	vertical velocity variance

σ_{cld}	cloud fraction
T_{NA}	non-adiabatic temperature
F_{S}	solar radiation flux
M_{v}	integrated vertical cloud mass flux
M_{h}	vertically-integrated island-scale horizontal mass flux
δ	divergence
F_{δ}	convergence fraction

Chapter 1. Introduction

Section 1.1 Overview

The interaction between atmospheric flow and the Earth's complex terrain has been studied for many decades. It is well documented that regional flow, cloud, and precipitation patterns are heavily influenced by the presence of orography (Banta, 1990). Concerning precipitating systems in particular, orography not only triggers heavy precipitation but also enhances the precipitation associated with larger-scale processes such as mesoscale convective systems, synoptic fronts, and tropical cyclones (Houze Jr., 2012). As a consequence, mountainous regions are prone to flash flooding (particularly in narrow watershed catchments), which may lead to significant life and property losses. Thus, understanding the effects of orography on precipitation is critical for forecasting and mitigating flash floods, landslides and other hydro-meteorological hazards.

The dynamical response of an impinging airflow to orography under a weak diabatic heating situation is often diagnosed using the Froude number, $Fr=U/Nh$, where U is the background wind speed, N is the Brunt-Vaisala frequency, and h is the terrain height (Smolarkowicz and Rotunno, 1989; Tian and Parker, 2003). However, in the absence of cloud cover, solar insolation heats the Earth's land surface, which in turn warms the air immediately above it. The resulting buoyancy gradient introduces additional flow dynamics that Fr cannot explain entirely. These dynamics, which have largely been studied in very idealized settings, are only partially understood. In this study, we investigate the dynamics and controlling parameters of thermally-driven flow and associated cumulus convection over a heated, mountainous topography.

Section 1.2 Dynamics of atmospheric convection

Before we discuss the orography's effect on atmospheric convection, we briefly review the basics of atmospheric convection. Atmospheric convection is a form of turbulent motion that arises from the heterogeneity in the horizontal and vertical density fields. The vertical momentum equation in an inviscid atmosphere with hydrostatically-balanced basic state

$$\frac{dw}{dt} = -\frac{1}{\rho} \frac{\partial p'}{\partial z} + B \quad (1.1)$$

where the first and second terms on the right hand side are the vertical perturbation pressure gradient force (PGF) and buoyancy force respectively, shows that the buoyancy force completely determines a parcel's vertical acceleration in the absence of vertical PGF. The buoyancy force B is

$$B = -g\left(\frac{\rho'}{\rho}\right) \quad (1.2)$$

where $\bar{\rho}$ is the basic state density and $\rho' = \rho - \bar{\rho}$ is the parcel's density perturbation from the basic state (i.e surrounding) density. By ideal gas law, a warm and moist parcel tends to be less dense than a cool and dry parcel at the same pressure. Applying this to Eq. 1.1, a warm and moist parcel tends to accelerate upward since it tends to be less dense than its surroundings ($\rho' < 0$) or, in other words, 'positively buoyant'. The vice-versa is true for a dry, cool and relative dense ($\rho' > 0$) or 'negatively buoyant' parcel.

Static stability measures the potential for buoyancy to accelerate a vertically perturbed parcel away from its initial position. In a statically stable (unstable) atmosphere, a parcel will return to (accelerate away from) its original state after vertically displaced,

since the buoyancy force acting on the parcel opposes (coincides) the direction of the vertical displacement.

Static stability is controlled by the parcel's density relative to its surrounding environment. When a parcel is lifted from its initial position, it cools and expands. The rate of cooling, which may be predicted from the First Law of Thermodynamics (Rogers and Yau, 1989), depends on whether the parcel is saturated. An unsaturated air parcel cools at the dry-adiabatic lapse rate ($\sim 10 \text{ K km}^{-1}$) while a saturated parcel cools moist-adiabatically. Latent-heat release due to condensation renders the moist-adiabatic lapse rate smaller than the dry-adiabatic lapse rate. The difference between them depends on the amount of water vapor in the air, which is controlled by the Clausius-Clapeyron equation (Bohren and Albrecht, 1998). This equation shows that warmer air is able to hold more water vapor, hence the moist and dry adiabatic lapse rate differ the most at higher temperatures.

A layer of atmosphere is absolutely unstable (stable) if its lapse rate is greater (less) than the dry-adiabatic (moist-adiabatic) lapse rate. In absolutely unstable situations, an upward-displaced parcel becomes positively buoyant, which causes the air parcel to accelerate away from its initial position, regardless of saturation. Two other types of static instability that exclusively apply to saturated air parcels are discussed in subsections 1.2.1 and 1.2.2.

1.2.1 Conditional Instability

A layer of atmosphere is conditionally unstable if its lapse rate falls between the dry and moist lapse rates. In this case, the environment is stable in respect to unsaturated vertical displacements, but unstable in respect to saturated vertical displacements

(Markowski and Richardson, 2010). Consider an unsaturated parcel lifted by an external force that initially cools dry-adiabatically. Since the environmental lapse rate is less than the dry-adiabatic lapse rate, the parcel becomes colder and denser than its environment. Therefore, the parcel is negatively buoyant and tends to decelerate unless the lifting is sustained by an external force. If parcel is brought to the lifting condensation level (LCL), its lapse rate then becomes moist-adiabatic. Since the moist-adiabatic lapse rate is less than the environmental lapse rate, the parcel gains positive buoyancy with further lifting parcel until its buoyancy returns to zero at the level of free convection (LFC). The integrated negative buoyancy that a parcel needs to overcome before becoming neutrally buoyant at the LFC is known as the convective inhibition (CIN).

Once above the LFC, additional ascent of the parcel creates a positive buoyancy force that propels the parcel freely away from its original position, leading to the release of conditional instability. The vertical acceleration ceases when the parcel's buoyancy becomes zero again at the level of neutral buoyancy (LNB). The amount of integrated positive buoyancy force that a parcel gains between the LFC and LNB is known as the convective available potential energy (CAPE). Deep convection occurs more frequently under high CAPE environments because a large amount of positive buoyancy is available to drive the parcel high up into the atmosphere. However, this occurs only if there is sufficient external lifting to overcome the CIN.

1.2.2 Potential Instability

Potential instability is another form of moist instability, which arises from the bulk lifting of an atmospheric layer. A layer is defined as potentially unstable if its equivalent potential temperature, often thought as the maximum temperature an air parcel

would have if all the water vapor were to condense and release latent heat and then warms dry-adiabatically in a descent down to a reference pressure level, decreases with height. A potentially unstable layer might be absolutely stable initially but exhibits a vertical relative humidity gradient such that the bottom is more humid than the top. If lifted by an external force, the bottom of this layer saturates first. Further ascent cools the lower part of this layer moist-adiabatically, while the unsaturated top cools dry-adiabatically. Since dry-adiabatic lapse rate is greater than the moist-adiabatic lapse rate, the lapse rate increases within this layer. The final result of this bulk lifting leads to the conversion of an absolutely stable atmospheric layer into a conditionally unstable one where saturated parcels within this layer can ascend freely.

1.2.3 Entrainment with Unsaturated Surrounding

Entrainment is the mixing of environmental air into a cloud parcel. During this process, the buoyancy of the saturated parcel is decreased due to dilution with the environmental air (Bohren and Albrecht, 1998). In addition, the parcel's buoyancy decreases through evaporative cooling of liquid hydrometeor (Paluch, 1979). Thus, the overall effect of entrainment is to reduce a saturated parcel's buoyancy by reducing its density contrast with the surrounding, which potentially limits their ability to ascend high into the troposphere (Rogers and Yau, 1989; Markowski and Richardson, 2010).

Cumulus entrainment has been studied for many decades. The earliest views on cumulus entrainment treated a cloud parcel as a rising plume or blob, where environmental air is homogeneously entrained into the cloud. In these models, the rate of entrainment is directly proportional to the cloud's vertical velocity and inversely proportional to the cloud radius (Morton et al., 1956; Squires and Turner, 1962). Thus,

larger clouds are more capable of fighting off buoyancy reduction associated with entrainment mixing than smaller clouds. However, due to their gross assumptions, these models fail to produce liquid water content profiles observed within cumulus clouds (Blyth, 1993). Thus, they are largely disputed today.

Squires (1958) proposed cloud-top entrainment that briefly replaced the plume or blob entrainment as the dominant entrainment mechanism (Blyth, 1993; de Rooy et al., 2013). Instead of unsaturated air being laterally entrained into the cloud at the cloud edges, unsaturated air is entrained at the cloud summit. Evaporative cooling associated with cloud-top entrainment generates negatively buoyant downdrafts that penetrate into the rising cloud parcel, which further dilutes its buoyancy. However, disagreements remain regarding how these downdrafts are generated, how far these downdrafts penetrate into the cloud, and how these downdrafts trigger subsequent mixing with the environment. To better understand the entrainment processes, Large-Eddy Simulations (LES) have been used to study the entrainment process using a bulk mass-flux framework (e.g Siebesma et al., 2003). Preliminary results suggest that cloud-top entrainment does not play a significant role in the mixing process compared to lateral entrainment, at least in shallow cumulus clouds (Heus et al., 2008).

Section 1.3 Topographically-induced convection

In the planetary boundary-layer, there are numerous forces that lift air parcels or a layer of atmosphere to saturation so that instability may be released. The passage of a synoptic cold front is a common example. When the air ahead of the cold front is conditionally unstable, deep convection can occur as denser cold air behind the front

undercuts the warm, moist air ahead of it (Houze and Hobbs, 1982). Other than atmospheric boundaries such as fronts, orography also acts as a source of vertical motion to release static instability. The orographically-induced vertical motion can come from either, 1) mechanical lifting of air flow over an orography, 2) obstacle effects around an orography, and/or 3) thermally-driven circulation over a heated terrain (Banta, 1990). We devote this section to the discussion of each topographically-forced convective mechanism.

1.3.1 Mechanical lifting

For a stratified flow approaching a 3-D obstacle such as an orography, if Fr is greater than unity (> 1), the combination of weak stability, strong background wind speeds, and shallow obstacle height allows the flow to easily climb over the obstacle. In addition to gravity waves, downslope windstorms, and rotors (Doyle and Durran, 2002), vigorous convection can erupt over windward slope of an obstacle if the flow is conditionally unstable (Fig. 1.1, Houze Jr., 2012; Miglietta and Rotunno, 2012).

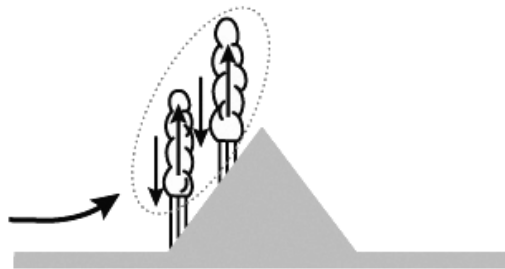


Figure 1.1. Schematic of convection initiation or enhancement as a conditionally unstable flow undergoes mechanically-forced ascent along an orography (from Houze Jr., 2012).

Convection initiated by the mechanical lifting of conditionally unstable air over a mountain's windward slope has caused several historic flooding events, such as the Rapid City flood of 1972 over Black Hills of South Dakota (Maddox et al., 1978) and Big Thompson flood of 1976 in eastern Colorado (Caracena et al., 1979). In both of these

events, the upstream soundings indicated the presence of high conditional instability with a very moist low-level flow capped below a stable inversion layer. Prevailing synoptic setups during these events allowed the low-level flow to impinge against the slopes of Black Hills or Rocky Mountains. As a consequence, low-level flow was mechanically-lifted up to the LFC by the orography, which resulted in intense convective storms that produced large rain accumulations (Maddox et al., 1978).

1.3.2 Obstacle effects

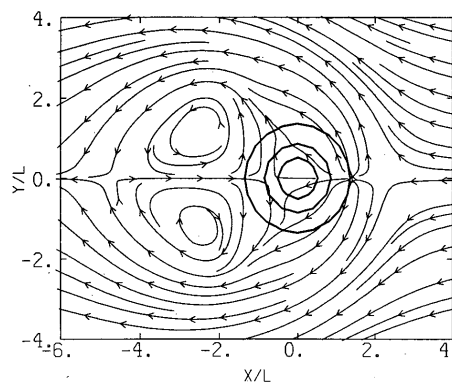


Figure 1.2. Streamlines around a 3-D orography in a low Fr regime with no solar heating. Note that the flow splits upstream of the obstacle (at $X/L \sim 2$) and converges downstream (at $X/L \sim 4$). Opposing leewortices also form downstream of the orography. (from Smorlarkiewicz and Rotunno, 1989)

In cases where $Fr < 1$ and thermal-forcing is relatively weak, a stratified flow approaching a 3-D orography does not obtain enough kinetic energy to overcome the potential energy required to lift it over the orography (Lin, 2007; Markowski and Richardson, 2010). Similar to mechanical lifting regimes, the flow decelerates as it approaches the orography. However, since it is not able to ascend over the windward slope, the flow splits around the orography instead. The split flows then converge downstream of the orography (Fig. 1.2, Smorlarkiewicz and Rotunno, 1989). Rising motions are generated within the flow stagnation zone upstream and within the convergence zone downstream of the orography (Houze Jr., 2012). These vertical

motions provide the lifting mechanism for convection initiation when the impinging flow is conditionally unstable.

Convection initiation and precipitation enhancement due to upstream flow blocking or downstream flow convergence have been observed on numerous occasions (Watanabe and Ogura, 1987; Chen and Nash, 1994; Rotunno and Ferretti, 2001). The rain bands that form upstream of the Hawaii islands are a result of upstream ascent in a blocked flow lifting moist parcels to saturation (Leopold, 1949; Smolarkewicz et al., 1988; Chen and Nash, 1994). Watanabe and Ogura (1987) attributed a heavy rainfall event over western Japan to the upstream blocking of moist flow that was associated with a synoptic front. Unlike in $Fr > 1$ regimes, the greatest accumulation occurred along the coastline instead of over the mountain slopes. Extreme rainfall associated with flow blocking upstream of an orography was also studied during the Mesoscale Alpine Program (MAP, Rotunno and Ferretti, 2003). Numerical simulations show that the stable air that banked up against the eastern Alps during MAP-IOP8 acted as an 'effective mountain' that forced moist low-level flow upward; shifting the precipitation zone to well upstream of the mountain range.

1.3.3 Thermal lifting

1.3.3.1 Elevated heating over mountains

The convective mixing of sensible surface heating warms the air immediately above a heated terrain. Thus, parcels that lie on an elevated warm surface will heat up faster than the air that is detached from this elevated heat source. The temperature difference generates positive buoyancy within the parcels over the heated terrain, which results in a pressure gradient that drives upslope (anabatic) flows along the mountain

slope (Aitkinson, 1981; Banta, 1984; Whiteman, 2000). Rising motions are frequently found in narrow convective cores embedded within the upslope flows. However, the strongest rising motions are generated as the upslope flows converge over the mountain summit (Raymond and Wilkening, 1980; Banta, 1990). Recent studies have quantified this upslope convergence using the divergence theorem (see Appendix for a similar calculation in this study) and the wind data around a closed perimeter surrounding a mountain feature (e.g. Geerts et al. 2008; Demko et al. 2009). Such studies found that flow convergence developed soon after sunrise and gradually strengthened as the sensible heat flux increased.

After the upslope flows converge, the intense updrafts formed spread outward below a statically stable free atmosphere, forming return flows which diverge above the heated terrain as shown by research flight loops (e.g. Raymond and Wilkening, 1980; Damiani et al., 2008). Toroidal circulations are formed when thermally-driven flows trace out complete loops on each side of the orography (Demko et al., 2009. Fig. 1.3). As solar flux wanes in the evening, radiative cooling over a mountain slope creates a local negative buoyancy anomaly, which results in mesoscale descent and downslope (katabatic) winds. As result, the circulations switch signs such that the flows descend aloft the mountain peak and diverge down the slopes.

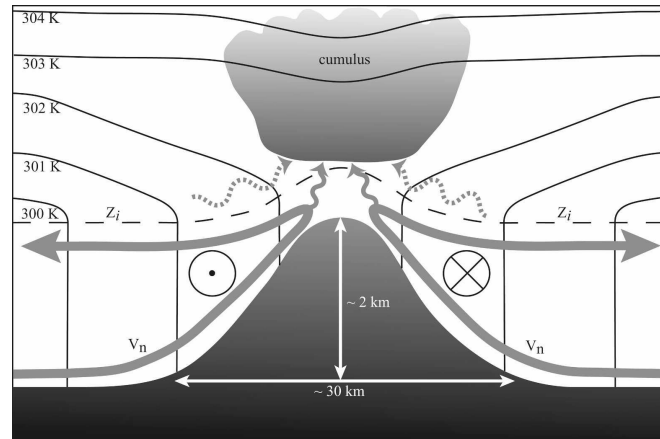


Figure 1.3. Schematic cross-section of thermally-driven circulations over a heated mountain under weak large-scale winds. The black solid lines represent the potential temperature, the dashed line denotes the convective boundary-layer depth (Z_i), and the thick gray lines (V_n) are the upslope flow normal to the slope. The two circles show the horizontal vorticity of the thermally-driven flow, pointing outward (left) and pointing inward (right). Note that parts of the upslope flows are feeding into the cumulus convection as they converge above the summit, while the cumulus also draws in air from above the convective boundary-layer (from Demko et al., 2009).

Moist convection initiates when there is sufficient boundary-layer moisture and conditional instability for the mountain lifting to release it. Convection initiation over a heated orography has been studied in several observational studies (e.g. Raymond and Wilkening, 1980; Banta, 1984; Damiani et al., 2008). Typically, shallow cumulus and cumulus congestus form in the morning as thermally-driven updrafts lift moist air parcels to the LCL. As the updrafts intensify with the strengthening upslope flow convergence, the air parcels may gain enough vertical momentum to reach the LFC. Deep cumulonimbi can erupt if the saturated air parcels breach the LFC and ascend high into the atmosphere. The resulting cumulonimbi then propagate in the direction of the ambient ridge-top winds, hence the maximum precipitation is normally found just downwind of a summit (Johnson et al. 2008; Barthlott et al., 2011).

Numerous numerical studies also have been carried out to investigate the effects of various environmental factors on thermally-forced flow and convection over heated terrains (e.g Banta, 1986; Tian and Parker, 2002; Yang et al., 2005; Yang and Chen,

2008). One of the factors governing the strength of the thermally-driven flow is the surface heat budget. Soils containing abundant moisture have a larger latent heat flux and a lower sensible heat flux (Banta, 1990). Therefore, weaker thermally-driven flows develop over moist land surfaces such as forests, whereas stronger flows typically form above dry, bare slopes. This effect has a significant impact on convection initiation over a heated terrain. While using convective-scale ensemble simulations to study the sensitivity of convective precipitation to various perturbed initial conditions, Hanley et al. (2011) found that most of their ensemble members failed to produce any storm. They attributed the lack of convection initiation in their numerical simulations to the 2-4 g kg⁻¹ of boundary-layer mixing ratio deficiency, which was partly caused by the inaccurate representation of soil moisture. As result, the simulated thermal-circulation grew too strong, which entrained large amounts of dry air into the boundary layer and limited storm initiation. After correcting for this moisture deficiency, some ensemble members produced realistic deep convective storms over the high terrains.

Background wind speed and direction also have been studied as potential factors controlling the thermally-driven flows. Tian and Parker's (2002) numerical simulations show that stronger winds tend to weaken thermally-driven eddies over the summit. This agrees with the result from Banta's (1986) numerical study, which noted a weakening trend in thermally-driven eddies with increasing background wind speed. Kirshbaum (2013) attributed this simulated convection weakening to the ventilation of heat away from the ridge top by the stronger background winds. The location of storm initiation is also sensitive to the background wind speed and direction. During the 2007 Convective and Orographically induced Precipitation Study (COPS) campaign, Hagen et al. (2011)

found that on days with light wind speed ($< 5 \text{ m s}^{-1}$) below 925-hPa, storms initiated directly over the mountains of Germany's Black Forest region due to upslope flow convergence. In contrast, on days with stronger, unidirectional winds at all levels, convection initiated downwind of the ridge tops as a result of valley flow convergence downstream (Fig. 1.4).

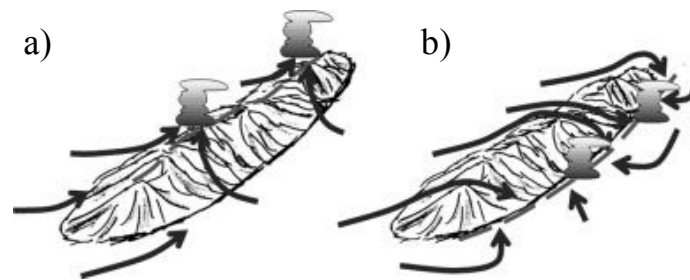


Figure 1.4. Schematic diagrams illustrating the effects of wind velocity on the initiation location of convective storms during the 2007 COPS: a) a weak wind case and variable vertical wind shear, b) a strong wind case with unidirectional vertical wind shear (from Hagen et al., 2011).

1.3.3.2 Sea/land breezes

Heat capacity controls how fast a surface warms for a given amount of energy input. For a given amount of incoming solar radiation, a surface with a low heat capacity tends to warm faster than a surface with a high heat capacity. Over an island, since the land surface has a lower heat capacity, it warms faster than the adjacent water body during daytime. Thus, more sensible heat flux is produced over the island, which causes air over the island to become warmer than air over the water body. The resulting temperature contrast induces a pressure gradient that forces air over the water to flow toward the land surface, creating a sea breeze. The opposite occurs at night, as air over the colder land surface flows toward the warmer water body, creating a land breeze. A zone of strong vertical velocity is found near the sea/land breeze front as the denser cold air undercuts lighter warm air ahead of the front (Neumann and Mahrer, 1971; Atkinson, 1981). This zone of strong vertical motion provides the lifting mechanism to bring

conditionally unstable air parcels to the LFC. This zone of strong upward velocity is greatly enhanced if two seabreeze fronts collide with each other (Abe and Yoshida, 1982). Sea breeze fronts and associated cold pool collision zones are thought to be favorable regions for mesoscale convective system (MCS) initiation (Carbone et al., 2000).

Numerous numerical studies have been conducted to quantify the strength and understand the controlling parameters of sea/land breeze fronts (e.g. Segal et al., 1988; Xian and Pielke, 1991; Savijarvi and Matthews, 2004). The background winds again play a major role in controlling this type of thermally-driven flow. Miller et al. (2003) found that an offshore background wind tightens the temperature gradient across the front, which intensifies the sea breeze's strength. The opposite is true for an onshore background wind. The optimal condition for sustaining strong thermally-induced vertical motions near a seabreeze front is achieved when the offshore background wind completely stalls the seabreeze front's inland propagation (Arritt, 1993). However, since the heated land surface also continuously warms the air behind the sea breeze front, the post-frontal cold air advection becomes crucial for sustaining the temperature contrast. Robinson et al. (2013) found that the front is sustained only if the flow behind the front is at least three times greater than the front's inland propagation speed. Otherwise, without cool marine air being advected into the front, surface warming quickly destroys the temperature gradient across it.

Coastal orography also has been found to have significant impact on sea/land breeze fronts. In a mountainous coastal region, thermally-driven upslope (downslope) winds formed in response to elevated heating (cooling) combine with sea breeze (land breeze) to produce overall stronger anabatic (katabatic) flows (Mahrer and Pielke, 1977;

Barthlott and Kirshbaum, 2013). However, Qian et al. (2012) found that only the strength of simulated land breeze is increased with the presence of a steep inland topography (e.g. a plateau). Daytime sea breeze is blocked near the terrain's foothill, creating a deep cold pool along the coast. This cold pool is further strengthened during nighttime and propagates offshore as a strong land breeze.

Section 1.4 Cloud and precipitation feedbacks

Once moist convection develops in response to topographically-forced ascent, the clouds and precipitation formed act as feedback mechanisms that subsequently alter the flow dynamics. In this section, we discuss a few feedback mechanisms affecting both the mechanical-lifted and thermally-driven regimes.

1.4.1 Cloud shadowing

Immediately after clouds form over a heated terrain, they block incoming solar radiation. Thus, the sensible heat flux coming off from the cloud-covered ground is reduced. As result, the air temperature decreases below the cloud-covered land surface and the thermal forcing weakens. Using numerical simulations, Segal et al. (1986) found that the overall effect of large-scale cloud shading is to reduce the thermally-driven circulation strength. Frame and Markowski (2013) also found that gust fronts enhanced by cloud-shadowing can cut off inflow and weaken a convective storm. However, sometimes a circulation can intensify if the land surface is shadowed in a way such that the diabatic heating differences between a clear area and a cloudy area reinforces the temperature gradient. The resulting temperature gradient can exceed several degrees Celsius, large enough to generate new mesoscale circulations (Purdom and Gurka, 1974).

1.4.2 Cloud latent-heat release

In a hydrostatically balanced atmosphere, the pressure at some level is proportional to the weight per unit area of the atmosphere above this level. Since cumulus convection releases latent heat and lowers the air density within the cloud layer, the weight of the atmospheric column above the mountain decreases. This creates a low pressure anomaly over the mountain summit, which helps to draw in the upslope flow and enhance the moisture convergence (Houze, 1993; Damiani et al., 2008). An example of such phenomenon was studied during the 2006 CuPIDO campaign. Geerts et al. (2008) found that the anabatic convergence over a mountain feature sometimes peaked before the local solar noon when the sensible heat flux is the greatest. They attributed this observation to the cumulus latent-heat release creating a low pressure anomaly over the summit, which might have enhanced the toroidal circulations.

The same process can also strengthen the windward ascent in mechanically-forced orographic flow. In a hydrostatic flow, an unsaturated air parcel cools dry-adiabatically during a mechanically-forced ascent. This causes the air parcel's temperature to become cooler than its environment, thus it becomes negatively buoyant. The negative buoyancy induces a downward acceleration that prevents the flow from ascending up the windward slope. However, if the air parcel saturates during the ascent, latent-heat release increases the air parcel's temperature and weakens the negative buoyancy. As result, the suppressive downward acceleration is reduced and flow is allowed to ascend along the windward slope (Jiang, 2003; Minder et al., 2013). In a thermally-driven regime, latent-heat release by orographic convection also has a significant impact on the flow dynamics over a mountainous island (Nguyen et al., 2010).

1.4.3 Evaporation of precipitation

As mentioned in Section 1.2.3, evaporation of liquid droplets back to vapor phase absorbs latent heat. Evaporation occurs when precipitation falls into an unsaturated air, which generates cold pools. Precipitation cold pools have major impact on the dynamics of a thermally-driven system. Chen and Wang (1995) found that the evaporation of early-morning precipitation over Hawaii's windward slopes led to a slower land surface warming, which delayed the onset of upslope flows. Downslope flows over Taiwan's Central Mountain Range were also enhanced when precipitation from decaying storms rapidly cooled the air temperature over the mountain (Ruppert et al., 2013).

The precipitation produced by a thermally-driven convection also has an impact on the elevated convergence driving the convective storm. For instance, a substantial weakening of the surface convergence due to thunderstorm cold pools was found during the 2006 CuPIDO campaign (Geerts et al., 2008; Demko et al., 2009). Despite signs of cumulus convection was enhancing the upslope flows in the morning, the deep cumulonimbus formed in the afternoon produced cold pools that reversed the anabatic convergence to katabatic divergence.

Section 1.5 Motivation

Despite extensive observational and numerical studies on thermally-driven flow dynamics over differentially heated terrains, there remain large gaps in the understanding of thermally-driven convection. In addition, little is understood about the complex interaction between different topographic forcing mechanisms, which include mechanically and thermally-forced flows.

Kirshbaum and Wang (2014) studied the combination of mechanical and thermal forcing using idealized simulations. One of the methods used to quantify the thermally-forced updraft strength was the heat-engine framework first developed by Souza et al. (2000) and later extended by Tian and Parker (2003). They found that the heat-engine theory outperforms the linear scaling of thermally-driven updraft strength under the "growth-decay" regime, where the background flows are weak and convergence is focused over the crest (Kirshbaum, 2013). However, their simulations used a simplified heating function such that it assumes a sinusoidal evolution in time and an exponentially decreasing magnitude with height. Furthermore, the effects of land surface variation on heating were also neglected. In our study, we consider a more complicated, real case of convection driven by solar heating over a mountain.

Since the heat-engine theory strictly applies to a "dry" atmosphere, interaction between moist convection and associated dynamics were neglected. Therefore, the sensitivity of thermally-driven convection to a number of atmospheric and terrain parameters were not thoroughly investigated. Previous research projects such the 1990 Hawaiian Rainband Project (HaRP, Carbone et al., 1995; Yang et al., 2005) and the Maritime Continent Thunderstorm EXperiment (MCTEX, Carbone et al., 2000; Crook, 2001) have used numerical models to simulate thermally-forced flow over either a flat or mountainous topography. However, the spatial resolutions they used were insufficient to resolve small (or shallow) cumuli (Bryan et al., 2003). Thus, the effects of various atmospheric and terrain parameters on thermally-forced shallow cumulus convection were not adequately addressed.

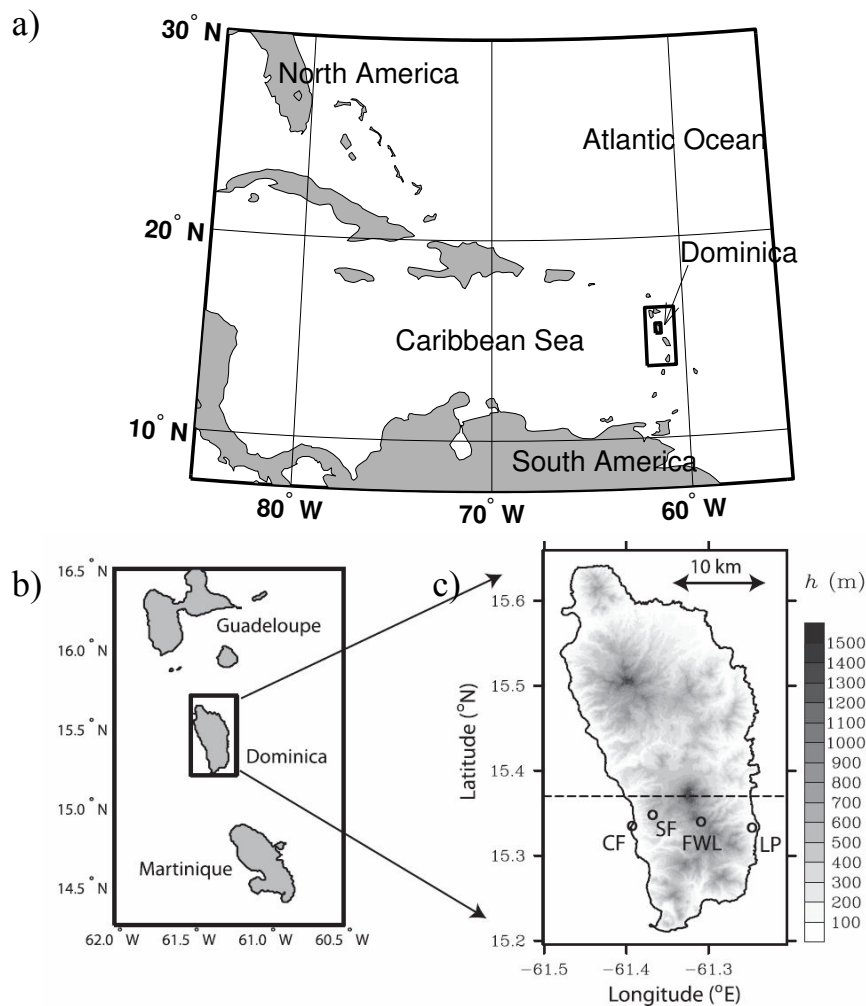


Figure 1.5. a) A map of the Caribbean Sea showing the location of Dominica, b) a zoomed-in map of Guadeloupe, Dominica, and Martinique (the outer boxed area in Fig. 1.5a), and c) a zoomed-in terrain elevation (filled contours) map of Dominica (the boxed area in Fig. 1.5b). CF, SF, FWL, and LP denote the locations of Canfield, Springfield, Freshwater Lake, and La Plaine, respectively. (Figures 1.5 b and 1.5c from Kirshbaum and Smith, 2009)

To address the above questions, we exploit data collected during the 2011 Dominica EXperiment (DOMEX) campaign and use cloud-resolving numerical simulations. Dominica is an island that lies between the French islands of Guadeloupe and Martinique ($15^{\circ}25' \text{ N}$, $61^{\circ}21' \text{ W}$). It is about 17 km wide from east-to-west and 45 km long from north-to-south (Fig. 1.5) and is situated in the Atlantic's easterly-trade wind belt. Strong ($> 8 \text{ m s}^{-1}$) trade-wind flows frequently impinge on the roughly north-south

oriented ridge of the island, producing heavy precipitation over the windward slopes (Smith et al., 2009, 2012). Various numerical simulations have been performed to investigate the dynamics of mechanically-forced convection initiation over Dominica's windward slopes on strong trade wind days (Kirshbaum and Smith, 2009; Kirshbaum and Grant, 2012; Minder et al., 2013). However, thermal-forcing appeared to be the dominant driving-mechanism of island cumulus convection on four weaker trade-wind ($< 5 \text{ m s}^{-1}$) days during DOMEX. Thus, the island also serves as a natural laboratory for studying thermally-driven circulation and associated cumulus convection over a heated terrain.

In this study, observational results from the weak trade-wind cases during the DOMEX campaign are analyzed. These findings are complemented by numerical simulations, which help us to evaluate the ability of a cloud-resolving model to simulate thermally-driven flows over a complex terrain and investigate the effects of various atmospheric and terrain parameters on thermally-forced flow and associated cumulus convection. The relative impacts of different moist convection feedbacks on thermal circulation are also studied using numerical sensitivity tests. Lastly, the heat-engine theory's ability to predict thermally-driven updraft strength over a complex terrain is examined.

Chapter 2. DOMEX Observations

Section 2.1 Datasets

2.1.1 Field campaign data

The 2011 Dominica EXperiment (DOMEX) field campaign phase took place over the island of Dominica from April 4th to May 10th. The field campaign's main goals

were to 1) investigate the mountain-triggered convection and precipitation characteristics, 2) obtain datasets suitable for testing and improving numerical simulations of small-scale topographically-induced convection and precipitation, and 3) improve the climate and weather predictability of the Lesser Antilles (Smith et al., 2012).

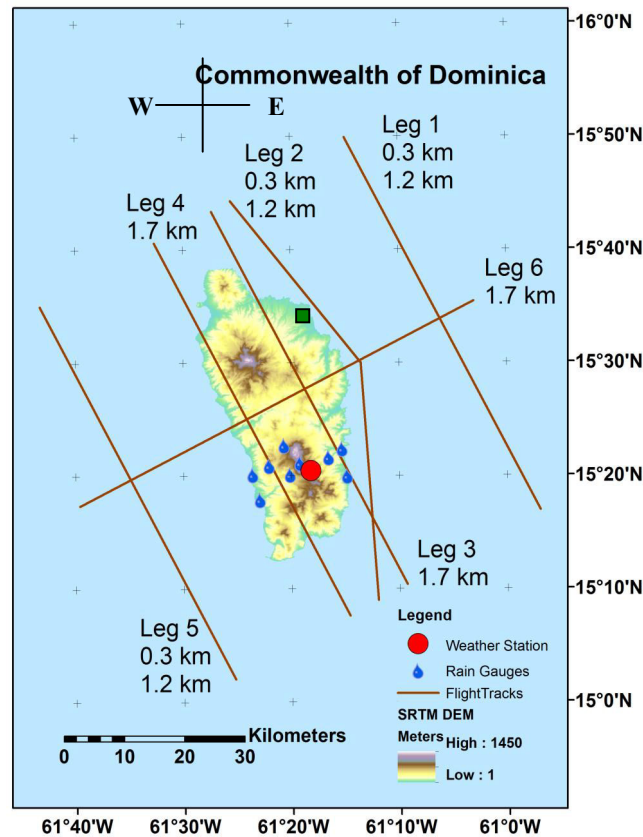


Figure 2.1 A map of the DOMEX field campaign instrument setup and WKA aircraft flight legs (thin brown lines). The filled red circle denotes the location of FWL surface weather station. The blue droplets indicate individual rain gauge locations. The filled green square marks Melville Hall airport's location. Dominica's elevation is shown in filled contours (from Smith et al., 2012)

The data collected during DOMEX consisted of both surface-based observations and aircraft measurements. A satellite linked weather station was deployed on the windward slope of Morne Trois Piton at Fresh Water Lake (FWL, ~ 860 m above sea-level. Fig. 2.1). The weather station provided two-minute updates on the temperature, water vapor mixing ratio, humidity, atmospheric pressure, and shortwave and long-wave

radiation fluxes. A 6-m tall tower was constructed on a nearby vegetation-free bare ground to obtain unobstructed wind measurements. Other surface-based instruments associated with the field campaign included a rain gauge network deployed over the southern portion of the island as shown in Fig. 2.1 (Smith et al., 2012).

The University of Wyoming's King Air (WKA) research aircraft was deployed to observe the atmosphere above Dominica. Several Rosemount sensors were deployed on the aircraft to measure the flight-level temperature and pressure. The humidity data was obtained using a LICOR absorption sensor and an Edgetech chilled mirror dewpointer. The aerosol concentration and size distribution were measured using a Condensation Nuclei (CN) counter and a Passive Cavity Aerosol Spectrometer Probe (PCASP). The cloud number concentration, droplet size distribution, and liquid water content were measured using a Forward Scattering Spectrometer Probe (FSSP) and a Cloud Droplet Probe (CDP). Furthermore, the aircraft was equipped with an inertial reference unit and a gust probe that measure the flight-level winds. The above measurements were sampled in 25 Hz frequency, but they were reprocessed into 1-sec. intervals for the ease of analysis. Other than the in-situ instruments, remote-sensing instruments such as the 95-GHz Wyoming Cloud Radar (WCR) and two-channel elastic Wyoming Cloud LIDAR (WCL) were also deployed on the WKA (Wang et al., 2009) to detect cloud and precipitation droplets. For detailed descriptions of cloud physics instruments deployed on The King Air, please visit the field campaign website: <http://www.domex2011.com/home>). For information on WCR, please visit: <http://www-das.uwyo.edu/wcr>.

At the beginning of each scheduled flight operation, a sounding flight sampled the undisturbed upstream flow approximately 20 km to the east of the island before the flow

interacted with Dominica's terrain. Horizontal flight paths (or legs, Fig. 2.1) were then conducted according to the day's pre-flight weather report. Some of these flight legs were repeated at different heights, for instance, Legs 1, 2, and 5 were each flown at 300 m and 1200 m above the ocean. Leg 1 was designed to sample the turbulent variability in the upstream subcloud and cloud layers. Leg 2 was intended to study the changes in the trade-wind flow as it neared the island's windward coast. Legs 3 and 4 flew directly over and parallel to the north-south oriented Dominica at about 1800 m above sea-level. On days that favored thermally-driven convection, Legs 3 and 4 were conducted at least once each or repeated several times in a racetrack pattern over the island. Otherwise, they were performed once each on days that favored mechanically-forced convection. Other flight legs include Legs 5 and 6. The former was flown to investigate the downstream modifications of the boundary layer by moist convection and gravity-wave breaking over the island's terrain; and the latter was only flown on certain days to capture the variability in cumulus convection and the trade-wind inversion height across the island. Since our goal in this study is to better understand the thermally-driven circulation and associated cumulus convection over a heated terrain, we focus our aircraft observation analysis and model verification using the WKA sounding and Legs 3 and 4 observations.

2.1.2 Operational data

Operational datasets also provided additional information on the weather conditions over and near Dominica during DOMEX. At the surface, two 2.8-GHz French weather radars scanned the area in 5-min. cycles for precipitation occurrence. One of the radars was located approximately 60 km to the north of Dominica on the island of Guadeloupe and another was located about 60 km to the south of Dominica on

Martinique (Fig. 1.5). Melville Hall Airport (MH), located on the northeastern coast of Dominica, provided hourly surface temperature, humidity, and pressure (Fig. 2.1). Finally, the National Oceanic and Atmospheric Association's (NOAA) Geostationary Operational Environmental Satellite (GOES) supplied half-hourly visible satellite images over Dominica at 1-km resolution.

Section 2.2 Overview of DOMEX observations

Based on a multi-year radiosonde climatology of Dominica, Smith et al. (2009) found that strong ($6\text{-}10\text{ m s}^{-1}$) trade-winds between the 925- and 850-hPa layer are climatologically common in Dominica. Therefore, the main objective of DOMEX as well as the first DOMEX studies focused on understanding the mechanically-forced convection over the island. They found that mechanically-forced convection typically develops when the trade-wind speed is $> 8\text{ m s}^{-1}$ at $\sim 300\text{ m}$ above sea-level (Smith et al., 2012). A strong trade-wind case (April 27th or RF13) during DOMEX was examined to study the mechanically-forced flow and windward-side cumulus convection (Smith et al., 2012; Minder et al., 2013). Legs 3 and 4 flight-level winds were convergent during RF13 because the trade-wind flow plunged beneath the flight level as it crossed Dominica's ridges (Fig. 2.2a), leaving Leg 4 with weaker winds than Leg 3 (Smith et al. 2009; Minder et al., 2013). In addition, a nearly constant aerosol concentration of $\sim 30\text{ cm}^{-3}$ was measured along Legs 3 and 4 over both the land and ocean (Fig. 2.2b), which Smith et al. (2012) suggested was due to oceanic air being advected over the island by the strong trade winds.

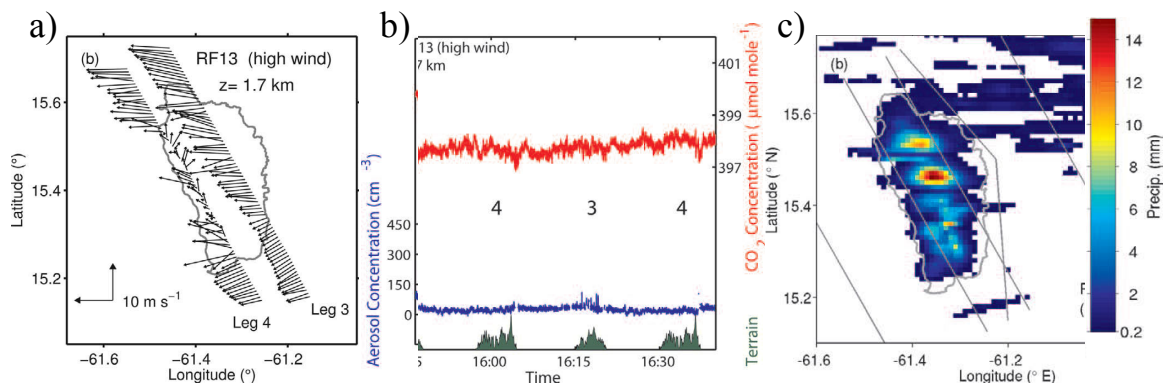


Figure 2.2. DOMEX observations during RF13: a) Legs 3 and 4 flight-level winds, b) aerosol concentration along Legs 3 and 4, and c) radar-derived accumulated rainfall during the 2-hr aircraft observation period (from Smith et al., 2012).

Aerosol particles serve as condensation nuclei for cloud droplets. How large the cloud droplets can grow depends on the amount of water vapor available and concentration of condensation nuclei in the air. For a fixed condensation rate, fewer cloud droplets implies more rapid cloud droplet growth. Since the air over Dominica during RF13 contained few cloud condensation nuclei, the cloud droplets grew rapidly through condensation. The mean cloud droplet diameter observed along Legs 3 and 4 during RF13 was $\sim 25 \mu\text{m}$ (Smith et al., 2012). Cloud droplets larger than this size may further grow to precipitation size by collision-coalescence (Rogers and Yau, 1989). These large cloud droplets probably facilitated the collision-coalescence growth of raindrops, which partly contributed to the heavy rainfall observed during RF13 over Dominica's windward slopes (Fig. 2.2c). In contrast, little precipitation was observed during RF13 over the lee slopes. This is because the flow warmed and dried out as it plunged down the lee slopes of Dominica, suppressing clouds and precipitation.

Section 2.3 Analysis of thermally-driven events

Although mechanically-forced convection is climatologically common over Dominica, the trade-wind speed does occasionally fall below 5 m s^{-1} (Smith et al. 2009). A handful of weak trade-wind days were observed during DOMEX (Smith et al. 2012). However, only April 18th (RF07) was analyzed in Smith et al. (2012). On this day, thermally-driven circulations developed and produced divergent outflows near the boundary-layer top, which were sampled by the WKA along Legs 3 and 4 (Fig. 2.3a). In addition, the aerosol concentration measured along Legs 3 and 4 was around $200\text{-}300 \text{ cm}^{-3}$ above the island as the aerosol-rich island surface air was advected upward by the circulations (Fig. 2.3b). Because the air over Dominica contained more aerosol particles, the mean cloud droplet diameter was only $\sim 15 \mu\text{m}$. The small cloud droplet size hindered the collision-coalescence growth of raindrops, which partly contributed to the lack of island rainfall (Fig. 2.3c). The lack of rainfall may also have been associated with the shallower and drier cloud layer over the island (Smith et al., 2012).

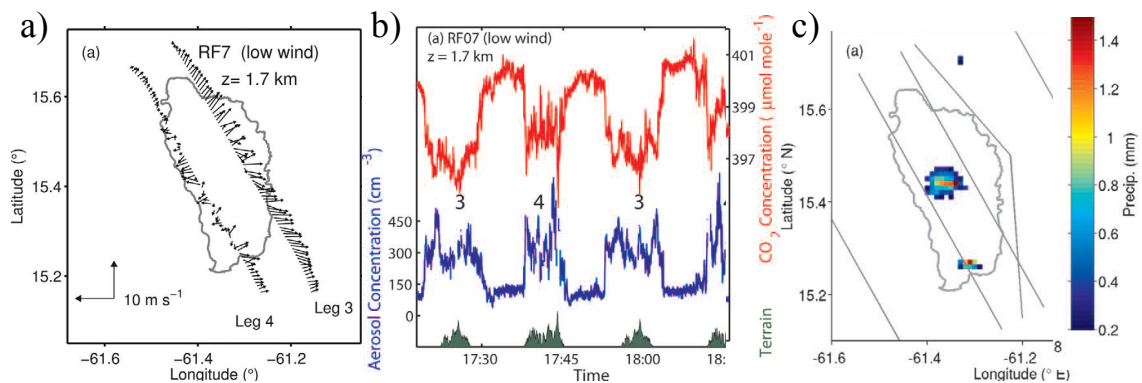


Figure 2.3. Same as Figure 2.2 but for RF07 (from Smith et al. 2012).

Other than Smith et al. (2012)'s brief analysis of RF07, no other DOMEX study investigated the driving mechanisms of thermally-driven convection over Dominica. One of the questions that were not addressed is whether it was the background moist

instability that was controlling the convection strength or was it the amount of solar heating. Thus, in contrast to previous DOMEX studies, we focus our analysis on the weak wind days to gain a better understanding of the controlling parameters of thermally-driven updrafts and associated cumulus convection. Four weak trade-wind ($< 5 \text{ m s}^{-1}$) days were selected for the observational analysis in our study, namely April 15th, 18th, 19th, and 21st.

Table 2.1 summarizes the upstream flow conditions and background moist instability during the four DOMEX weak trade-wind cases. The cross-barrier component of the background winds below the average height of Dominica's tallest summits ($\sim 1000 \text{ m}$) ranged from $1\text{-}4 \text{ m s}^{-1}$. The Brunt-Vaisala frequencies calculated based on the virtual potential temperature lapse rate below this height were $\sim 3\text{-}8 \times 10^{-3} \text{ s}^{-1}$. These parameters combined yield $Fr < 1$ for all four cases, indicating that vertical motion over Dominica was likely dominated by the thermally-driven upslope flows instead of mechanically-forced ascent (Chapter 1).

	April 15th	April 18th	April 19th	April 21st
U (m s^{-1})	4.9	2.7	3.0	3.6
U_{CB} (m s^{-1})	3.6	1.6	3.0	1.6
N ($\times 10^{-3} \text{ s}^{-1}$)	7.8	6.6	5.4	3.2
Fr	0.47	0.25	0.55	0.50
$q_{v,500}$ (g kg^{-1})	16.2	14.8	14.4	14.9
CAPE/CIN (J kg^{-1})	1268/5	119/87	130/81	157/73
LCL/LFC/LNB (m)	666/1029/10891	810/1177/8535	863/1070/7600	900/900/8359

Table 2.1. Upstream flow conditions of the four DOMEX weak trade-wind cases: wind speed (U), cross-barrier wind speed (U_{CB}), Brunt-Vaisala frequency (N), Froude number (Fr, computed using U_{CB}) below the mean height of Dominica's tallest summits ($\sim 1000 \text{ m}$), and the low-level ($< 500 \text{ m}$) water vapor mixing ratio ($q_{v,500}$). The CAPE, CIN, LCL, LFC, and LNB computed using the full soundings.

To extend the soundings above the maximum altitude of WKA soundings ($\sim 4000 \text{ m}$), we appended the 12 UTC (Coordinated Universal Time or UTC = Local Standard

Time or LST + 4) balloon soundings from Guadeloupe (available at University of Wyoming's sounding database: <http://weather.uwyo.edu/upperair/sounding.html>) to the WKA soundings. Since 4000 m is well above the typical daytime mixed layer height over a tropical ocean, the flow above this height should remain uncontaminated by the daytime boundary-layer mixing over a small tropical island such as Guadeloupe. Thus, we assumed that the balloon sounding data above 4000 m adequately represents the large-scale flow conditions over the region, despite the balloon sounding being released ~60 km to the north of the WKA sounding.

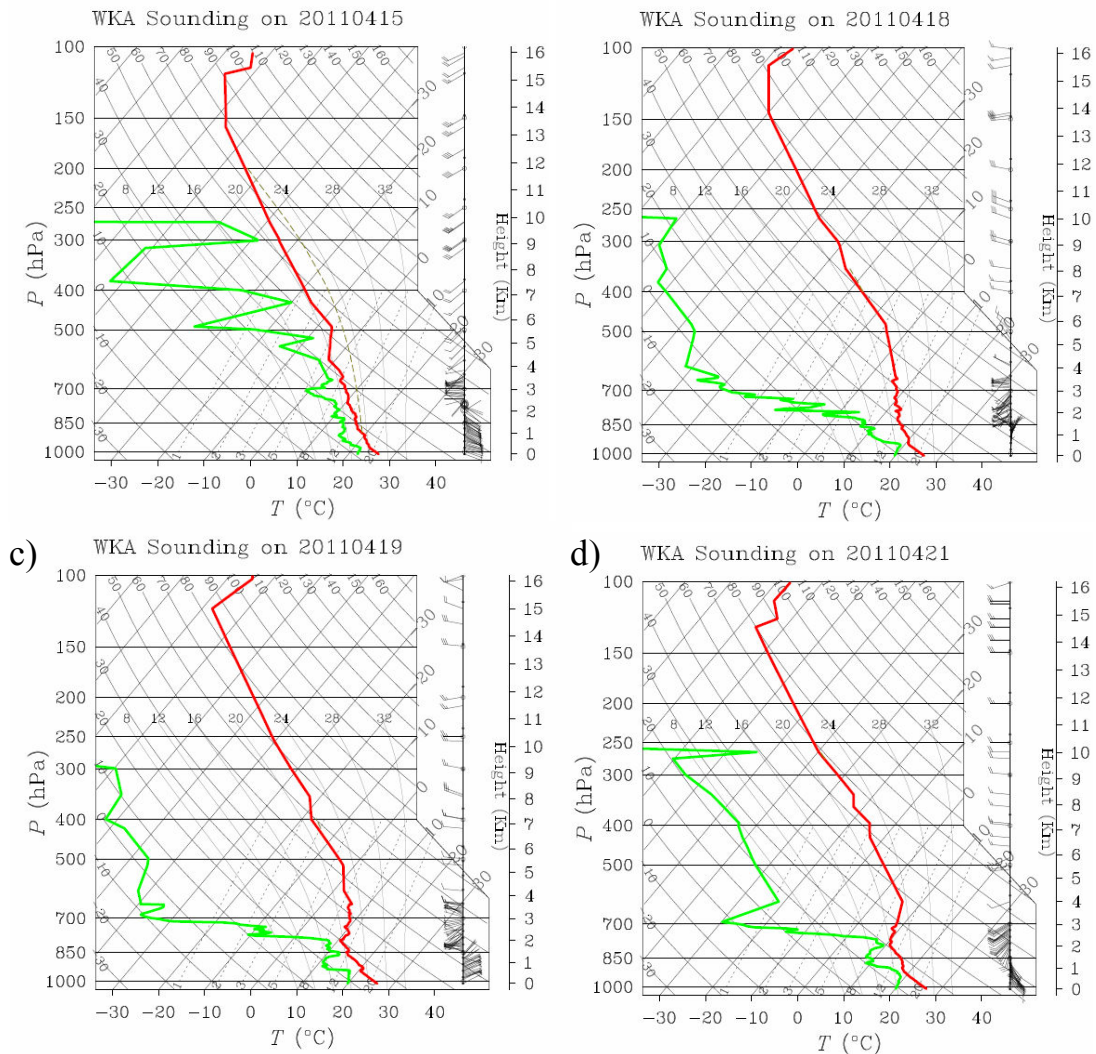
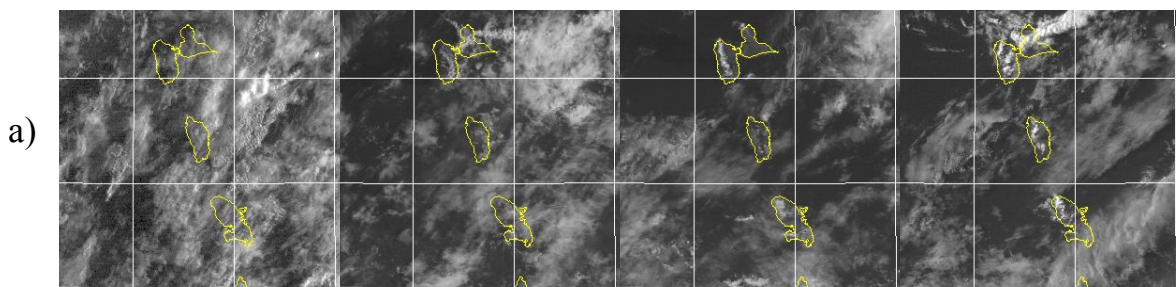


Figure 2.4. Skew-T soundings from the four DOMEX weak trade-wind cases. a) April 15, b) April 18, c) April 19, and d) April 21. The red solid lines indicate the air temperature and light green solid lines show the dewpoint temperature.

The resulting sounding profiles show some major differences between the four weak-wind cases (Fig. 2.4). The water vapor mixing ratio below 500 m ($q_{v,500}$) on the 15th was $\sim 16 \text{ g kg}^{-1}$. Due to this abundant low-level moisture, the LCL on the 15th was the lowest of all four cases (Table 2.1). In addition, the CAPE on this day was $> 1200 \text{ J kg}^{-1}$ because of a deep, nearly saturated, and conditionally unstable layer that extended from the surface up to around 600 hPa. Therefore, deep convection could develop if there is sufficient low-level forcing to lift boundary-layer air parcels up to the LFC. The background winds on this day, however, were the strongest of the four cases (Table 2.1). According to the heat ventilation argument discussed in Chapter 1, the stronger winds might have helped to suppress convection initiation on the 15th.

In contrast, April 18, 19th, and 21st all exhibited considerably less low-level q_v ($\sim 15 \text{ g kg}^{-1}$). The sounding profiles show rapidly falling dewpoints between 750 hPa and 500 hPa (Figs. 2.4b-d), indicating that the air above 750 hPa was also much drier on these days. In addition, unlike the 15th, the atmosphere between 750 hPa and 500 hPa during these three days was statically stable. The CAPE and CIN during these three days only ranged from $\sim 100\text{-}150 \text{ J kg}^{-1}$ (Table 2.1), which suggest that even if the boundary-layer air parcels were lifted up to the LFC, only shallow convection would occur.



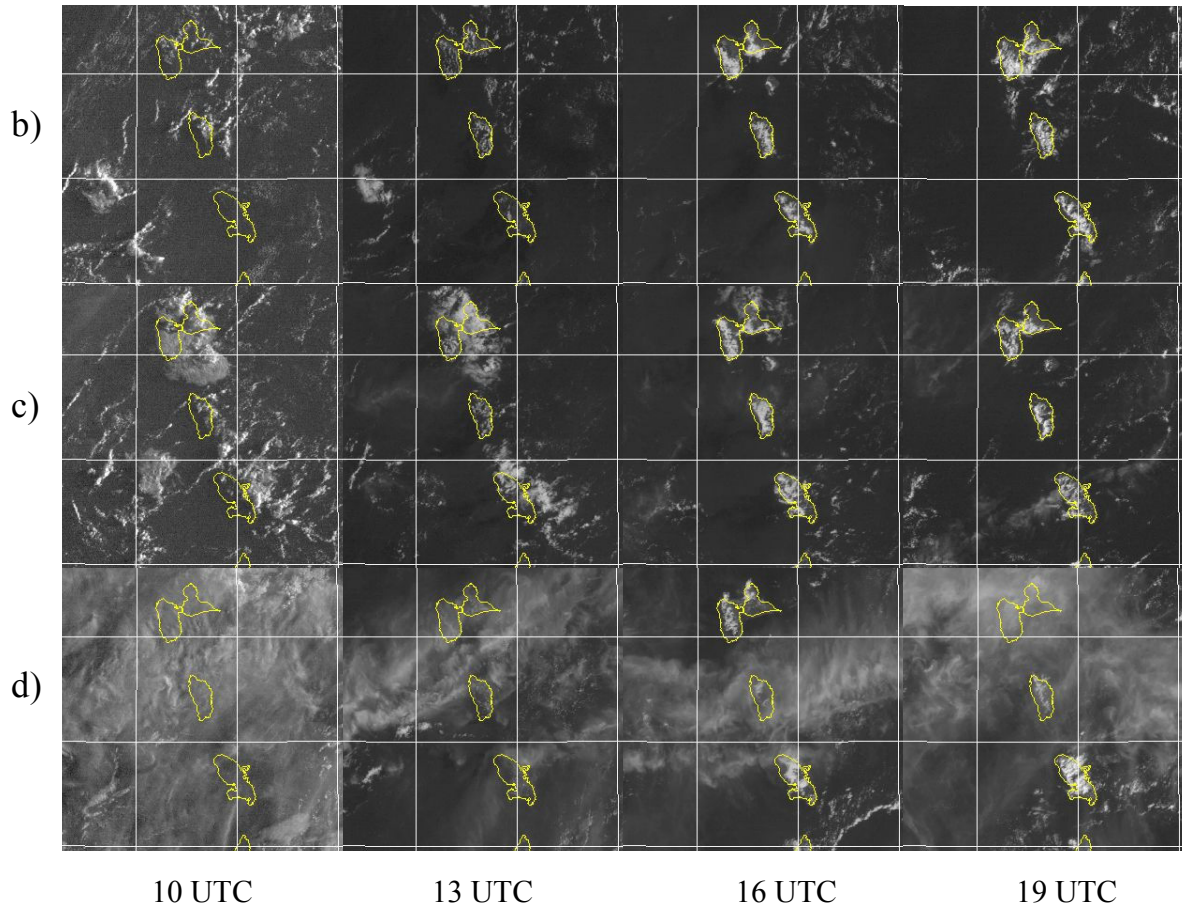


Figure 2.5. Selected satellite images for the four DOMEX weak trade-wind cases at 10, 13, 16, and 19 UTC: a) April 15, b) April 18, (c) April 19, and (d) April 21.

Figure 2.5 shows the selected visible satellite imageries closest in time to 10, 13, 16, and 19 UTC from the four DOMEX cases. April 15th featured intermittent large-scale stratocumulus clouds throughout the day (Fig. 2.5a). The large-scale cloud cover reduced the solar heating, which along with the stronger background winds (Table 2.1), suppressed the thermally-driven ascent and limited cumulus convection over the island (Fig. 2.5a). However, just enough low-level forcing was present to trigger a deep convective storm over the island's northern crest between 16-18 UTC. Figure 2.6 shows the WCR reflectivity (left panels) and Doppler vertical velocities (right panels) for selected over-island legs from the four cases. The reflectivity image taken along April 15th's Leg 3-1 (from 1551-1603 UTC) shows an isolated convective cell over the island

that was at least 5 km deep with little additional clouds (Fig. 2.6a.L) elsewhere. The vertical velocity image shows mainly downward motion within this convective storm, which indicates that the storm was decaying at the time (Fig. 2.6a.R). Otherwise, the flow elsewhere along the leg was relatively tranquil.

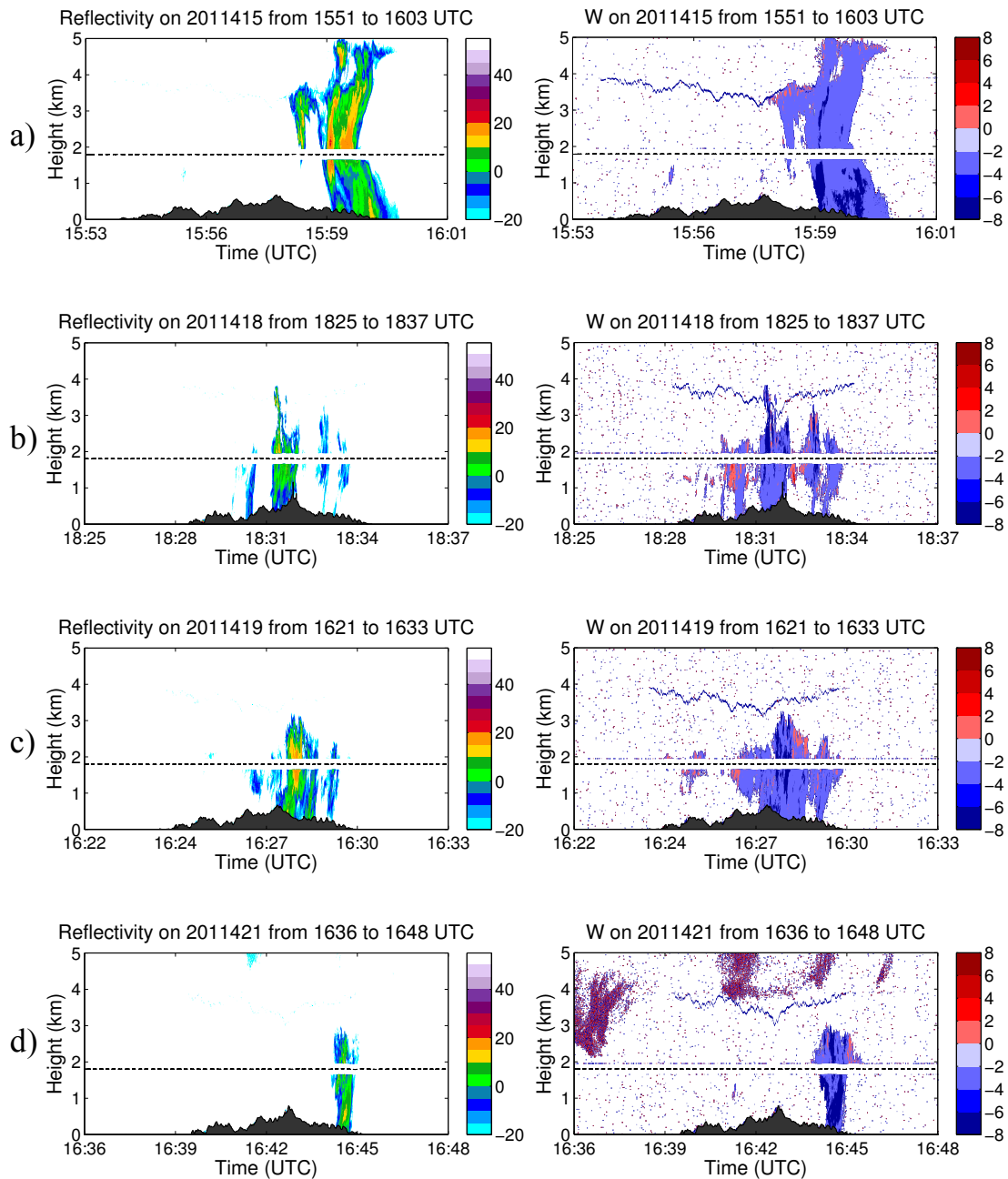


Figure 2.6. Selected WKA: L) WCR reflectivity and R) vertical velocity along the over-island transects during a) April 15, b) April 18, c) April 19, and d) April 21. The Dominica's terrain as seen from the WKA is also shown at the bottom of each plot.

Figure 2.7 shows the Guadeloupe radar-derived accumulated rainfall from 0-21 UTC of the four DOMEX cases based on the radar-specific Z-R relationship

$$R = \left(\frac{Z}{85}\right)^{\frac{1}{1.2}} \quad (2.1)$$

where R is the rainfall rate, Z is the radar reflectivity in μm^{-3} , and a scanning frequency of every 5 minute (Smith et al., 2009). The convective storm on the 15th produced ~20 mm of rainfall near the northern summit (Fig. 2.7a). Some showers also occurred just offshore of Dominica on the 15th, amounting more than 40 mm of rainfall.

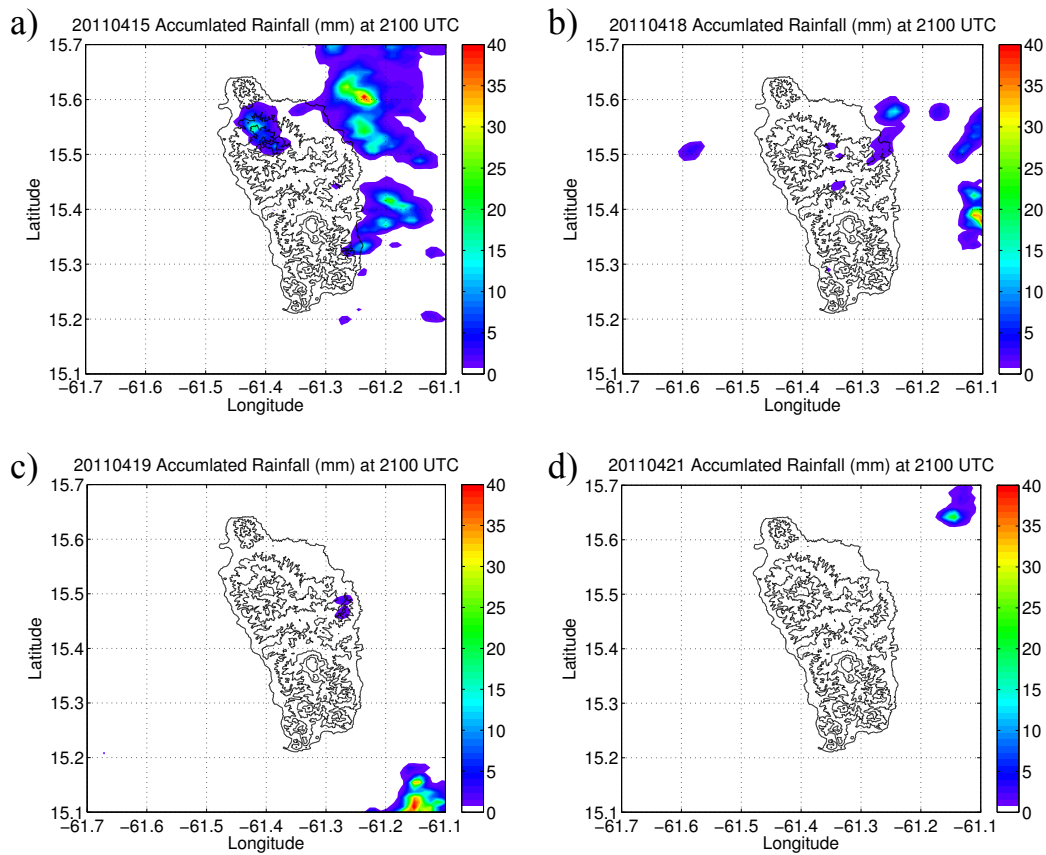


Figure 2.7. Radar-derived accumulated rainfall ending at 21 UTC for a) April 15, b) April 18, c) April 19, and d) April 21.

The weather on the 21st was similar to the 15th in that it also featured an extensive large-scale cloud cover over the region (Fig. 2.5d). This cloud cover mainly consisted of upper-level cirrus clouds associated with a subtropical jet. Like the stratocumulus clouds on the 15th, these cirrus clouds also reduced the solar heating over the island and limited the island thermal forcing. However, in contrast to the 15th, a stable temperature inversion was present between 700-600 hPa with dry air above 750 hPa. As result, only a few cumulus clouds developed (Fig. 2.5d). The WCR reflectivity and vertical velocity images from the 21st show an isolated shallow convection with little turbulence over the island (Figs. 2.6d.L and 2.6d.R). Due to the lack of cumulus convection, the radar-derived rainfall was minimal over the island (Fig. 2.7d).

April 18th and 19th both featured similar weather conditions. Like the 21st, the air from 750 hPa to 500 hPa was dry. However, owing to the limited large-scale cloud cover (Figs. 2.5b-c), abundant solar heating generated strong upslope flows which in turn produced widespread shallow cumulus convection over the island starting at ~14 UTC. The cumuli initially formed parallel to Dominica's north-south oriented ridgeline over the eastern slopes, but they shifted over to the western slopes in the afternoon. This shift was either due to 1) the weak easterly trade winds blowing the cumulus convection westward or 2) the westward propagating sun angle shifting the strongest solar heating and dominant convergence zone over the lee slopes. The WCR reflectivity and vertical velocity images from the 18th and 19th (Figs. 2.6b-c) indicate that the cumuli reached 3-4 km above sea-level and the flow was also much more turbulent than the other two days. Despite the intense shallow convection over the island and precipitation shaft evident on the WCR images, the radar derived rainfall was < 2 mm on both days (Figs. 2.7b-c). This

likely resulted from the shallow and dry cloud layers and small droplets due to large aerosol concentrations, which together limited the amount of precipitation.

To quantify the thermally-driven forcing over Dominica during the weak wind events, we compared the FWL and near-surface measurements from the aircraft sounding. To undertake such a comparison, we need time-varying meteorological data from both locations. At FWL, 2-min. surface observations were averaged into 10-min. intervals for the analysis. However, the ocean sounding was only conducted once. Thus, time-varying data of the surface air temperature and sea-level pressure (SLP) at the ocean sounding site were unavailable. To fill these missing data, we performed the following procedures:

1) For the surface air temperature, we extrapolated the lowest sounding level air temperature dry-adiabatically down to sea-level and assumed that it was in a steady-state (i.e no diurnal cycle). Therefore, the surface air temperature over the ocean was constant throughout a day.

2) For the SLP, we first corrected the pressure at the lowest sounding level down to sea level using the hypsometric equation:

$$SLP = P_1 \exp\left[\frac{g(z_1 - z_0)}{R_d \bar{T}_v}\right] \quad (2.2)$$

where P_1 is the pressure at the lowest sounding level, g is the gravitational acceleration, z_1 is the altitude of the lowest sounding level, z_0 the sea-level (= 0 m), R_d is the dry air constant, and \bar{T}_v is the averaged virtual temperature in the layer between the lowest sounding level and sea-level. To obtain the SLP time-series, we used the 6-min. SLP data from two nearby airports (TFFR or Guadeloupe and TFFF or Martinique) in the region. Here we assumed that the SLP over the ocean is mainly influenced by the global-scale semidiurnal tides and synoptic-scale pressure systems. In a separate study that exploited

the airports' SLP data, Minder et al. (2013) found that land surface heating can induce mesoscale pressure anomalies in these datasets. To prevent these undesired pressure signals from obscuring the "true" pressure variation over the ocean, we first filled the missing data in the airports' SLP time-series using a spline interpolation. The airports' SLP time-series were then low-pass filtered using a fifth-order Butterworth filter with a 4-cycles day⁻¹ cutoff frequency. The filtered airport SLP time-series were then averaged into a single time-series and interpolated to 10-min. intervals. Finally, this time-series was fitted to the single sounding measurement by first finding the difference between the two at the time of WKA sounding and then shifting it up or down accordingly to match the observed ocean sounding SLP (Fig. 2.8).

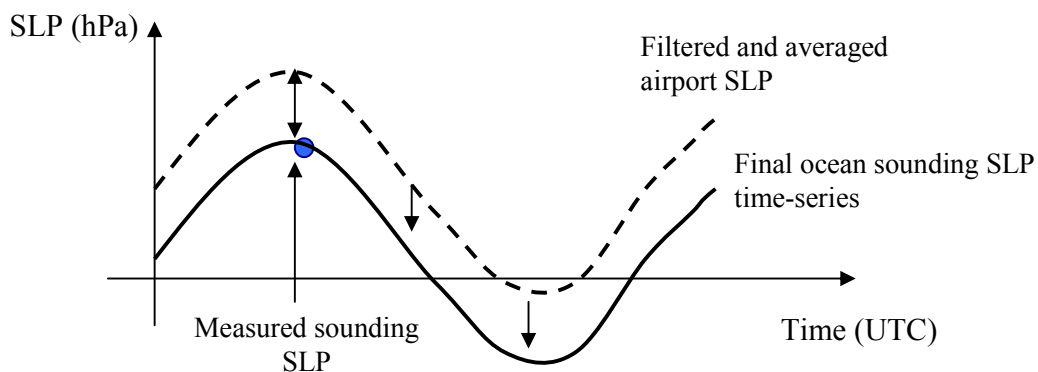


Figure 2.8. An illustration of procedures for constructing the sea-level pressure time-series at the ocean sounding site. The dashed line represents the filtered and averaged SLP data from TFFR and TFFF. The blue dot indicates the single SLP measurement from the WKA upstream sounding. The double-head arrow shows the difference between the filtered and averaged airport SLP and the single WKA SLP measurement at the time of the upstream sounding. The downward arrows indicate the direction of shift made to fit the airport SLP to the single upstream sounding SLP. Finally, the solid line shows that finished SLP time-series at the ocean sounding site.

Note that due to uncertainties in the tidal correction or the use of instruments with different calibrations, there could be a bias in these measurements. This bias is at least partially removed by comparing the peak-to-trough difference in the air temperature and SLP difference between FWL and the ocean sounding site (referred as ΔT_{SFC} range and ΔSLP range henceforth, respectively), not the absolute maximum or minimum. Also,

because the island-scale circulations take a couple of hours to spin up, we focus our attention to the temperature evolution over the early part of the day (prior to 15 UTC) before the aircraft traversed the island.

Figure 2.9 shows the FWL solar radiation flux (F_s), surface air temperature, relative humidity, water vapor mixing ratio, non-adiabatic temperature difference between FWL and the ocean sounding site, and SLP difference between FWL and the ocean sounding site. According to Figure 2.9a, both the 15th and 21st had relatively low F_s prior to 15 UTC, which confirms that large-scale clouds partially blocked the solar radiation over Dominica in the morning. The total solar energy received per unit area prior to 15 UTC was only $5-6 \times 10^4$ kJ m⁻² on the 15th and 21st compared to $7-8 \times 10^4$ kJ m⁻² on the 18th and 19th (Table 2.2). Due to the reduced solar heating, ΔT_{SFC} range was only $\sim 5^\circ\text{C}$ on the 15th and 21st compared to $> 7^\circ\text{C}$ on the 18th and 19th (Fig. 2.9b and Table 2.2). In addition, the ΔSLP range on the 15th and 21st was also smaller than that the 18th and 19th (~ -2 hPa vs. ~ -3 hPa, Fig. 2.9f). Therefore, the surface data suggests that both the 15th and 21st experienced weaker heating prior to the WKA flights than the 18th and 19th, which led to weaker thermally-driven updrafts and limited cumulus convection over the island.

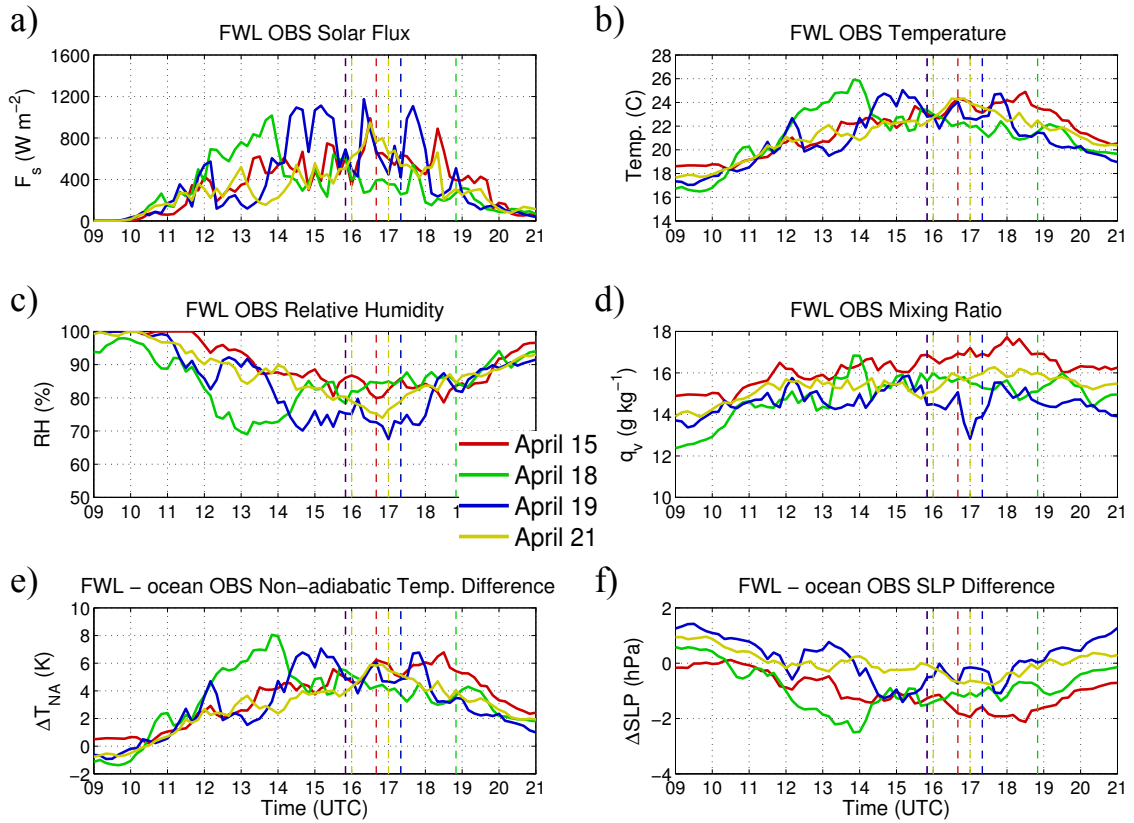


Figure 2.9. FWL observations: a) solar radiation flux, b) surface air temperature, c) relative humidity, d) water vapor mixing ratio, e) non-adiabatic temperature difference between FWL and the ocean sounding site, and f) sea-level pressure difference between FWL and ocean sounding site during the four DOMEX weak trade-wind cases. The colored dashed lines denote the starting and ending times of the WKA over-land legs during each of the four cases.

	Time-Int. F_s ($\times 10^4 \text{ kJ m}^{-2}$)	ΔT_{SFC} Range (K)	ΔSLP Range (hPa)
April 15	5.86	4.7	-2.24
April 18	8.60	9.5	-3.32
April 19	7.17	7.7	-3.15
April 21	4.99	4.9	-1.96

Table 2.2. A summary of FWL surface observations for the four DOMEX weak trade-wind cases: the time-integrated solar flux, the maximum diurnal range of the surface air temperature difference between FWL and the ocean sounding site, and the maximum diurnal range of the SLP difference between FWL and the ocean sounding site evaluated before 15 UTC.

In contrast to the 15th and 21st, the 18th received abundant solar radiation in the morning due to the lack of large-scale cloud cover (Fig. 2.9a). By the time the air temperature at FWL had reached its maximum at ~ 14 UTC, it was at least 9°C warmer

than the morning low (see ΔT_{SFC} range, Table 2.2). In addition, the ΔSLP had dropped by more than 3 hPa from its peak value before sunrise (see ΔSLP range, Table 2.2). Both ΔT_{SFC} and ΔSLP range on the 18th were the largest out of the four cases, reflecting that the 18th experienced the greatest solar heating and heating-induced pressure fall over the mountain before 15 UTC (Figs. 2.9e-f). Note that after 15 UTC, cloud shadowing associated with the cumulus convection blocked the incoming solar radiation. As result, the surface air temperature fell immediately and the island thermal forcing diminished. ΔSLP rebounded in response to the decrease in the island thermal forcing, indicating that the thermal circulations have weakened as well (Fig. 2.9f).

The time-integrated solar flux up to 15 UTC on the 19th was also relatively large (Table 2.2), indicating that Dominica also received abundant solar radiation on this day due to the limited large-scale cloud cover (Fig. 2.5c). However, the time-integrated solar flux was not as large as on the 18th because some early-morning cumuli propagating across the island briefly blocked the solar radiation above Dominica (Fig. 2.5c). As result, both ΔT_{SFC} and ΔSLP range were smaller than those on the 18th (Table 2.2).

One way to quantify the thermal circulation strength is to investigate the inflow strength into the thermal circulation along Legs 2 and 5. However, because Leg 5 was not conducted during the 18th and 19th, we were unable to estimate the strength of low-level inflow into the thermal circulation for all four cases. Therefore, we estimated the strength of this circulation theoretically using heat-engine theory (Souza et al., 2000; Tian and Parker, 2003). The heat-engine theory predicts the circulation speed based on the non-adiabatic temperature and mixing ratio difference between two locations. The non-

adiabatic temperature difference between FWL and the ocean sounding corrects for the height differences between two locations and is given by

$$\Delta T_{NA} = (T_{FWL} + \frac{g}{c_p} h_{FWL}) - (T_{sounding} + \frac{g}{c_p} h_{sounding}) \quad (2.3)$$

where c_p is the dry air specific heat, T_{FWL} is the temperature at FLW, h_{FWL} is the FWL's elevation, $T_{sounding}$ is the temperature at the lowest sounding level, and $h_{sounding}$ is lowest sounding altitude. The maximum ΔT_{NA} before 15 UTC on the 18th and 19th was larger than that on the 15th and 21st, reaching 7-8 K (Table 2.3). The 15th and 21st both had a lower maximum ΔT_{NA} of 4-5 K because of the reduced solar heating in the early-morning.

	Avg. T_{SFC} (K)	Avg. Δr (g kg ⁻¹)	Max. ΔT_{NA} (K)	$W_{T,max}$ (m s ⁻¹)
April 15	296.2	-1.0	4.6	1.42
April 18	295.9	-1.0	8.1	2.46
April 19	295.9	-0.3	6.8	1.93
April 21	296.1	-0.4	4.0	1.59

Table 2.3. The averaged air temperature between FWL and the ocean sounding site, the averaged water vapor mixing ratio difference between FWL and the ocean sounding site, the maximum non-adiabatic temperature difference between FWL and the ocean sounding site, and the maximum predicted thermal circulation strength during the four DOMEX cases based on the heat-engine theory before 15 UTC.

The thermal-circulation strength (W_T) based on the heat-engine theory is given by

$$|W_T| = \left[\frac{\eta}{\mu} (c_p \Delta T_{NA} + L_v \Delta q_v) \right]^{1/2}; \quad \eta \approx \left(\frac{gz_i}{c_p \bar{T}} \right); \quad \mu \sim 8 \left(1 + \frac{\ell_h}{z_i} \right) \quad (2.4)$$

where η is the thermal efficiency, μ is the frictional dissipation coefficient, z_i is the average mixed layer height (~ 1000 m), L_v is the specific heat of vaporization, Δq_v is the water vapor mixing ratio difference between two locations, \bar{T} is the averaged air temperature of two locations, and ℓ_h is the slope length (~ 8 km). Because the heat-engine theory assumes that the thermal circulation is confined within the mixed layer and

that the circulation speed is constant anywhere along the closed circulation, W_T can also be treated as the strength of boundary-layer updraft above a heated terrain.

The Δq_v between FWL and the ocean sounding site were generally $< 1.0 \text{ g kg}^{-1}$ on these days (Table 2.3). After substituting ΔT_{NA} from each case into Eq. 6, we found that the 18th had the largest maximum W_T ($W_{T,max}$) of $\sim 2.5 \text{ m s}^{-1}$. April 19th came next with a $W_{T,max}$ of $\sim 1.9 \text{ m s}^{-1}$. $W_{T,max}$ on April 15th and 21st was both $\sim 1.5 \text{ m s}^{-1}$. However, several assumptions went into this calculation. For example, z_i was assumed be constant at all times. Therefore, this method is unlikely to quantify the thermal circulation strength with high accuracy, but it still helps us to draw a comparison of thermal circulation strength between the four cases. In Chapter 3, we use more sophisticated calculations from numerical sensitivity tests to validate the heat-engine theory's ability to predict the simulated thermal circulation strength.

According to the heat-engine theory, the thermal circulations on the 18th and 19th were stronger than those on the 15th and 21st due to the abundant solar heating in the morning. Therefore, stronger low-level forcing and solar heating-induced air destabilization were present over the island to trigger vigorous cumulus convection on these days. In contrast, the cumulus convection was predicted to be the least vigorous on the 15th and 21st because of the reduced solar heating in the morning, which led to weaker thermally-driven updrafts and less diurnal destabilization over the island.

To investigate difference in the island convection between the four cases, we analyzed the in-situ observations collected along WKA Legs 3 and 4 during the four cases. Three over-island legs were conducted on the 15th (two Leg 3s and one Leg 4), four over-island legs for the 21st (two legs each), and the 18th and 19th both had six

over-island legs (three legs each). Because the release of moist instability by convective clouds produces stronger vertical motions, more cumuli tend to generate more turbulence. The cloud fraction along Legs 3 and 4, where we defined a measurement with liquid water mixing ratio (q_l) $> 0.1 \text{ g kg}^{-1}$ as a cloud, shows that the days with cloudier mornings (the 15th and 21st) each had a cloud fraction of $< 5\%$ (Table 2.4). In contrast, the days with sunnier mornings (the 18th and 19th) each had a cloud fraction of 20-30%. Thus, the averaged vertical velocity variance (σ_w^2) of all legs on the 18th and 19th was much higher than that on the 15th and 21st.

	Time (UTC)	$\sigma_w^2 \text{ (m}^2 \text{ s}^{-2}\text{)}$	$W_{\text{core}} \text{ (m s}^{-1}\text{)}$	$B_{\text{core}} \text{ (cm s}^{-2}\text{)}$	$M_{\text{v,nor}} \text{ (kg m}^{-2} \text{ s}^{-1}\text{)}$	σ_{cld}
April 15	1550-1640	0.09	NaN	NaN	0.006	0.02
April 18	1720-1850	1.28	2.04	0.61	0.191	0.17
April 19	1550-1720	1.47	2.01	0.55	0.286	0.27
April 21	1600-1700	0.18	1.65	0.27	0.006	0.01

Table 2.4. WKA Legs 3 and 4 measurements from the four DOMEX weak trade-wind cases. Flight period, averaged vertical velocity variance (σ_w^2), averaged cloud-core vertical velocity (W_{core}), averaged cloud-core buoyancy (B_{core}), averaged and distance-normalized vertical cloud mass flux ($M_{\text{v,nor}}$), and island cloud fraction (σ_{cld}).

Analysis of the cumulus properties shows that both the 18th and 19th had an averaged cloud-core vertical velocity (W_{core}), where we defined a cloud point that is positively buoyant and rising as a cloud-core, of $\sim 2 \text{ m s}^{-1}$. This is greater than the averaged W_{core} of $\sim 1.5 \text{ m s}^{-1}$ measured on the 21st. On the 15th, no active cloud core was intercepted along the flight legs. Furthermore, the cloud-core buoyancy (B_{core}) on the 18th and 19th was $0.50\text{-}0.60 \text{ cm s}^{-2}$, but it was about half of that on the 21st. Thus, the flight-level clouds on the 18th and 19th were more vigorous than the flight-level clouds on the 15th and 21st.

Last but not least, the averaged distance-normalized vertical cloud mass flux

$$M_{v,nor} = \frac{\rho_{cld} w_{cld} \int ds_{cld}}{\int ds_{leg}} \quad (2.5)$$

where ρ_{cld} is the cloudy air density, w_{cld} is the cloud vertical velocity, ds_{cld} is the integrated cloud width, and $\int ds_{leg}$ is the total distance traveled along a leg, of all legs was also larger on the 18th and 19th than that on the 15th and 21st. The higher $M_{v,nor}$ is consistent with the higher σ_{cld} , and W_{core} .

Section 2.4 Conclusions from the observations

Several conclusions may be drawn from the DOMEX observations. April 18th and 19th both received abundant solar heating in the morning, which led to stronger thermally-driven updrafts. Thermally-driven updrafts provided the low-level forcing that triggered widespread shallow cumulus convection over Dominica. Despite having a more unstable and moister atmosphere, less cumulus clouds formed over the island on April 15th because of the reduced solar heating and stronger background winds. Similar to the 18th and 19th, the 21st featured a dry, statically stable mid-troposphere. However, the cumulus convection was suppressed on this day because of the reduced solar heating, at least before the WKA passed over the island. Therefore, the strength of island moist convection appears to depend more on the amount of solar heating and associated thermal circulation strength rather than the background moist instability.

Given that the thermally-driven convection was weak, the 15th and 21st are excluded from the future modeling analysis. Although vigorous cumulus convection developed on both the 18th and 19th, the thermal forcing on the 18th was the strongest due to the lack of early-morning clouds. Thus, we consider this day as the "golden" case

of thermally-driven convection over a heated island and study it extensively in the next chapter using cloud-resolving simulations.

Chapter 3. Numerical Simulations

Section 3.1 Model Description

The Weather Research and Forecasting (WRF) model was used in an idealized configuration to simulate the thermally-driven convection over Dominica. WRF is a fully-compressible, non-hydrostatic Eulerian model that solves the moist atmospheric equations on an Arakawa-C staggered grid (Skamarock et al., 2008). The grid is Cartesian in the horizontal and consists of unevenly spaced, terrain-following pressure levels in the vertical. The equations were time-integrated using the 3rd-order Runge-Kutta (RK-3) scheme. Horizontal and vertical advection were solved using the 5th-order and 3rd-order advection schemes, respectively. The lateral boundary conditions are periodic in both the x- and y-dimensions. The model top is rigid, but a 4-km thick Rayleigh damping layer was implemented at the top of the domain to suppress wave reflection.

The horizontal dimensions are 180-by-180 km, with Dominica's topography centered in the domain. The simulations were performed using horizontal grid spacings of 1 km, 500 m, 250 m, and 125 m. 81 vertical levels were used to resolve the turbulence and microphysical processes at least through the cloud layer. The model top is at 12 km, which gives a vertical grid spacing of approximately 90 m at the bottom and ~300 m at the top. The latitude and longitude of the domain, which control the radiation balance and Coriolis force, were set to the approximate coordinates of Dominica (~15°N, ~61°W).

Since the Coriolis parameter, $f = 2\Omega_e \sin \varphi$ where Ω_e is the Earth's angular speed of rotation ($=7.292 \times 10^{-5} \text{ rad. s}^{-1}$) and φ is the latitude ($=15^\circ\text{N}$), does not vary significantly over the small dimension of the domain, we treated it as a constant.

Since April 18th featured clear evidences of thermally-driven convection over Dominica, we used the combined upstream WKA and Guadeloupe balloon sounding from this day to initialize our simulations. Because the ocean has a minimal diurnal cycle, we assumed that the upstream sounding is representative of the atmospheric conditions above the ocean over the whole day. We initialized the simulations at 09 UTC (05 LST) and ran them for 12 hours to capture half of the diurnal cycle. The flow typically requires 1-2 hours to adjust to the terrain, which occurs early in the day before diurnal heating becomes significant. The simulation outputs were produced at a frequency of 10 minutes.

The MM5 Dudhia shortwave radiation scheme was used to calculate the incoming solar flux based on the domain's latitude, longitude, and the simulation date. This scheme also accounts for the shortwave radiation scattering and absorption by clouds and water vapor. For long wave radiation, we used the Rapid Radiative Transfer Model (RRTM).

A simple 5-layer thermal diffusion surface layer model was used. This model determines the surface heat budget based on the land-use category. We chose evergreen broadleaf forest, a common land surface type in tropical climates, as the land surface type over Dominica. The sea-level land skin temperature over Dominica was initialized at 292 K (19°C), which was around the average sea-level minimum air temperature for the month of April in Dominica (Dominica Meteorological Service). Since the air temperature decreases with altitude, we incorporated a 5 K km^{-1} land skin temperature lapse rate to initialize reasonable skin temperatures at higher elevations. For the

surrounding ocean, we chose water as the surface type. The sea surface temperature was initialized at 300 K, which is the average for April just off Dominica's coast (World Sea Temperature: www.seatemperature.org).

For the surface layer physics, the PSU/NCAR Mesoscale Model 5 (MM5) Monin-Obukhov similarity theory was used. No planetary boundary layer (PBL) scheme was used except at the 1-km grid spacing where we used the Mellor-Yamada-Janjic PBL scheme. Subgrid turbulence was parameterized using a 2-D Smagorinsky-type closure at 1-km grid spacing (where the vertical mixing is carried out by the PBL scheme) and using a 3-D TKE-based closure at smaller grid spacings (where no PBL scheme was used). Finally, microphysical processes were parameterized using the new Thompson microphysics, which solves six hydrometeor categories and is double-moment in rain and ice and single-moment for the other categories. Since the observed aerosol concentration over Dominica ranged from 200-300 cm^{-3} on the 18th, we set the cloud droplet (or condensation nuclei) concentration prescribed in the Thompson microphysics scheme to 200 cm^{-3} . Since moist convection can be represented explicitly at grid spacings of 1 km or less, no cumulus parameterization was used.

To isolate the impacts of island forcing, we seek to maintain the background flow at a steady-state throughout the simulation. However, if we simply ran the full model-physics described above without any modification to the WRF model, the boundary-layer humidity would continuously increase due to surface latent-heat fluxes and tropospheric temperature would decrease due to clear-air radiative cooling. A steady-state can only be achieved when the moistening from the ocean surface and radiative fluxes are balanced by large-scale advection. However, because large-scale forcing is neglected in our

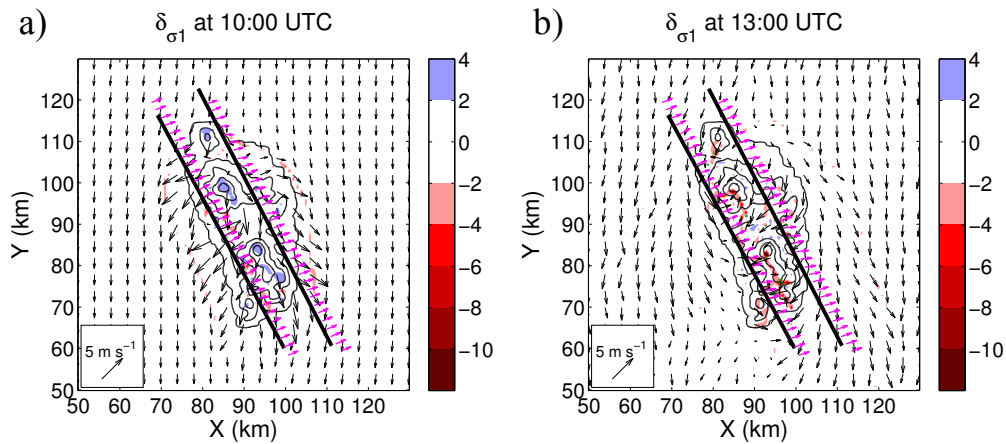
simulations, we preserve steady state by adding in tendencies to precisely cancel out moisture and temperature tendencies associated with ocean latent-heat flux and clear-air radiative cooling. Those tendencies were obtained from a 24-hr. 2-D (in x and z) simulation of purely oceanic flow. For the April 18th case, we diagnosed a diurnal-mean ocean latent-heat flux of 80 W m^{-2} and cooling of 1 K from the 2-D simulation. Thus, we added negative tendencies of that same amount to the subcloud (0-600 m) moisture and tropospheric temperatures, which is adequate to maintain a quasi-steady background flow throughout the simulation.

Section 3.2 Model Verification

The control simulations were performed at four different grid spacings (1-km, 500-m, 250-m, and 125-m) using the model setup described above. Before comparing the numerical simulations, we first describe a numerical issue that affected the 125-m grid spacing simulation, the last of control simulations to be performed. In that simulation, high amplitude sound waves produced spurious wave dynamics over the mountain. To alleviate this problem, we increased the time off-centering parameter in WRF ("epssm") from 0.1 to 0.2, which effectively removed the sound waves. While this change did not strongly impact the island-scale flow dynamics, we still re-conducted the four control simulations using $\text{epssm} = 0.2$ for consistency. However, because we had already carried out the sensitivity experiments described in Sections 3.3-3.7 prior to discovering that problem, so all of those including the corresponding control simulation use $\text{epssm} = 0.1$.

3.2.1 General description

Figure 3.1 shows the temporal evolution of the first model-level winds, first model-level flow divergence, and vertically-integrated cloud liquid water mixing ratio (cloud liquid water path) from the 250-m grid spacing control simulation (CTL-250E2). As indicated in Fig. 3.1a, land breezes can be seen a few kilometers off both the Dominica's east and west coasts by ~10 UTC (6 LST). After sufficient solar heating, the flow over the island begins to reverse from downslope to upslope by ~13 UTC (Fig. 3.1b). In addition, horizontal winds along Legs 3 and 4 extrapolated from the nearest model grid points at the WKA flight level (~1800 m) transition from strong southwesterly along both legs before 13 UTC, to weak southwesterly along Leg 4 and strong southwesterly along Leg 3 by 16 UTC (Figs. 3.1b-c), which signifies the development of elevated outflows and the growth of island thermal circulations.



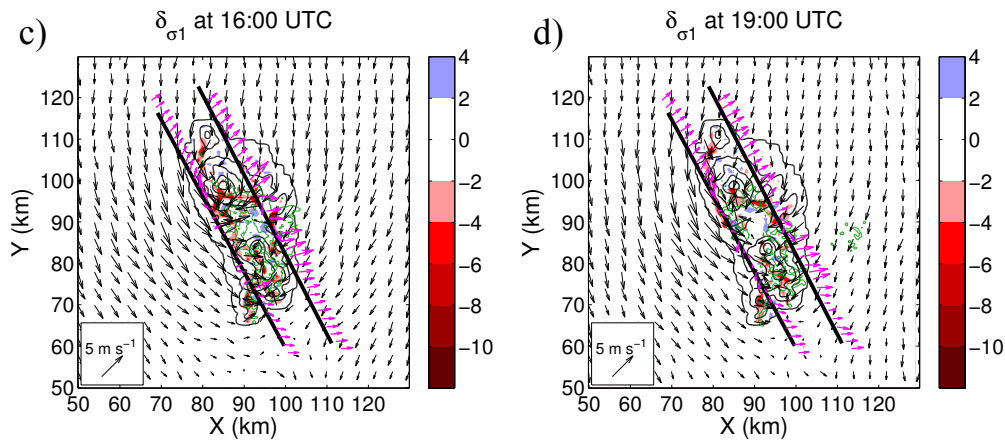


Figure 3.1. First model-level horizontal winds, first model-level flow divergence (filled color contours, scale: $\times 10^{-3} \text{ s}^{-1}$), and vertically-integrated cloud water mixing ratio (cloud liquid water path, green contours $> 0.1 \text{ g m}^{-2}$) from the 250-m grid spacing control simulation at a) 10, b) 13, c) 16, and d) 19 UTC. The terrain elevation is plotted in 250-m intervals except for the outer-most contour, which denotes the 1-m elevation. Flight-level winds (pink arrows) along Legs 3 and 4 (straight black lines) are also shown.

As seen from Fig. 3.1c, the simulated upslope flow convergence has generated enough lifting by 16 UTC to trigger widespread cumulus convection over the island. Both the evaporation of precipitation and cloud shadowing create cold pools (or divergent outflows), which disrupt the organization of the surface convergence. The updrafts generated along the outflow boundaries initially enhance the cumulus convection, but the precipitation cold pools eventually weaken the surface thermal forcing and cause the cumuli to dissipate. This temporarily allows the solar heating to re-strengthen the near-surface convergence and triggers additional convection. The cycle repeats for the remainder of the simulation (Figs. 3.1c-d). Toward the end of the simulation, the convection weakens systematically as the solar heating wanes (not shown).

Figure 3.2 shows the first model-level winds, flow divergence, and cloud liquid water path from the four control simulations at 18 UTC. Thermally-driven convection develops in all four control simulations. However, location of the strongest near-surface flow convergence differs between each simulation such that it is shifted toward the west

coast of Dominica in the 1-km grid spacing run but is located near the island's center in the other smaller grid spacing runs. Furthermore, the 0.01 g kg^{-1} isosurfaces of cloud water mixing ratio (Fig. 3.3) shows that the cumuli in the 1-km grid spacing simulation are much larger than the ones in the smaller grid spacing simulations. To determine which simulation most accurately represents the thermally-driven flow and associated convection over Dominica, we compare the simulated surface and WKA flight track conditions to the observations in Sections 3.2.2 and 3.2.3.

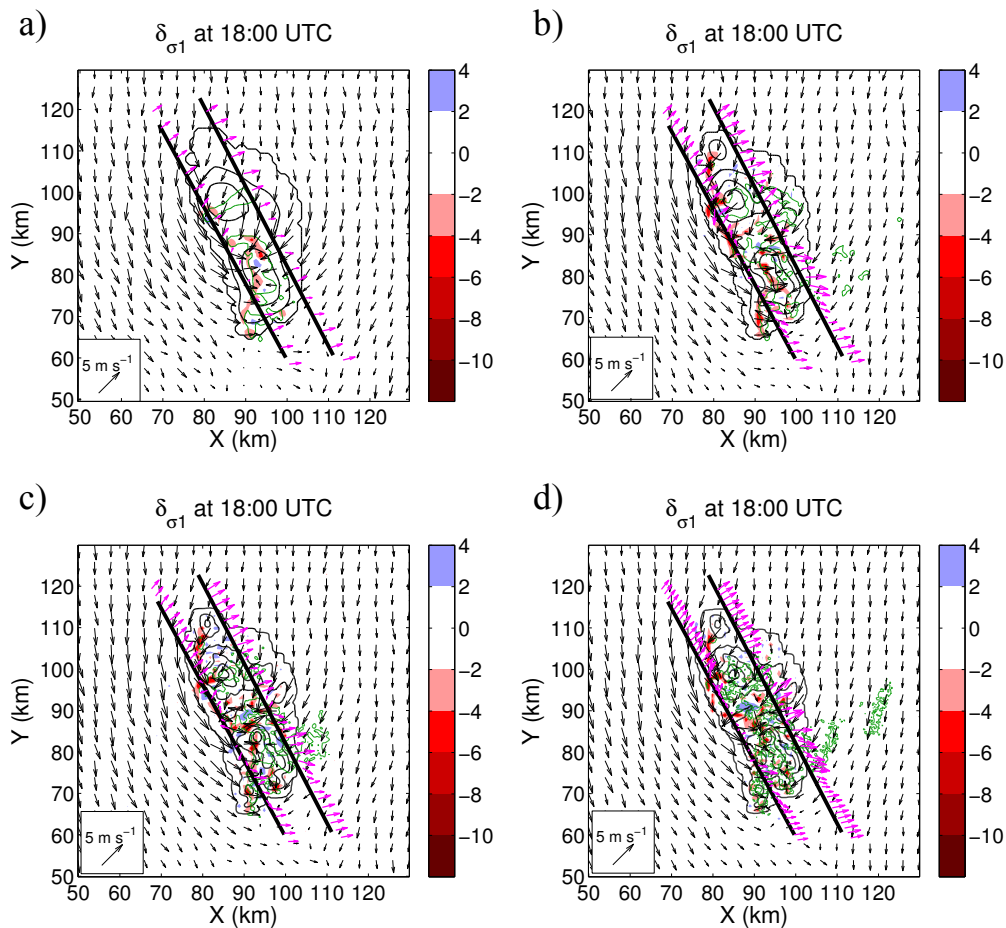


Figure 3.2. Same as in Figure 3.1. but for the four control simulations at different grid spacings: a) 1-km, b) 500-m, c) 250-m, and d) 125-m at 18 UTC.

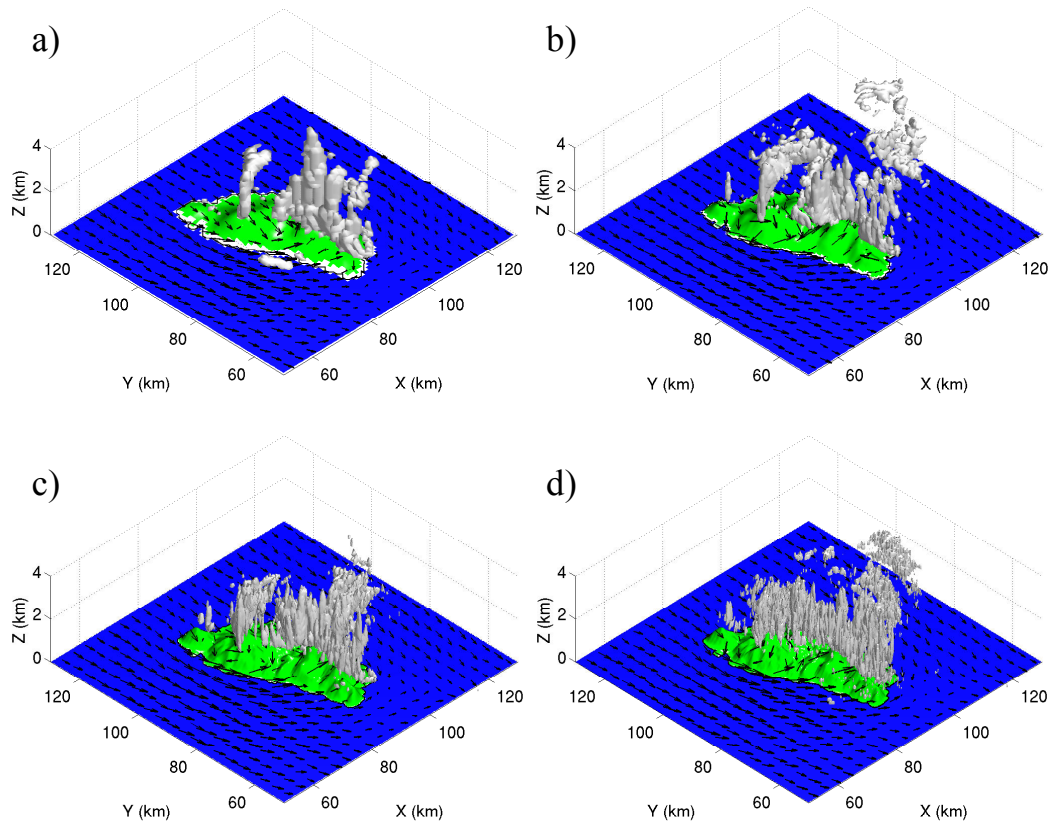


Figure 3.3. Simulated 2-m horizontal winds and 0.01 g kg^{-1} isosurfaces of cloud water mixing ratio from the four control simulations at: a) 1-km, b) 500-m, c) 250-m, and d) 125-m grid spacings.

3.2.2 Surface verification

We begin with a verification of our four control simulations at different grid spacings by comparing the Freshwater Lake (FWL) observations against those simulated at the nearest model grid point in each simulation (Fig. 3.4). In the 1-km grid spacing run (CTL-1000E2), the initial air temperature is $\sim 3^\circ\text{C}$ too high (Fig. 3.4b) because of the poor terrain resolution and lower elevation of FWL in the simulation. Even though the solar flux appears well simulated in this simulation (Fig. 3.4a), the maximum air temperature (Fig. 3.4b) in the CTL-1000E2 simulation is $\sim 4^\circ\text{C}$ too low because sensible heat flux tends to smaller over shorter mountains (e.g Barthlott and Kirshbaum, 2013). As result, the total diurnal air temperature range is only $\sim 4^\circ\text{C}$ (Fig. 3.4b). Because the

simulated diurnal heating is too weak, the Δ SLP range, defined previously as the peak-to-trough difference of the sea-level pressure difference between FWL and the ocean sounding site before 15 UTC (as discussed in Section 2.3.2), is only ~ 1 hPa (Fig. 3.4e). The underestimated simulated air temperature also causes the simulated relative humidity to be too high at all times despite the simulated water vapor mixing ratio agreeing well with the observation (Figs. 3.4c-d).

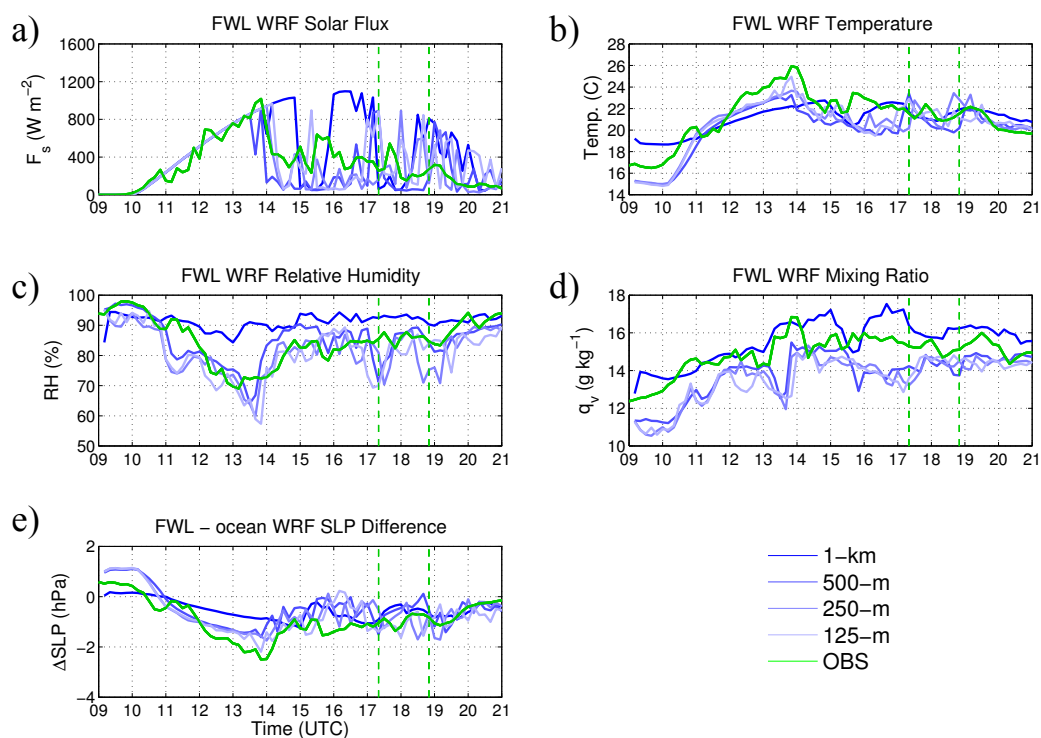


Figure 3.4. April 18th FWL observations (green line) compared to those simulated in the four control simulations: a) solar radiation flux, b) 2-m air temperature, c) 2-m relative humidity, d) 2-m water vapor mixing ratio, and e) sea-level pressure difference between FWL and the ocean sounding site.

In contrast to the CTL-1000E2 simulation, the 500-m (CTL-500E2), CTL-250E2, and 125-m (CTL-125E2) grid spacing simulations all agree better with the observations on the representation of the diurnal cycle. As expected, the air temperature increases as the incoming solar radiation increases after sunrise (Figs. 3.4a-b). The simulations also agree well with the observed cumulus development time. Once the simulated cumulus

convection develops at ~14 UTC, the incoming solar flux decreases and the air temperature drops. Despite a negative temperature bias of ~2°C in these runs, the diurnal temperature range is already 9°C by this time, which agrees better with the observation. The maximum SLP difference between FWL and the sounding site before 15 UTC is ~0.5 hPa too high because of the -2°C air temperature bias in these simulations (Fig. 3.4e). However, a diurnal Δ SLP range of ~3 hPa is accurately predicted. The only systematic disagreement between the 500-m, 250-, and 125-m grid spacing control simulations and observations is in their under-prediction of q_v (Fig. 3.4d). This bias may be caused by too much mixing of dry, free-atmospheric air into the boundary layer. This is consistent with the underestimated FWL air temperatures, which may also arise from the overly strong mixing of heated surface air with overlaying cooler air. Otherwise, the smaller grid spacing control simulations simulate the meteorological conditions at FWL better than the CTL-1000E2 simulation.

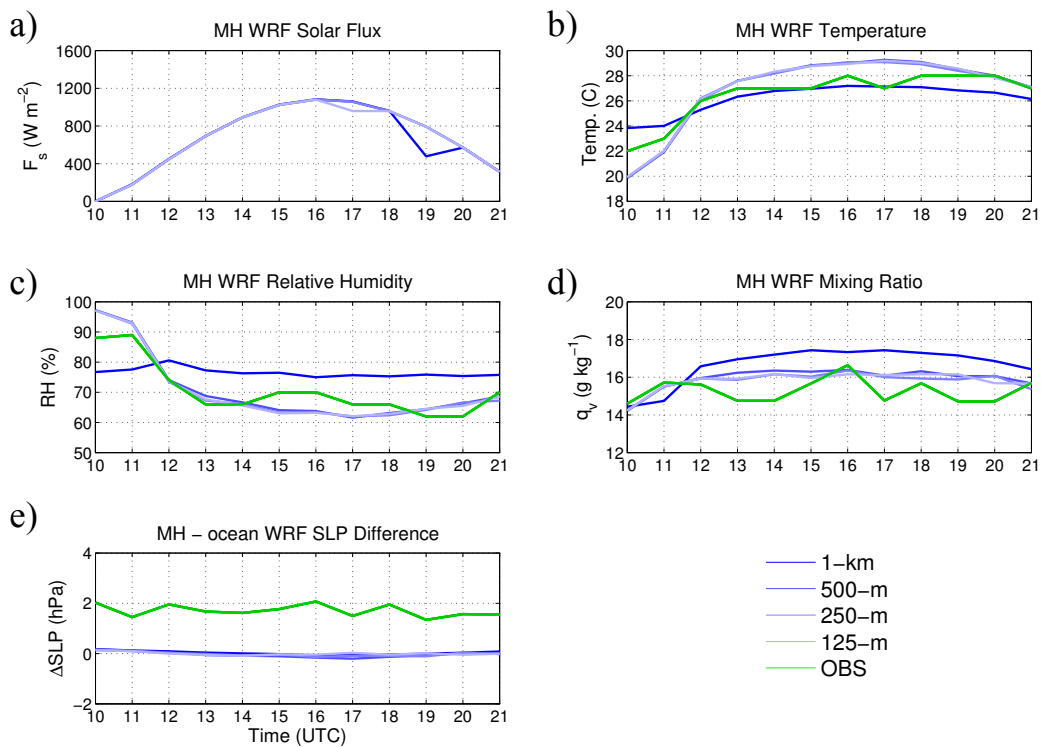


Figure 3.5. Same as in Figure 3.4, but for MH.

The CTH-1000E2 run simulate the air temperature at Melville Hall airport (MH) well (Fig. 3.5b), but show large errors in the simulated RH and q_v (Figs. 3.5c and 3.5d). In the CTL-500E2, CTL-250E2, and CTL-125E2 simulations, despite the initial air temperature being $\sim 2^\circ\text{C}$ too cold and the maximum air temperature $\sim 2^\circ\text{C}$ too warm (Fig. 3.5b), the simulated RH and q_v evolutions agree well with the observations (Figs. 3.5c and 3.5d). The model appears to simulate the SLP difference between MH and the ocean sounding site poorly in all grid spacings (Fig. 3.5e). However, we suspect that instrument bias or calibration error may have caused the pressure measurement at MH to be ~ 2 hPa higher than the ocean measurement at all times. Thus, the model may actually have simulated a realistic diurnal cycle in MH-ocean sea-level pressure difference. Since MH is close to the coast and oceanic air continuously mixes with the island boundary layer, the heating is confined over a shallower layer at MH. As a result, the thermally-driven pressure anomaly at MH is not as significant as the one at FWL despite the similar degree of surface warming.

3.2.3 Flight track comparison

The model data were interpolated onto the six over-island legs flown on April 18th. Because the smallest scale that the model can resolve depends on its grid spacing, we interpolated the simulation results onto the flight tracks using a spacing equal to the model grid spacing. To enable fairer comparisons between the observations and the model at different grid spacings, we also averaged the WKA flight track data into 1-km, 500-m, 250-m, and 125-m grid spacings. Figure 3.6 shows the simulated vertical velocity variance (σ_w^2) averaged separately along Legs 3 and 4 for all points over the island (elevation > 1 m) and the island rain rate for the entire simulation. We compare the

simulated Legs 3 and 4 flow and in-cloud properties at different grid spacings to the WKA over-island observations in Tables 3.1 and 3.2.

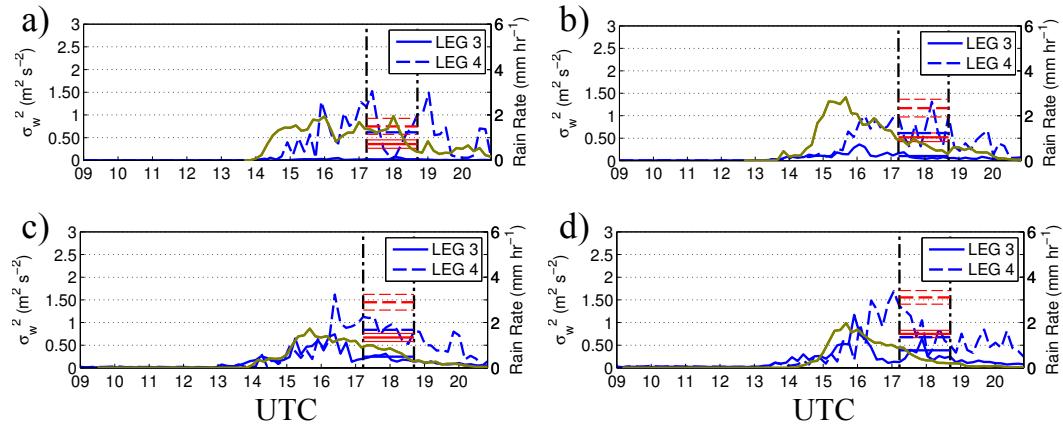


Figure 3.6. Simulated vertical velocity variance averaged separately along all Leg 3s and Leg 4s for the whole simulation: a) 1-km, b) 500-m, c) 250-m, and d) 125-m grid spacing simulations. The island rainfall rate (olive-colored solid line) is also plotted. The thick solid (dashed) red line denotes the observed vertical velocity variance averaged for all Leg 3s (Leg 4s) and the thin solid (dashed) red lines denote the upper and lower bounds of the observed vertical velocity variance standard error for all Leg 3s (Leg 4s).

As shown in Figure 3.6, the σ_w^2 are nearly zero along both legs until ~ 13 UTC when the cumulus convection begins to form. In all control simulations, the model simulates a greater σ_w^2 along Leg 4 than along Leg 3. This agrees with the observation where the Leg 4 σ_w^2 was about twice as large as the Leg 3 σ_w^2 (Tables 3.2 and 3.3), which likely arises from the northeasterly background winds shifting the primary island convergence line to the western side of the island. Precipitation begins at ~ 14 UTC and the simulated flight track σ_w^2 peaks just after the maximum rain rate in all simulations (Fig. 3.6). However, while cloud shadowing and precipitation may have created cold pools that initially intensified the simulated convection, they likely ultimately cooled the air over higher terrains and weakened the thermal circulations that drove the cumulus convection. We investigate the weakening of thermal circulations due to these convection feedbacks in more detail in Section 3.5.

OBS	σ_w^2 ($m^2 s^{-2}$)	U ($m s^{-1}$)	V ($m s^{-1}$)	W_{core} ($m s^{-1}$)	B_{core} ($cm s^{-2}$)	Q_{cld} (g m^{-3})	$M_{v,nor}$ (kg $m^{-2} s^{-1}$)	σ_{cld}
1000-m	0.35	3.64	0.82	0.62	0.60	0.2571	0.055	0.25
500-m	0.52	3.65	0.84	0.94	0.74	0.3176	0.083	0.22
250-m	0.67	3.66	0.83	1.45	0.49	0.3845	0.095	0.18
125-m	0.75	3.66	0.82	1.24	0.50	0.4068	0.101	0.16
WRF	σ_w^2 ($m^2 s^{-2}$)	U ($m s^{-1}$)	V ($m s^{-1}$)	W_{core} ($m s^{-1}$)	B_{core} ($cm s^{-2}$)	Q_{cld} (g m^{-3})	$M_{v,nor}$ (kg $m^{-2} s^{-1}$)	σ_{cld}
CTL-1000E2	0.02	2.42	0.67	NaN	NaN	0.0000	0.000	0.00
CTL-500E2	0.10	2.72	0.60	1.72	0.37	0.2645	0.014	0.04
CTL-250E2	0.31	2.68	0.58	1.61	0.44	0.3829	0.061	0.14
CTL-125E2	0.28	2.62	0.79	1.11	0.45	0.3912	0.063	0.13

Table 3.1. Observed vs. simulated Leg 3 flow and in-cloud measurements in four different grid spacings: vertical velocity variance (σ_w^2), u-component wind (U), v-component wind (V), cloud-core vertical velocity (W_{core}), cloud-core buoyancy (B_{core}), cloud liquid water content (Q_{cld}), distance-normalized vertical cloud mass flux ($M_{v,nor}$), and cloud fraction (σ_{cld}).

OBS	σ_w^2 ($m^2 s^{-2}$)	U ($m s^{-1}$)	V ($m s^{-1}$)	W_{core} ($m s^{-1}$)	B_{core} ($cm s^{-2}$)	Q_{cld} (g m^{-3})	$M_{v,nor}$ (kg $m^{-2} s^{-1}$)	σ_{cld}
1000-m	0.74	-0.49	-0.54	2.24	0.61	0.3811	0.183	0.34
500-m	1.16	-0.54	-0.54	2.09	0.61	0.4170	0.208	0.30
250-m	1.45	-0.53	-0.55	2.14	0.77	0.5238	0.238	0.25
125-m	1.56	-0.53	-0.55	2.25	0.83	0.5610	0.251	0.22
WRF	σ_w^2 ($m^2 s^{-2}$)	U ($m s^{-1}$)	V ($m s^{-1}$)	W_{core} ($m s^{-1}$)	B_{core} ($cm s^{-2}$)	Q_{cld} (g m^{-3})	$M_{v,nor}$ (kg $m^{-2} s^{-1}$)	σ_{cld}
CTL-1000E2	0.62	1.08	0.59	2.46	1.27	0.8175	0.161	0.13
CTL-500E2	0.61	0.74	0.49	1.95	0.92	0.5865	0.118	0.12
CTL-250E2	0.84	0.49	0.60	2.85	1.51	0.6246	0.177	0.11
CTL-125E2	0.77	0.41	0.26	2.45	1.37	0.6215	0.156	0.12

Table 3.2. Same as in Table 3.1, but for Leg 4s.

Although it appears that the 1-km grid spacing simulation best simulates the Leg 4 σ_w^2 out of the four control simulations (Table 3.2), this simulation produces large errors in other quantities. Both the Leg 4 W_{core} and B_{core} are too large in this simulation because the clouds are poorly resolved and may experience unrealistically low entrainment rates due to their overly large size. As result, they become too strong, contain too much liquid water (Table 3.2), and produce too much rainfall over the high terrains (Table 3.3).

Figure 3.7a shows the first model-level flow divergence from the CTL-1000E2 simulation at 17 UTC. In this simulation, the precipitation cold pools displace the strongest convergence toward Dominica's west coast. Thus, most of the cumulus convection is concentrated along Leg 4. In addition, too much westerly momentum is simulated along Leg 4 likely because the overly deep convection produces the main easterly outflows above the WKA flight level. Thus, the simulated u-wind component along Leg 4 also does not agree well with the observation (Table 3.2).

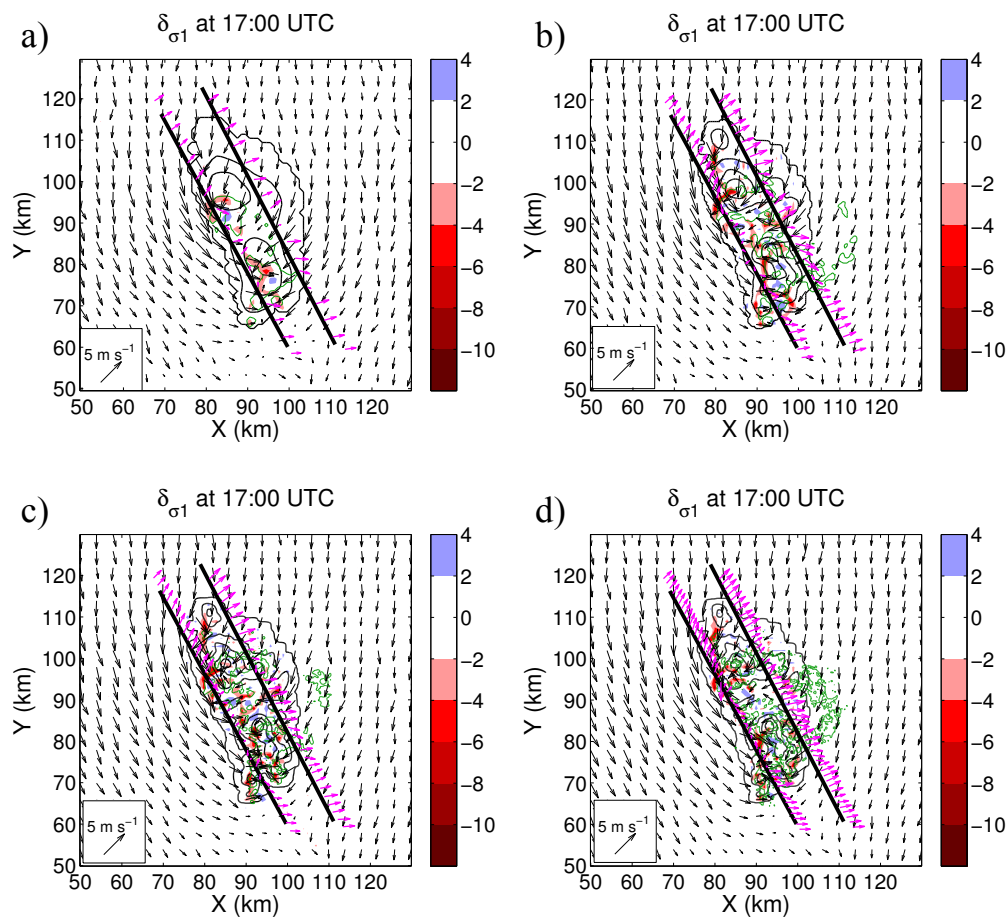


Figure 3.7. Same as in Figure 3.2, but at 17 UTC.

In contrast to Leg 4, almost no clouds form along Leg 3 because the strongest lifting shifts over to Dominica's lee slopes (Fig. 3.7a). As a result, the 1-km simulation

simulates a nearly zero σ_w^2 along Leg 3 (Table 3.1). The under-simulated M_v and σ_{clid} along Leg 3 also support this finding. Overall, it appears that errors in the representation of clouds and precipitation in the 1-km simulation fundamentally changes the flow dynamics over the island.

	OBS	CTL-1000E2	CTL-500E2	CTL-250E2	CTL-125E2
Max. Rainfall (mm)	< 2	54.4	64.1	58.1	40.0
Avg. Rainfall (mm)	< 2	5.5	4.8	3.5	2.8

Table 3.3. The Guadeloupe radar-derived rainfall and simulated maximum and averaged rainfall over Dominica in 1-km, 500-m, 250-m, and 125-m grid spacing control simulations.

As the grid spacing decreases, the simulated W_{core} along Legs 3 and 4 agree better with the observations. Leg 4 B_{core} approaches the observations as the grid spacing decreases from 500-m to 125-m as well, but they are still too large compared to the observation (Table 3.2). This partially explains the continued over-prediction of island rainfall (Table 3.3). Along with modest reductions to the maximum rainfall, the average rainfall also decreases as the grid spacing decreases. As a consequence, the cold pools weaken and they are less effective at displacing the main convergence line over the high terrain. Since the convergence lines in the CTL-500E2, CTL-250E2, and CTL-125E2 simulations concentrate more in between Legs 3 and 4, the strongest convection also shifts toward the island's center (Fig. 3.7b-d). Consequently, the simulated σ_w^2 increases along Leg 3 compared to the 1-km grid spacing simulation. In addition, since the simulated convection is shallower, it produces stronger easterly outflows along Leg 4. Thus, the horizontal wind components also agree better with the observations as the grid spacing decreases (Tables 3.1 and 3.2). Even though the simulated Leg 4 σ_w^2 appear to agree less with the observation in these simulations than in the 1-km grid spacing simulation, they are generally within a factor of 2 of the observations.

The above results suggest that certain parameters (e.g island rainfall) might verify even better if we had further decreased the simulation's grid spacing to below 125 m. However, since the results does not seem to improve significantly going from 250-m to 125-m grid spacing, we decide to do our future sensitivity tests at 250-m grid spacing. Doing so, we ensure that the model reasonable represents thermally-driven flow pattern over Dominica while limiting the computational expense.

Section 3.3 Mechanical vs. thermal forcing

As previously discussed in Chapter 1, vertical motions arise when a flow is mechanically lifted by an orography or when thermally-driven upslope flows are generated. Moist convection initiates if the vertical motions are strong enough to lift air parcels up to their LFC. Since the background winds during April 18th were weak, mechanically-forced ascent should have a minimal contribution on convection initiation. Here we isolate the impacts of pure mechanical and pure thermal forcing to better understand their individual contributions.

The first sensitivity experiment (MC) isolates the mechanical forcing by turning off the surface heat fluxes. However, the surface layer scheme was kept on to capture the island surface's frictional effects. Since this simulation does not consider the surface heat fluxes, we turned off the 80 W m^{-2} of latent heat removal below the subcloud layer as well as the radiation schemes and the positive temperature tendency so that a quasi-steady state can be maintained. The second sensitivity experiment (TH) isolates the thermal forcing by flattening Dominica's terrain such that grid points where the terrain

height is > 2 m were set to 2 m above sea-level. In this simulation, limited mechanically-forced ascent can be generated since there is no orography to lift the background flow.

Early in the day, an eastward propagating land-breeze front is found in both the control (CTL-250E1) and TH simulations as the cooler land air diverges away from the island and collides with the northerly background winds off Dominica's east coast (Figs. 3.8a-b). The land breeze in the TH simulation appears weaker since there is no downslope flow to accelerate the land-breeze fronts. No land breeze develops in the MC simulation since the air over the island does not emit longwave radiation.

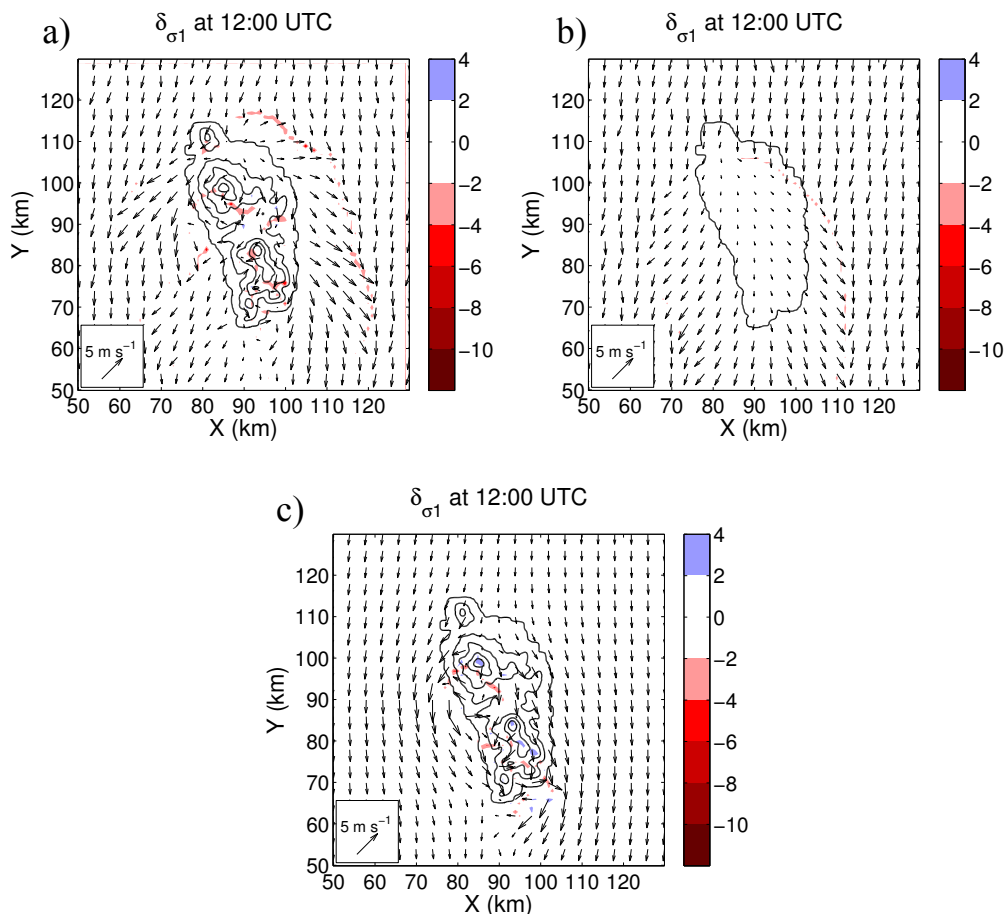


Figure 3.8. First model-level horizontal winds, flow divergence (filled contours, same scale as in Figure 3.1), and cloud liquid water path (green contours $> 0.1 \text{ g m}^{-2}$) from a) CTL-250E1, b) TH, and c) MC simulations at 12 UTC.

Figure 3.9 shows the time evolution of surface equivalent potential temperature, moist instability, horizontal and vertical (cloud) mass fluxes, and various cloud-core properties at 1800 m (the same height as the WKA legs 3 and 4) averaged over the island. As the day progresses, the island air temperature increases in both the CTL-250E1 and TH simulations, but remains steady in the MC simulation (Fig. 3.9a). Similarly, the island-averaged CAPE increases in both the CTL-250E1 and TH simulations, but no CAPE builds up in the MC simulation (Fig. 3.9b). The island flow in the CTL-250E1 and TH simulations begins to switch from divergent to convergent at ~12 UTC, as indicated by the development of positive island-scale horizontal mass flux vertically-integrated up to the lowest level of non-divergence (Fig. 3.9c, M_h , see Appendix for calculation), but it remains weakly divergent in the MC simulation due to the orographic blocking of incoming airflow. During the transition, the land-breeze fronts in the CTL-250E1 and TH simulations gradually dissipate and sea-breeze fronts develop over Dominica's east and west coasts in the TH simulation (Fig. 3.10b). However, sea-breeze fronts are not visible in the CTL-250E1 simulation probably because the upslope flows have overwhelmed the sea-breeze circulations (Fig. 3.10a). In the MC simulation, neither upslope nor sea-breeze flow develops (not shown).

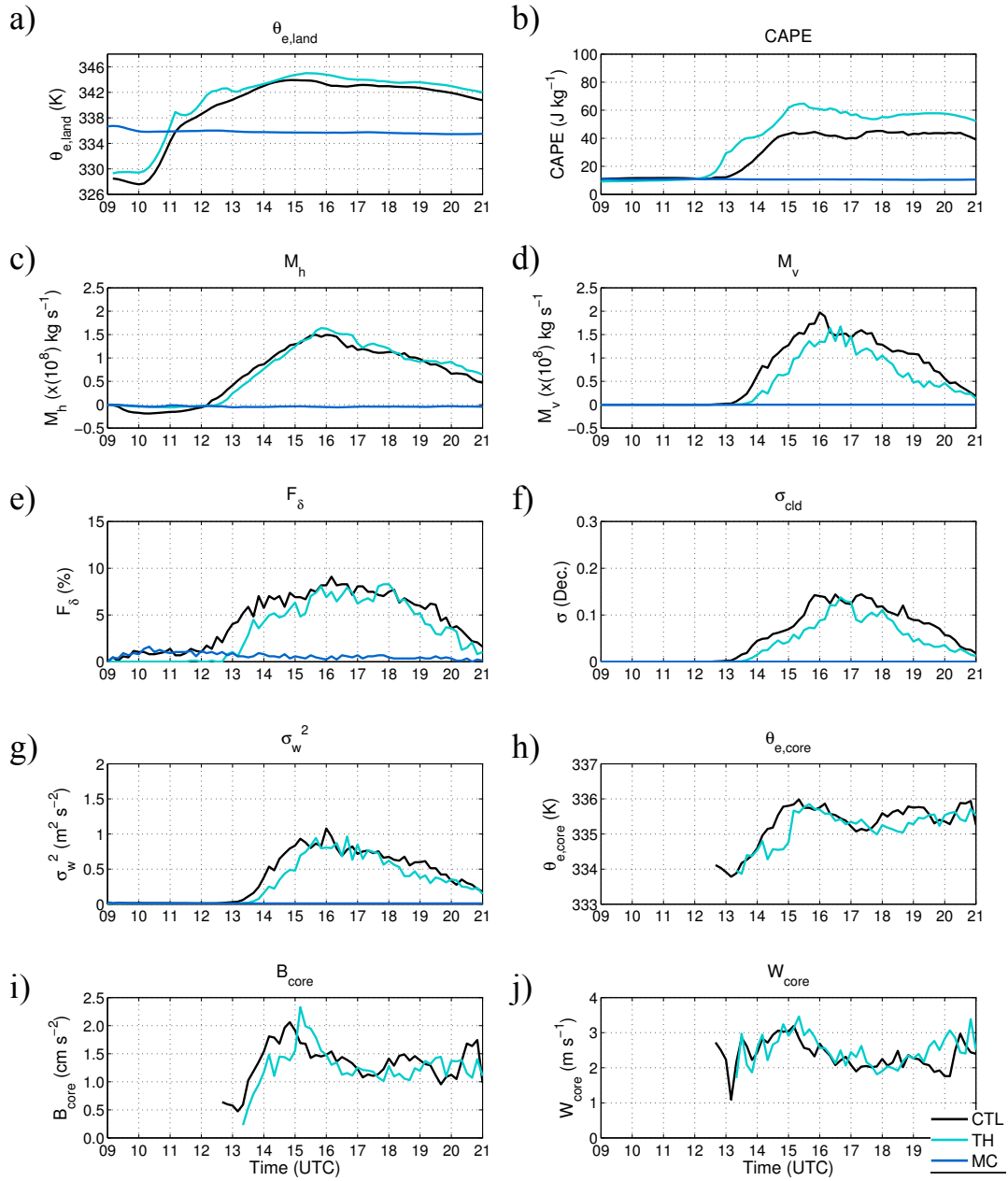


Figure 3.9. Comparisons of thermal circulation strength and cumulus vigor between the CTL-250E1, MC, and TH simulations: a) island-averaged 2-m equivalent potential temperature, b) island-averaged CAPE, c) vertically-integrated island-scale horizontal mass flux up to the lowest level of non-divergence, d) integrated vertical cloud mass flux at the WKA flight-level, e) first model-level convergence fraction (Divergence $< -4 \times 10^{-3}\ s^{-1}$) over the island, f) island cloud fraction g) island vertical velocity variance at the WKA flight-level, h) island cloud-core equivalent potential temperature, i) island cloud-core buoyancy, and j) island cloud-core vertical velocity.

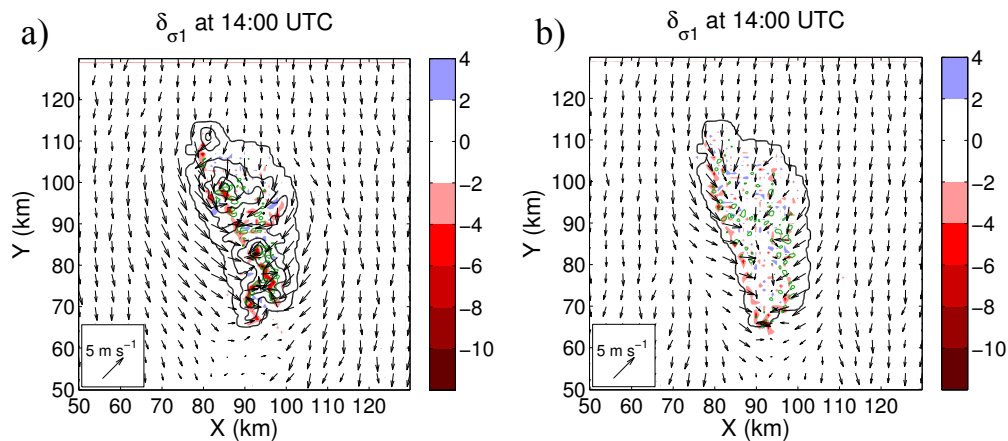


Figure 3.10. First model-level horizontal winds, flow convergence, and liquid water path from a) the CTL-250 and b) TH simulations at 14 UTC. Note the upslope convergence over the summits in the CTL-250 simulation and the sea-breeze fronts in the TH simulation.

As seen from Fig. 3.9f, cumulus convection initiates at ~ 13 UTC in both the CTL-250E1 and TH simulations. The near-surface flow convergence maximizes at ~ 15 UTC when the upslope flows in the CTL-250E1 simulation reach their greatest intensity, as well as when the sea-breeze fronts in the TH simulation converge near the island's center (not shown). Around this time, the cumulus-vigor parameters (e.g M_v , see Appendix for calculation, σ_{cld} , B_{core} , and W_{core}) show a slight positive jump (Figs. 3.9f, i, and j). Convective precipitation is produced in both the CTL-250E1 and TH simulations at around 16 UTC, which suggests that it is triggered by the intense updrafts generated when the upslope flow or sea-breeze convergence peaks. Precipitation cold pools then disrupt the convergence zones and cut off warm air inflow feeding into the clouds, which partially explains the sudden decline of cumulus vigor after ~ 16 UTC. Otherwise, subsidence warming associated with compensating descent may also warm the surrounding air, which limits the parcel-surrounding density contrast and reduces B_{core} (Kirshbaum and Smith, 2009). The gradual decrease of solar heating with lowering solar zenith angle may also explain the weakening of thermal circulations after 16 UTC.

Finally, σ_{cld} in the MC simulation remains zero throughout the day (Fig. 3.9f) because the background flow is too weak to ascend over Dominica's orography since Fr calculated from the April 18th sounding is < 1 (see Table 2.1).

	CTL-250E1	MC	TH
Max. Rainfall (mm)	58.1	0.0	20.8
Avg. Rainfall (mm)	3.5	0.0	2.1
Time-Int. M_h ($\times 10^{12}$ kg)	2.88	-0.17	3.04
Time-Int. M_v ($\times 10^{12}$ kg)	2.97	0.00	2.04

Table 3.4. Simulated maximum and averaged island rainfall, time-integrated horizontal mass flux up to the lowest level of non-divergence, and time-integrated vertical cloud mass flux at the WKA flight level for the control (CTL-250E1), mechanical forcing-only (MC), and thermal forcing-only simulations (TH).

Previous studies (e.g Mahrer and Pielke, 1977) have suggested that thermally-driven mountain circulations could combine with sea-breeze circulations to produce stronger anabatic flows. If such is the case, taller mountains should generate stronger updrafts and trigger more vigorous cumulus convection. According to Table 3.4, more precipitation is produced in the CTL-250E1 simulation than in the TH simulation, indicating that the convection is perhaps more vigorous due to the orography. However, the flight-level in-cloud parameters such as B_{core} and W_{core} do not differ significantly between the two simulations (Figs. 3.9i-j). Furthermore, the time-integrated M_h for the entire simulation in the CTL-250E1 simulation is slightly less than that in the TH simulation (Table 3.4).

To better understand why orography appears to weaken the thermal circulations, we investigate the vertical profiles of island-scale horizontal mass flux. These profiles indicate that the depth of positive mass flux in the TH simulation is ~ 100 m shallower than that in the CTL-250E1 simulation, but its near-surface mass flux is $\sim 0.5 \times 10^8 \text{ kg s}^{-1}$ larger than that in the CTL-250E1 simulation after 15 UTC (Fig. 3.11). If we integrate the island-scale horizontal mass flux vertically up to the lowest level of non-divergence, the

resulting value in the CTL-250E1 simulation is smaller than that in the TH simulation. Thus, the elevated terrain over the island apparently weakens the thermal circulations. We consider the following hypothesis for this result: to complete a thermal circulation, the elevated outflow over the mountain must descend through a deeper stable cloud layer than the shallower circulation in the TH simulation. Because this stable layer inhibits vertical motion, it suppresses both the convective outflow and inflow, thus weakening the island-scale circulations.

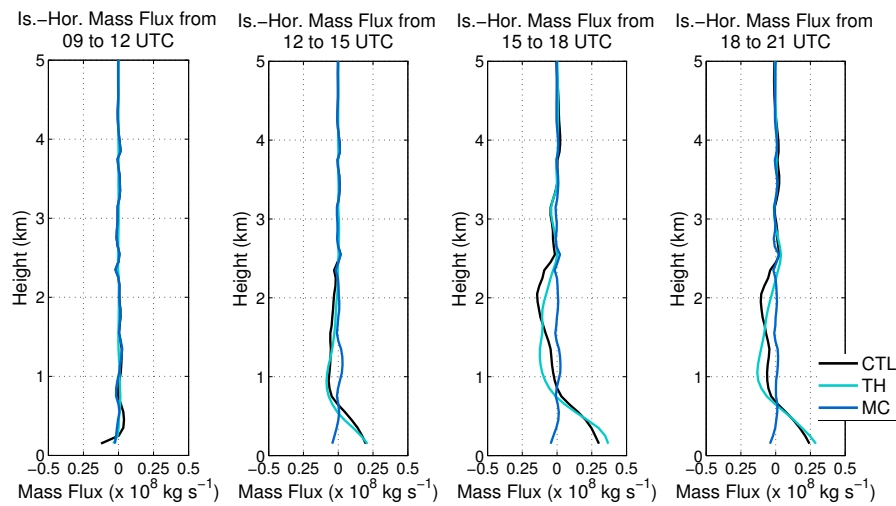


Figure 3.11. 3-hrly. island-scale horizontal mass flux profile from the pure mechanical forcing vs. pure thermal forcing sensitivity tests. Note that despite the lowest positive mass flux layer in the CTL-250E1 simulation is deeper, the surface horizontal mass flux in this simulation is smaller than that in the TH simulation.

Despite the weaker island-circulations in the CTL-250E1 simulation than in the TH simulation, M_v is higher in the CTL-250E1 simulation than in the TH simulation. We hypothesize that this counterintuitive finding arises from the following: in contrast to the TH case, where most convergence is focused along the sea-breeze fronts, the heterogeneous terrain of the CTL-250E1 case creates many localized convergence zones that all serve as foci for convection initiation. This perhaps explains why the island convergence fraction (F_δ , Fig. 3.9e), defined as the fraction of island area where the first

model-level flow convergence exceeds $4 \times 10^{-3} \text{ s}^{-1}$, is significantly higher in the CTL-250E1 simulation than in the TH simulation. Finally, the absence of anabatic flow convergence and cumulus convection (Fig. 3.9) in the MC simulation suggests that mechanical forcing plays a minimal role in convection initiation.

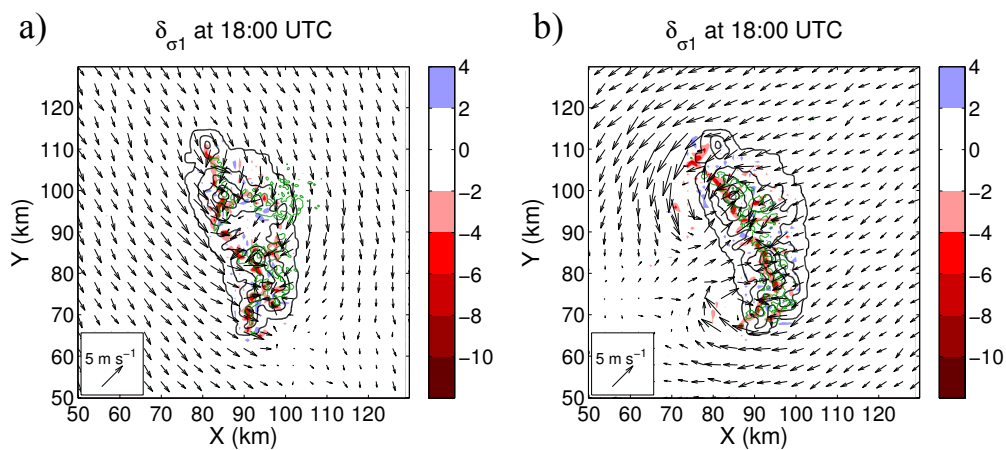
Section 3.4 Background wind velocity

Previous studies on thermally-driven convection have discovered a strong sensitivity of convection strength to the background wind velocity (e.g Hagen et al., 2011). During the four DOMEX weak trade-wind cases, the background wind speeds below 1 km ranged from $\sim 2 \text{ m s}^{-1}$ on the 18th, 19th, and 21st to $\sim 5 \text{ m s}^{-1}$ on the 15th. While weaker winds on the 18th and 19th favored stronger thermal circulations and moist convection, stronger winds on the 15th inhibited the convection (owing to the downwind ventilation of island heating). Here we study how the wind speed and direction influence the strength of thermal circulations and associated cumulus convection.

The WKA upstream sounding on April 18th recorded north-north easterly background winds of $\sim 3 \text{ m s}^{-1}$ below 1 km. In the first wind-sensitivity experiment (along-barrier winds or AW), we rotated the upstream sounding winds below 1 km to make them blow parallel to Dominica's dominant ridgeline (angled $\sim 120^\circ$ counter-clockwise from due east) without changing the mean wind speed within this layer. In the second simulation (cross-barrier winds or CW), we rotated the winds below 1 km to make them blow perpendicular to Dominica's dominant ridge line. To test the convection's sensitivity to the background wind speed, we doubled the initial sounding wind speeds below 1 km in our third simulation (double winds or DW) and halved the

wind speeds over the same layer in our fourth simulation (half winds or HW). Since increasing (decreasing) the surface wind speed increases (decreases) the evaporation rate of ocean water, we repeated the 2-D test simulations from the control simulation with the DW and HW soundings and obtained new latent-heat fluxes of 100 W m^{-2} (for DW) and 50 W m^{-2} (for HW) that are removed from the subcloud layer to maintain a steady state. To prevent wind velocity discontinuity at the 1-km interface in all of the experiments described above, we linearly relaxed the changes to the sounding winds to the values in the control simulation over the 1-2 km layer.

Despite different locations of land breeze fronts and upslope flow convergence between the simulations, the evolution of thermally-driven flows is rather similar. Since the goal of our study is to understand the thermally-driven convection, we skip the early-morning flow pattern and focus our analysis on the afternoon thermally-driven circulations and associated cumulus convection. The plots of first-model level winds, flow divergence, and cloud liquid water path at 18 UTC show that thermally-driven flow and convection develop in all four sensitivity simulations (Fig. 3.12).



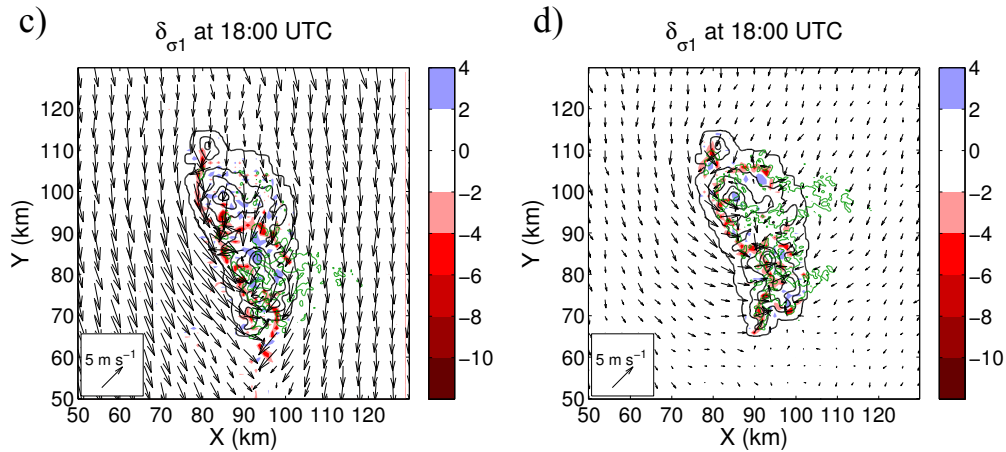
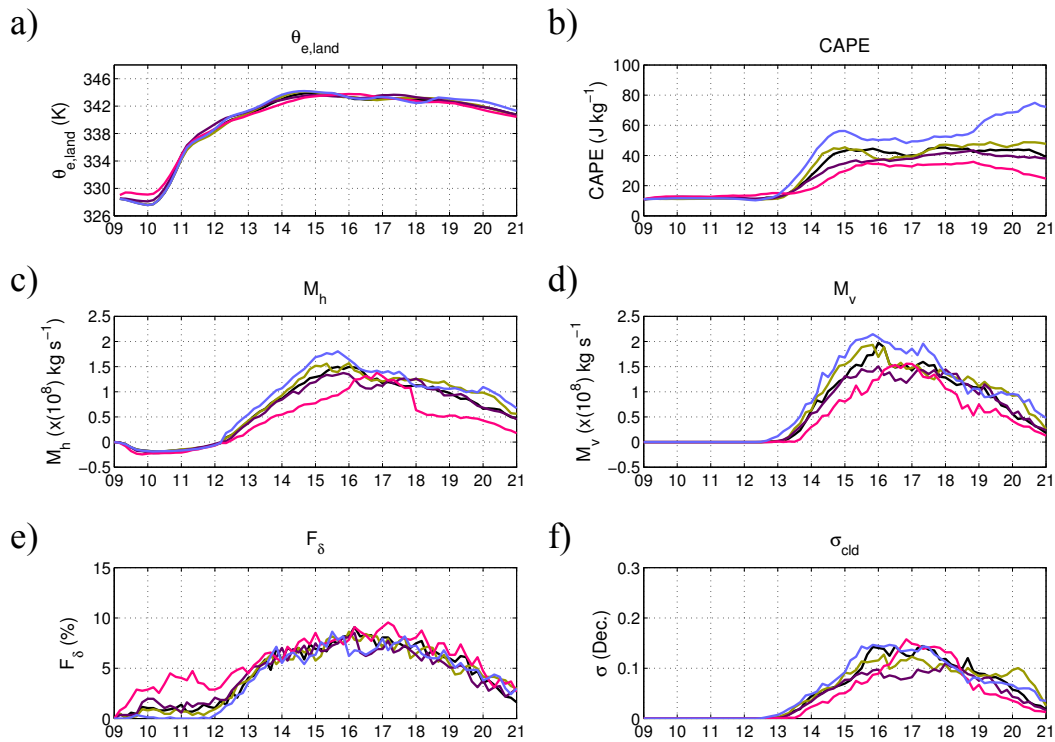


Figure 3.12. First model-level horizontal winds, first model-level flow divergence, and cloud liquid water path for the wind-sensitivity simulations: a) along-barrier winds (AW), b) cross-barrier winds (CW), c) doubled wind speeds (DW), and d) halved wind speeds (HW) at 18 UTC.

Like in the CTL-250E1 simulation, the air temperature begins to warm in all four wind-sensitivity simulations once the solar heating kicks in. The island-averaged surface θ_e in the AW and HW simulations is 1-2 K warmer than that in the CW and DW simulations, especially before 16 UTC (Fig. 3.13a). This is because the air parcels spend more time over land and absorb more heat. In response to the greater warming, stronger thermal circulations develop in both the AW and HW simulations as indicated by their larger M_h (Fig. 3.13c, Table 3.5). The cloud parcels in the AW and HW simulations are also warmer than those in the CW and DW simulations as they feed in the warmer subcloud-layer air (Fig. 3.13h). In addition, the CAPE in the AW and HW simulations is higher than that in the CW and DW simulations (Fig. 3.13b). As a result, the cloud cores in the AW and HW simulations are more buoyant than the ones in the CW and DW simulations, especially before 16 UTC (Fig. 3.13i). Due to the stronger surface forcing and greater background moist instability, cumulus clouds in the AW and HW simulations are more vigorous than those in the CW and DW simulations, as indicated by their greater M_v (Fig. 3.13d, Table 3.5). Consequently, the maximum rainfall and averaged

rain rate are also both larger in the AW and HW simulations than those in the CW and DW simulations (Table 3.5). Due to cloud shadowing, precipitation cooling, and lowering solar zenith angle, B_{core} and W_{core} appear similar between all simulations later in the day (Fig. 3.13i-j). Furthermore, note that the results from AW simulation are rather similar to the CTL-250E1 simulation because the low-level winds in the CTL-250E1 simulation are already blowing nearly parallel to Dominica's north-to-south oriented terrain.



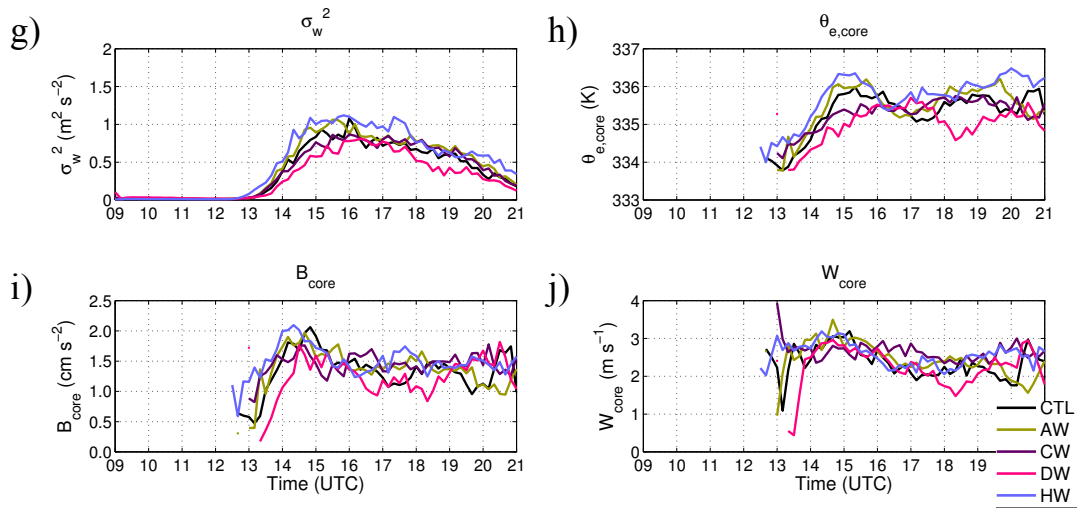


Figure 3.13. Same as in Figure 3.9, but for the wind sensitivity tests.

	CTL-250E1	AW	CW	DW	HW
Max. Rainfall (mm)	58.1	44.5	30.6	26.4	63.8
Avg. Rainfall (mm)	3.5	5.0	2.1	2.9	4.7
Time-Int. M_h ($\times 10^{12}$ kg)	2.88	3.16	2.73	1.90	3.46
Time-Int. M_v ($\times 10^{12}$ kg)	2.97	3.31	2.77	2.21	3.72

Table 3.5. Same as in Table 3.4, but for the wind velocity sensitivity tests.

Overall, the above results suggest that the thermal circulations intensify when the background winds are weak or blow parallel to Dominica's long axis. On the other hand, when the background winds are strong (but below the threshold for mechanically-forced convection) or blow perpendicularly to Dominica, the thermal circulations weaken. To test the robustness of this result, we performed another simulation where we doubled the low-level wind speeds and made them blow cross-barrier-wise to the island. The cumuli produced in this simulation are the weakest among all wind-sensitivity simulations (not shown). Therefore, other than the reduced solar heating due to large-scale cloud cover, stronger low-level background winds also likely suppressed cumulus convection on April 15th. In contrast, weaker background winds on the 18th and 19th favored vigorous cumulus convection over the island in addition to abundant solar heating.

Section 3.5 Cloud and precipitation feedbacks

As discussed in Section 1.4, thermally-driven convection creates various feedback mechanisms that can substantially modify its parent thermal circulation. During April 18th, cloud shadowing by the thermally-driven cumuli apparently have weakened the thermal circulations after 14 UTC, as indicated by the reduced SLP contrast between FWL and the ocean sounding site at the time of WKA over-island observations (Fig. 2.9f). In the current set of sensitivity tests, we wish to quantify several such feedback mechanisms, including cloud shadowing, precipitation, and cloud latent-heat release, on the island thermal circulations and convection.

The first sensitivity experiment (NORAIN) excludes precipitation by shutting off the autoconversion of cloud droplets into rain droplets. The second experiment (NOCOD) excludes the cloud-shadowing effect by neglecting cloud effects on optical depth in the shortwave radiation scheme. In other words, the clouds are "transparent" so that solar radiation still penetrates through them and heats the land surface. Finally, to quantify the cloud latent-heat release feedback, we turned off the microphysics parameterization in our third simulation (NOMP) so that neither clouds nor precipitation is produced.

Similar to the wind-sensitivity tests, the evolution of the thermally-driven upslope flows in the current set of experiments is rather similar to that in the CTL-250E1 simulation. However, the near-surface convergence zones in the NORAIN simulation are more pronounced over the island's center since no precipitation is produced to interfere with them (Fig. 3.14a). Because there is no evaporative cooling associated with precipitation, the surface θ_e in this simulation is slightly warmer than that in the CTL-250E1 simulation (Fig. 3.15a). As result, M_h in the NORAIN simulation is $\sim 10\%$ larger

than that in the CTL-250E1 simulation after 16 UTC (Fig. 3.15c), indicating that the thermal circulations are stronger than those in the CTL-250E1 simulation. Due to less surface cooling, the CAPE in the NORAIN simulation is $\sim 20 \text{ J kg}^{-1}$ larger than that in the CTL-250E1 simulation (Fig. 3.15b). The higher CAPE gives rise to more buoyant and vigorous cumulus convection (Figs. 3.15i-j), which increases the time-integrated M_v by $\sim 10\%$ compared to that in the CTL-250E1 simulation (Table 3.6). The more vigorous cumulus convection in the NORAIN simulation also leads to higher flight-level σ_w^2 (Fig. 3.15g). Overall, these results indicate that precipitation weakens the thermal circulation and the convection, thus representing a significant negative feedback.

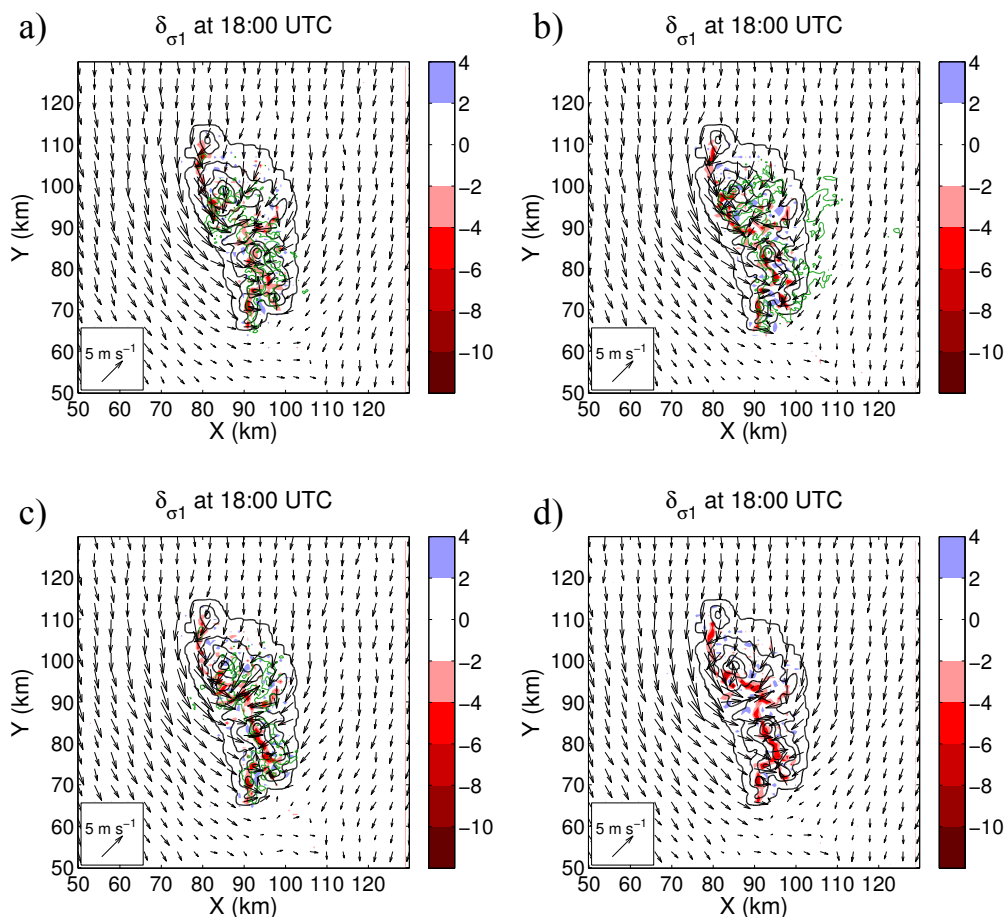


Figure 3.14. Same as in Figure 3.12, but for a) no rain (NORAIN), b) no cloud optical depth (NOCOD), c) no cloud optical depth and no rain (NOCR), and d) no microphysics (NOMP) simulations.

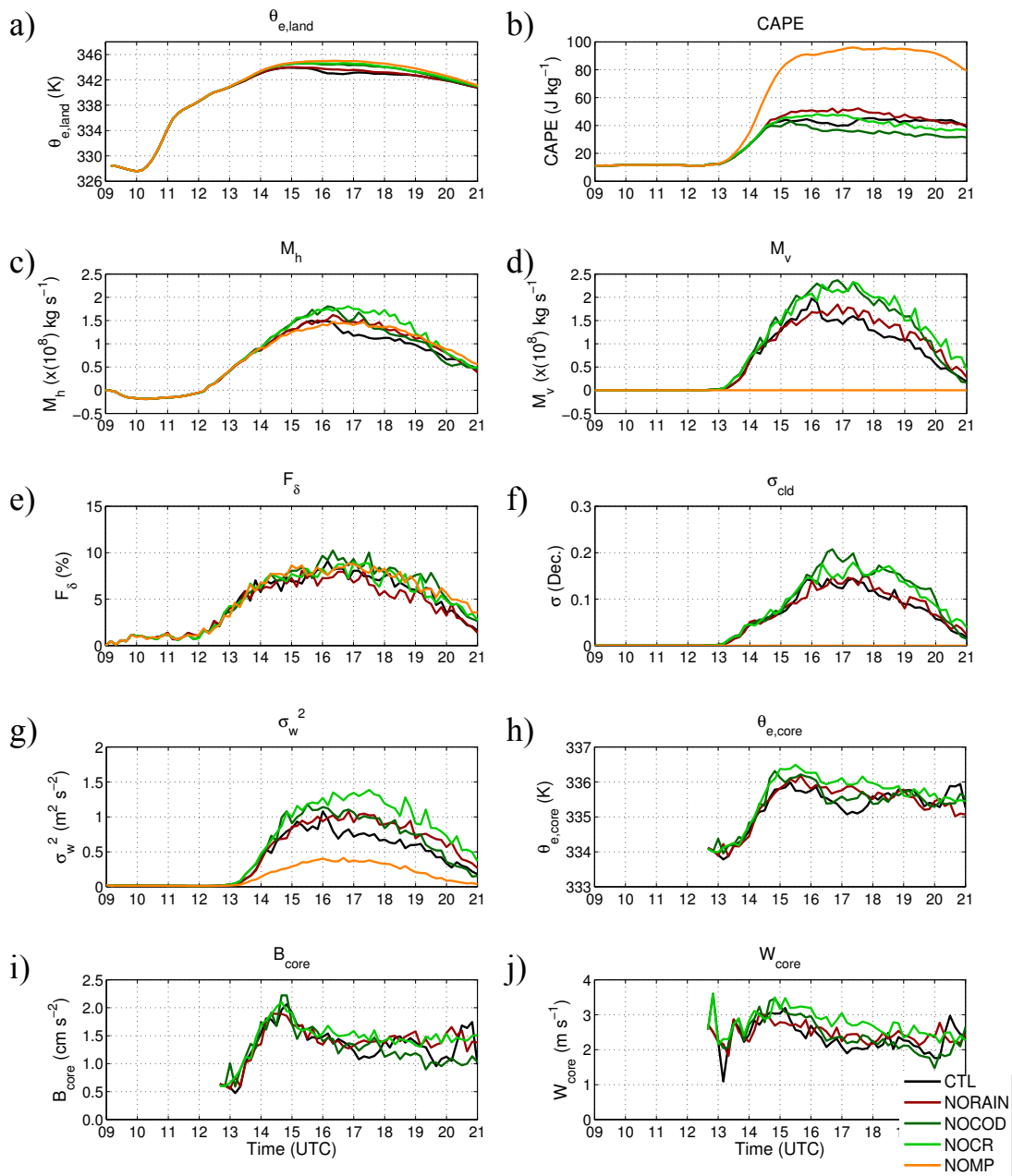


Figure 3.15. Same as in Figure 3.9, but for the cloud and precipitation feedback sensitivity tests.

	CTL-250E1	NORAIN	NOCOD	NOCR	NOMP
Max. Rainfall (mm)	58.1	0.0	106.0	0.0	0.0
Avg. Rainfall (mm)	3.5	0.0	7.8	0.0	0.0
Time-Int. M_h ($\times 10^{12}$ kg)	2.88	3.15	3.23	3.57	3.15
Time-Int. M_v ($\times 10^{12}$ kg)	2.97	3.28	4.02	4.21	0.00

Table 3.6. Same as in Table 3.4, but for the cloud and precipitation feedback sensitivity tests.

In the NOCOD simulation, the island-averaged surface θ_e is ~ 2 K warmer than that in the CTL-250E1 simulation because cooling associated with cloud shadowing has been turned off (Fig. 3.15a). Due to the greater surface air temperatures, M_h in the NOCOD simulation is 20-30% larger than that in the CTL-250E1 simulation after 15 UTC (Fig. 3.15c). The higher surface θ_e in the NOCOD simulation, however, does not increase the moist instability (Fig. 3.15b) since the increased precipitation create more subcloud cool pools that help to initiate more convection and stabilize the boundary layer (Table 3.6 and Fig. 3.15d). M_v increases because the lack of subcloud cooling associated with cloud shading enables the clouds to be more numerous and vigorous (Figs. 3.15f, i, and j). We also attribute the higher σ_{cld} to more outflow boundaries being created, which temporarily enhance the near-surface flow convergence (Fig. 3.15e). The higher σ_{cld} also leads to greater flight-level turbulence in the NOCOD simulation than in the CTL-250E1 simulation (Fig. 3.15g). Since both the thermal circulations and cumulus convection intensify in the NOCOD simulation despite the much heavier rainfall, cloud shadowing appears to have a stronger negative feedback on these phenomena than precipitation, at least given the background flows in these simulations.

To test whether the cooling induced by cloud shadowing truly affects the parent thermal circulation more than that of associated with precipitation, we performed an additional simulation (NOCR) where we turned off both the cloud optical effect and rain autoconversion. With precipitation turned off, M_h in the NOCR simulation is $\sim 20\%$ larger than that in the NOCOD simulation. Because there is no subcloud cooling associated with precipitation (Fig. 3.15a), the island-averaged CAPE in the NOCR simulation is about 15 J kg^{-1} higher than that in the NOCOD simulation (Fig. 3.15b). As a result, both B_{core} and

W_{core} in the NOCR simulation are larger than those in the NOCOD simulation (Figs. 3.15i-j). σ_{cld} , however, is less than that in the NOCOD simulation since no outflow boundary is produced to enhance F_{δ} (Figs. 3.15e-f). Despite having fewer clouds, both M_v and σ_w^2 in the NOCR simulation are comparable or even slightly larger than those in the NOCOD simulation, likely because of the more intense convection (Figs. 3.15d and g). Overall, the thermal circulations and cumulus convection intensify even further in the NOCR simulation. Since including precipitation (in the NOCOD vs. the NOCR simulation) causes a 9% decrease in the time-integrated M_h while including the cloud-optical depth (in the NORAIN vs. the NOCR simulation) causes a 12% decrease in the time-integrated M_h (Table 3.6), we conclude that cloud-shadowing has a slightly stronger negative feedback on the thermal circulations in our simulations.

Lastly, the NOMP simulation investigates the effect of cloud latent-heat release on the thermal circulation's strength. We expect the absences of cloud shadowing and precipitation evaporative cooling will lead to stronger thermal circulations. However, while the thermal circulations in the NOMP simulations are stronger than those in the CTL-250E1 simulation after 16 UTC as indicated by the greater M_h (Fig. 3.15c), M_h in this simulation is $\sim 15\%$ smaller than that in the CTL-250E1 simulation before 16 UTC. Thus, cloud latent-heat release appears to significantly enhance the thermal circulations.

Section 3.6 Cloud-layer stability

The background moist instabilities varied between the four DOMEX thermally-driven cases. The most unstable case, April 15, featured a CAPE of $\sim 1200 \text{ J kg}^{-1}$ according to the WKA sounding. However, as previously discussed, subcloud updrafts on this day were too weak to trigger widespread cumulus convection over Dominica. In

contrast, despite a CAPE of only around 100 J kg^{-1} , widespread cumulus convection developed on April 18th and 19th owing to abundant solar heating and weak background winds. Given that sufficient surface heating triggered cumulus convection on the 18th, we hope to answer two questions: 1) is background moist instability an important controlling parameter of thermal circulations and associated cumulus convection and 2) does increased latent heating associated with stronger cumulus convection enhance the overall thermal circulations?

In the first simulation (UNSTAB), we decreased the cloud-layer top (assumed 4000 m) potential temperature in the upstream sounding by 0.5 percent and linearly relaxed the cooling to zero from the cloud-layer top to the cloud-layer base (assumed 800 m). This destabilized the cloud layer and generated more positive buoyancy to accelerate air parcels upward above the LCL. The CAPE computed from the modified UNSTAB sounding is $\sim 340 \text{ J kg}^{-1}$, which is approximately three times of that on the 18th but is still about one-third of that on the 15th. However, making this change at least provides us some insights on how an increase in the background moist instability would change the thermal circulation and convection strength. In the second simulation (STAB), we increased the potential temperature at the cloud-layer top by the same percentage and linearly relaxed the warming to zero from the cloud-layer top to cloud-layer base. By doing so we stabilized the cloud layer and reduced the positive buoyancy above the LCL. The CAPE calculated from this STAB modified sounding is $\sim 25 \text{ J kg}^{-1}$, which is about one-fifth of that on the 18th. To prevent potential temperature discontinuity between the cloud-layer top and the atmosphere above, the potential temperature profile above the

cloud-layer top was increased (decreased) by the difference between the modified cloud-layer top and the original cloud-layer top potential temperatures.

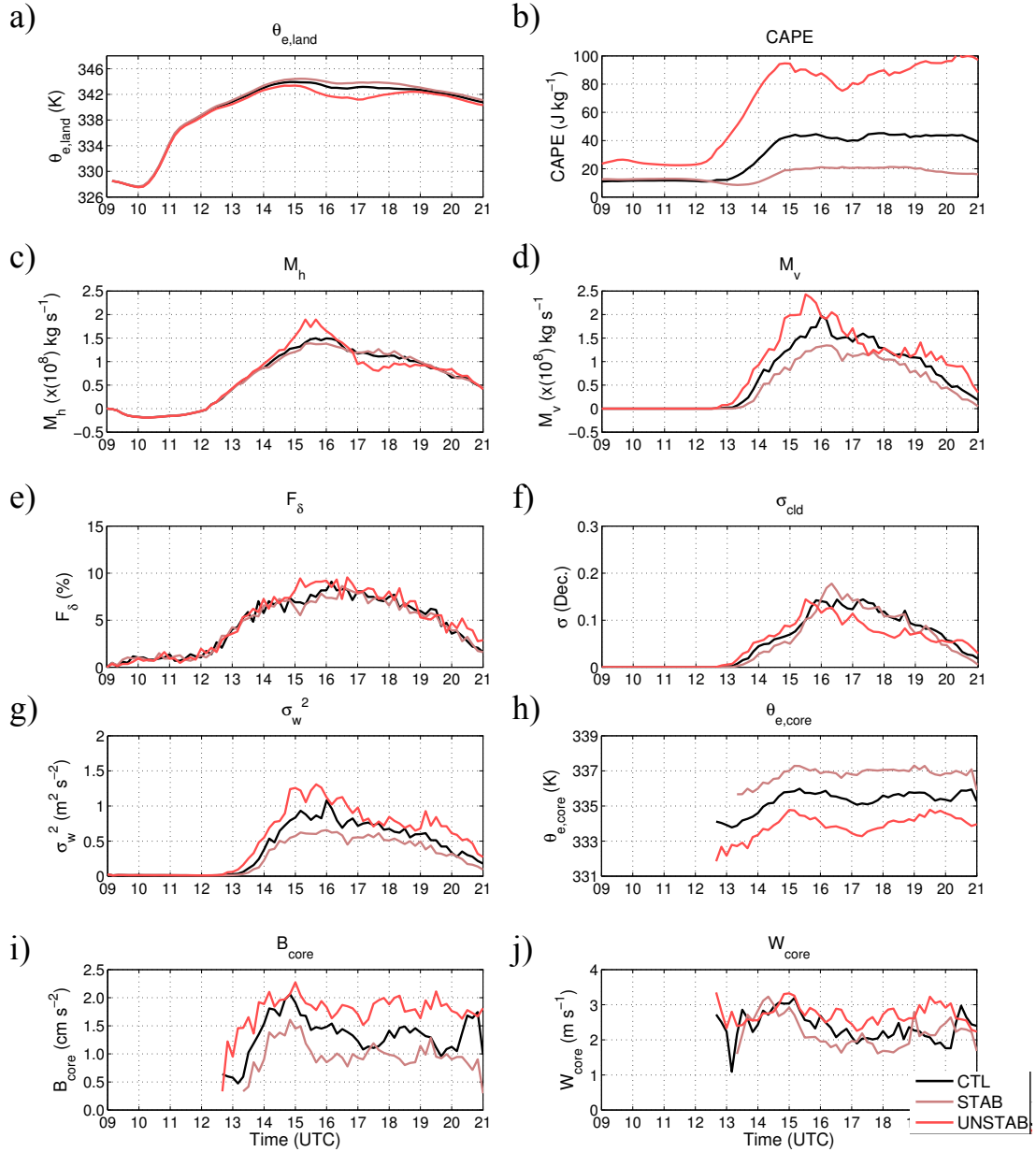


Figure 3.16. Same as in Figure 3.7, but for the cloud-layer moist stability sensitivity tests.

In these simulations, the land surface warms as solar radiation increases (Fig. 3.16a). The island-averaged surface θ_e in the UNSTAB simulation becomes colder than that in the CTL-250E1 and STAB simulations, partially because of its heavier

precipitation (Table 3.7). However, M_h is enhanced by $\sim 20\%$ compared to that in the CTL-250E1 and STAB simulations between 14-16 UTC. This is because the larger CAPE in this simulation enhances B_{core} and leads to greater W_{core} (Figs. 3.16b, i, and j). Stronger cloud-core updrafts not only enhance σ_{cld} and σ_w^2 by 20-30% (Figs. 3.16f-g), but they also give rise to more vigorous cumulus convection as indicated by a same percentage increase in M_v (Figs. 3.16d). As a result, latent-heat release over the island increases and a stronger low pressure anomaly is induced, which in turn strengthens the thermal circulations (see Section 1.4.2). After 17 UTC, M_h in the UNSTAB simulation becomes smaller than that in the CTL-250E1 and STAB simulations (Fig. 3.16c), likely because the cloud shadowing and precipitation's negative feedbacks have overwhelmed the enhancing effect of cloud latent-heat release. Despite these negative feedbacks, the time-integrated M_h in the UNSTAB simulation is still slightly larger than that in the CTL-250E1 and STAB simulations (Table 3.7).

As discussed in Section 3.3, the weakening of thermal circulations in the CTL-250E1 simulation is perhaps due to the circulations' outflows undergoing a deep stable descent. While making the cloud layer more statically unstable in the UNSTAB simulation triggers more cumulus convection and releases more latent heat over the mountain, it also offsets the stable descent and allows the thermal circulations to spin more easily. Therefore, both mechanisms described above could explain the strengthening of thermal circulations when the cloud layer is more statically unstable.

	CTL-250E1	STAB	UNSTAB
Max. Rainfall (mm)	58.1	51.1	52.4
Avg. Rainfall (mm)	3.5	2.1	4.8
Time-Int. M_h ($\times 10^{12}$ kg)	2.88	2.83	2.94
Time-Int. M_v ($\times 10^{12}$ kg)	2.97	2.18	3.70

Table 3.7. Same as in Table 3.6, but for the cloud-layer static stability sensitivity tests.

Although the island-averaged surface θ_e in the STAB simulation is slightly larger than that in the CTL-250E1 simulation, the thermal circulations in the STAB simulation are $\sim 10\%$ weaker (as indicated by M_h) than those in the CTL-250E1 simulation before 17 UTC. This is because with the reduced CAPE (Fig. 3.16b), the cloud parcels are less buoyant (Fig. 3.16i). As result, fewer and less vigorous cumuli are triggered as indicated by its smaller σ_{cld} and σ_w^2 (Figs. 3.16f-g) and weaker W_{core} and M_v (Figs. 3.16d and j). Since the cumulus convection is less vigorous, there is less cloud latent-heat release over the island. Thus, the low pressure anomaly induced is weaker and does not strengthen the thermal circulations as much as that in the CTL-250E1 simulation. In addition, the weaker thermal circulations in the STAB simulation may also be due to stronger resistance to descend in the more stable cloud layer.

Consistent with the result from Section 3.5, increasing the background moist instability leads to more vigorous cumulus convection, which in turn releases more latent heat and strengthens the thermal circulations. However, the amount of low-level forcing is still the ultimate controlling factor of cumulus convection initiation. As demonstrated on April 15th, cumulus convection was suppressed due the lack of solar heating even though it featured a deep conditionally unstable atmosphere and little convective inhibition. In contrast, ample solar heating induced strong thermal circulations and destabilized air directly over the island on the 18th and 19th, thus widespread island convection developed in spite of a fairly stable atmosphere.

Section 3.7 Heat-engine theory

In Chapter 2, we estimated the strength of thermal circulation during each the four DOMEX weak wind cases by applying the FWL surface and WKA upstream sounding observations to the heat-engine theory. The results indicated that since the non-adiabatic temperature difference before 15 UTC was the greatest on the 18th, the estimated thermal circulation strength was also the strongest. However, we made some gross assumptions to make the calculation possible, one of them being the island mixed-layer height was assumed to be a constant (1 km). A more reliable application of the theory and comparison of thermal circulation strength may be obtained from numerical simulations. Numerical simulations not only enable us to derive a more realistic mixed-layer height, but they also allow us to verify the heat-engine theory's ability to predict the thermal circulation strength and sensitivities by directly comparing the boundary-layer updraft speed diagnosed from the simulations to that predicted from the heat-engine theory.

Because the heat-engine theory strictly applies in a "dry" atmosphere, we turned off the microphysics parameterization in all of the numerical simulations in this experiment. Thus, the NOMP simulation discussed in Section 3.5 readily serves as a useful simulation for the validation of heat-engine theory. Since we also wish to test the heat-engine theory's capability to capture the thermal circulation's sensitivity to terrain height, we performed a second simulation (THNOMP) using the same flat island as in the TH simulation.

Because our simulations are in 3-D over a complicated island terrain, some care is required to obtain a bulk estimate of island thermal circulation strength. To obtain these quantities, we first interpolated the model data onto forty vertical cross-sections oriented

across Dominica's long axis (Fig. 3.17). The vertical cross-sections are each separated by 1 km for a total along-ridge distance of 40 km, covering the central part of the island. Each cross-section is 40 km long with a horizontal grid spacing equal to that of the simulation's grid spacing (here 250 m). To obtain 1-D variables such as the surface air temperature, surface water vapor mixing ratio, and terrain height along the cross-sections, we simply extracted the values from the nearest model grid point. To obtain 2-D variables such as the vertical velocities along the cross-sections, we first extracted vertical velocity profiles from the nearest horizontal model grid points, then vertically interpolated the data onto a uniform grid consisting of 80 evenly-spaced vertical levels from 80 m to 6400 m above sea-level.

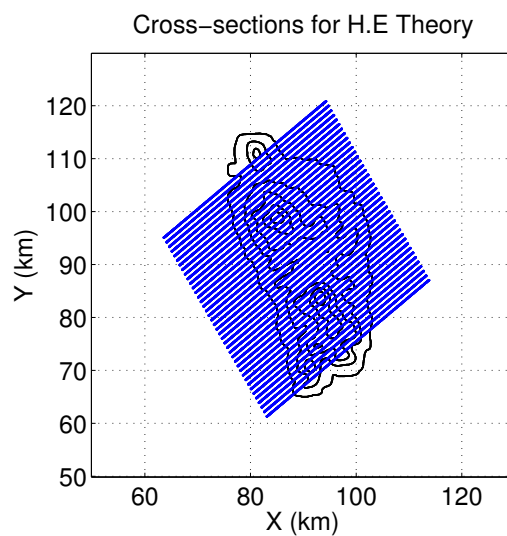


Figure 3.17. Locations of vertical cross-sections for the simulated circulation strength diagnosis. There are forty vertical cross-sections across Dominica and each of them is rotated to be roughly perpendicular to Dominica's terrain angle ($\sim 120^\circ$).

For the mixed-layer height, we first obtained a virtual potential temperature profile at each point and calculated the square of Brunt-Vaisala frequency at a model level as

$$N^2 = \frac{g}{\theta_{v,0}} \frac{\Delta\theta_v}{\Delta Z} \quad (3.1)$$

where g is the gravitational acceleration, $\theta_{v,0}$ is the virtual potential temperature at the first model level, $\Delta\theta_v$ is the virtual potential temperature difference between the model level and the level above, and ΔZ is the distance separating the two model levels. The virtual potential temperature is nearly constant within a well-mixed boundary layer, thus N^2 is ~ 0 . We defined the lowest model level where N^2 exceeds $2.5 \times 10^{-5} \text{ s}^{-2}$ as the mixed-layer top. The average mixed-layer height above the island (elevation $> 1 \text{ m}$) was then calculated for each cross-section.

To diagnose the thermal circulation strength from each cross-section, we first found the maximum vertical velocity in the column above each point from the lowest level up to the cross-section's mean mixed-layer height. The maximum vertical velocity out of all columns along the cross-section was then taken the circulation strength for that cross-section (Fig. 3.18). Finally, we averaged the circulation strength along all cross-sections to obtain the island thermal circulation strength.

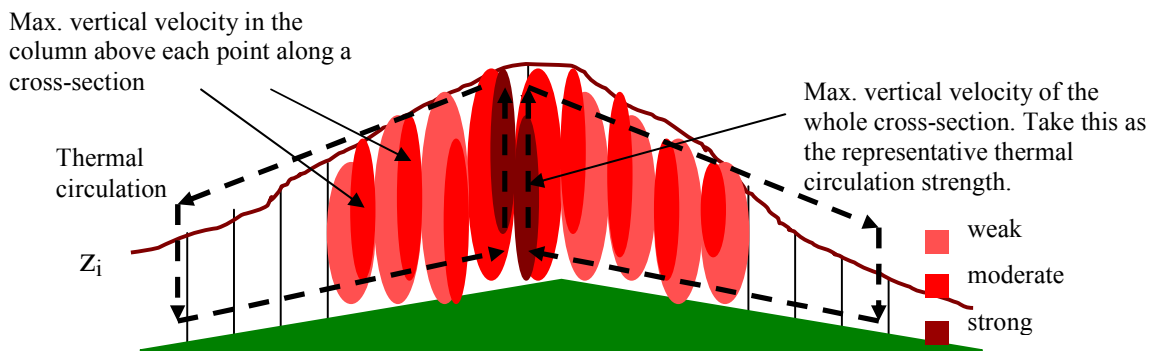


Figure 3.18. A schematic diagram of representative thermal circulation strength diagnosis from the simulation. The maximum vertical velocity along all cross-sections are then averaged to get a mean circulation strength over the island.

To compute the thermal circulation strength from the heat-engine theory (Eq. 2.4), we need the non-adiabatic temperature (T_{NA}) and water vapor mixing ratio (q_v) difference between the land and ocean, averaged surface air temperature of the land and ocean (\bar{T}_{SFC}), and the mixed-layer height (z_i) above the island. We first found the non-adiabatic temperature for all points along each cross-section by extrapolating the surface air temperature dry-adiabatically down to sea-level. The location of maximum T_{NA} above the island along each cross-section was then found. To avoid local extremes, the maximum T_{NA} over the island was determined by spatially-averaging the T_{NA} within 1 km to the left and right of the maximum. For T_{NA} over the ocean, we averaged the T_{NA} for all ocean points along each cross-section. To find q_v over the island, q_v within 1 km to the left and right of the T_{NA} maximum were averaged. To find the q_v over the ocean, q_v above all ocean points along each cross-section were averaged. For \bar{T}_{SFC} along each cross-section, we first smoothed the surface air temperature (T_{SFC}) at the T_{NA} maximum as described above to obtain the island T_{SFC} . We then averaged the island T_{SFC} with the averaged ocean T_{SFC} to get \bar{T}_{SFC} . ℓ_h was determined arbitrarily by finding the distance from the location of maximum T_{NA} to the nearest coastline along each cross-section. We applied the quantities calculated above to two forms of Eq. 2.4: the first ($W_{T,moist}$) considers both the T_{NA} and q_v difference between land and ocean and the second ($W_{T,dry}$) neglects the contribution of Δq_v term to W_T .

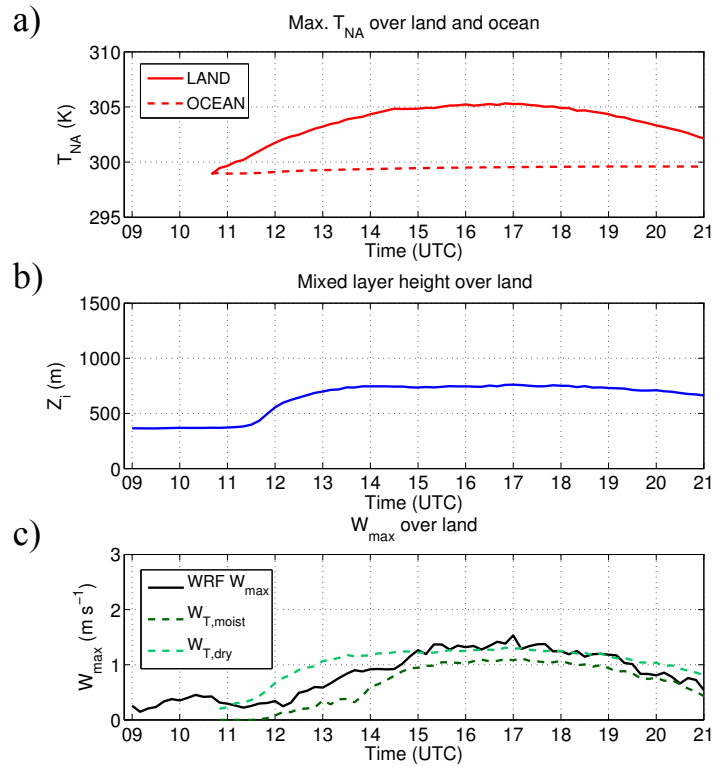


Figure 3.19. a) Simulated maximum T_{NA} for land and ocean, b) simulated island-averaged mixed-layer height, and c) simulated island thermal circulation strength (W_{max}) vs. heat-engine theory predicted thermal circulation strength ($W_{T,dry}$ and $W_{T,moist}$) from the NOMP simulation.

Figure 3.19 shows the averaged non-adiabatic temperatures over the island and ocean, the averaged mixed-layer height over the island, and the island-averaged heat-engine predicted vs. simulated circulation strength from the NOMP simulation. The diurnal variation of the predicted W_T agrees well with the simulation. As the air temperature above the island warms, the island mixed layer height also grows (Figs. 3.19a-b). Whereas $W_{T,dry}$ appears to agree with the simulation throughout the day (Fig. 3.19c), $W_{T,moist}$ slightly underestimates the circulation strength by $\sim 0.2 \text{ m s}^{-1}$ after 15 UTC.

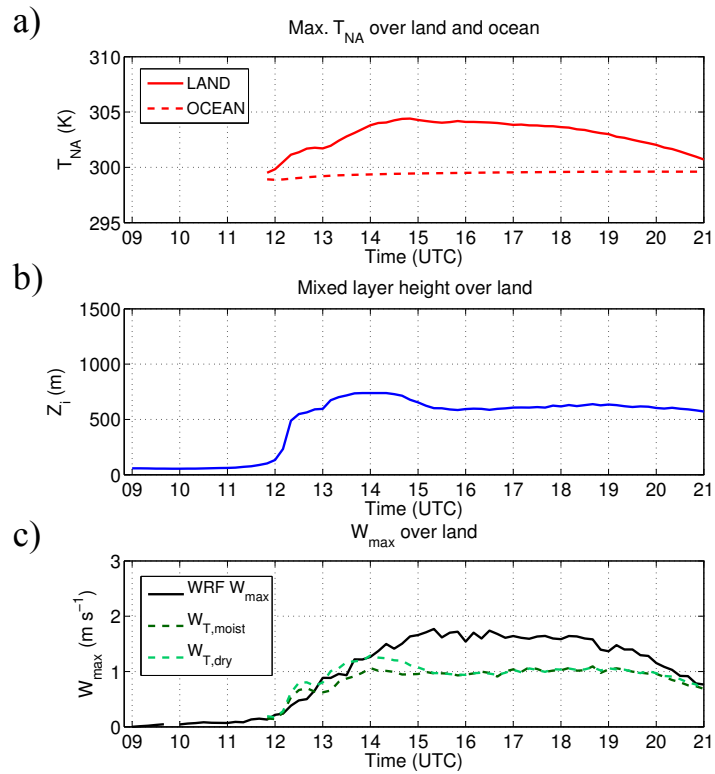


Figure 3.20. Same as in Figure 3.19, but for the THNOMP simulation.

In the THNOMP simulation, heat-engine theory underestimates the circulation strength by $\sim 0.6 m s^{-1}$ for both the dry and moist forms of Eq. 2.4 (Fig. 3.20c). $W_{T,dry}$ and $W_{T,moist}$ appear nearly identical after 15 UTC because the seabreeze fronts in this simulation have converged (Fig. 3.21), which suggests that oceanic moisture has engulfed the whole island and thus the island-ocean q_v difference has become negligible.

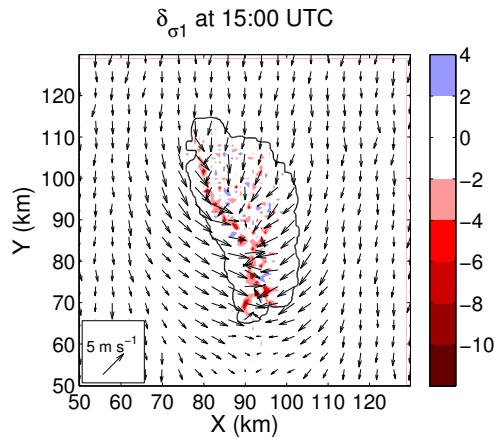


Figure 3.21. First model level horizontal winds, flow divergence, and cloud liquid water path from the THNOMP simulation at 15 UTC. Note that since the microphysics parameterization has been turned off, no cloud is produced. Also note that the seabreeze fronts have converged by this time.

Comparing Fig. 3.20c to Fig. 3.19c, the simulated boundary-layer updraft intensifies as the terrain height is reduced. This is consistent with the results from Section 3.3 where we attributed the weakening of thermal circulations in the CTL-250E1 simulation to the deep stable layer descent above the island. However, it disagrees with Tian and Parker (2003) where the boundary-layer updrafts intensified as the terrain height increased (in both numerical simulations and heat-engine theory). This is likely because the elevated outflows were confined within the mixed layer in their simulations, thus the circulations exhibited minimal stable layer descent.

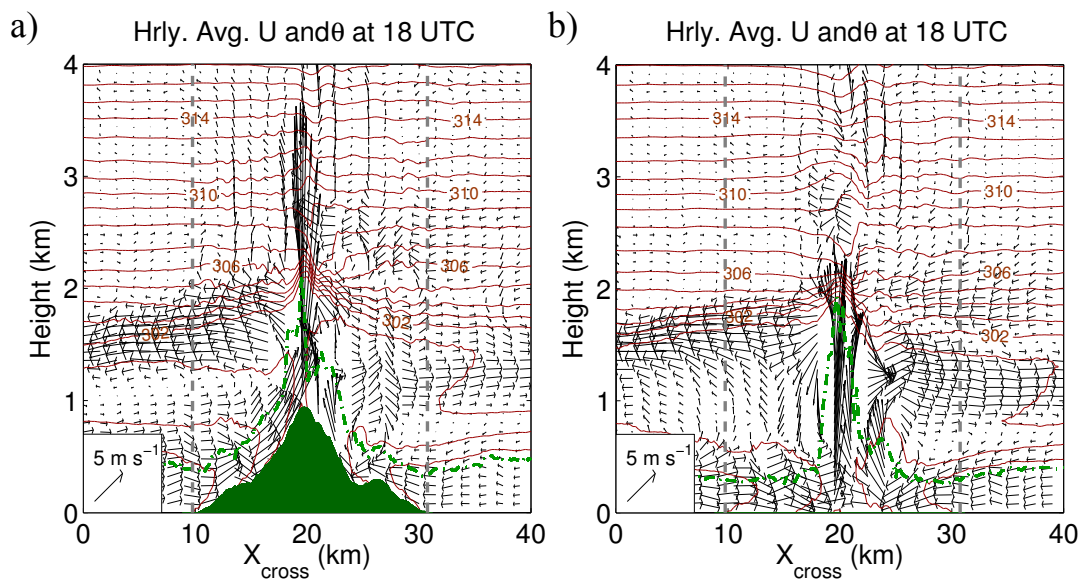


Figure 3.22. Perturbation winds from the initial time and potential temperature along one of the cross-sections from the a) NOMP and b) THNOMP simulations. The horizontal component of the winds along the cross-section is the horizontal winds at the nearest model grid points projected onto the cross-section. The green dashed line denotes the mixed layer height and the grey dashed lines mark the locations of coastlines.

Figure 3.22 shows the perturbation winds from the initial time and potential temperature along one of the cross-sections from the NOMP and THNOMP simulations at 18 UTC. In both simulations, the ascending branch of thermal circulation penetrates

well into the stable free-atmosphere (as denoted by the tightly packed potential temperature contours), thus the elevated outflows are slowed. However, the depth of stable descent above the mixed layer is reduced over a flat terrain, thus the circulations spin more freely in the THNOMP simulation than those in the NOMP simulation (Figs. 3.22a-b). This perhaps explains why the heat-engine theory severely underestimates the circulation strength in the THNOMP simulation, as it assumes that the entire thermal circulation is confined within the mixed layer. Another possible cause for the weaker W_T in the NOMP case might be due to the strongest updrafts are distributed over the highest peaks as discussed in Section 3.3, thus taking the average across the island would yield a weaker thermal circulation.

Chapter 4. Conclusion

Despite numerous studies of thermally-driven convection over islands and mountains separately, few studies have considered their combined effects, thus the thermal circulations and their associated convection are poorly understood. To improve the understanding of thermally-driven convection, we exploited the data collected during the 2011 DOMEX field campaign which took place over the island of Dominica from April to May, 2011. Previous DOMEX studies have found that thermally-driven convection is favored over Dominica when the trade-wind speed falls below 5 m s^{-1} , but they did not analyze the dynamics of those cases in detail. Therefore, we analyzed in detail the observations of four DOMEX weak trade-wind days.

The observational analysis suggested that the amount of solar heating incident over the island is the dominant controlling factor of cumulus convection. Since direct

measurement of the thermal circulation strength was not performed during the four DOMEX cases, we estimated the thermal circulation strength using heat-engine theory (Souza et al., 2000). Because Dominica's surface received abundant solar heating during the mornings of April 18th and 19th, a large land-ocean temperature contrast developed. As a consequence, the heat-engine theory predicted stronger updrafts over the island for these two days. The aircraft and satellite observations also confirmed vigorous island cumulus convection formed during these days.

During April 15th and 21st, large-scale cover in the morning blocked the solar radiation and reduced the surface heating, hence little convection developed over the island during the research flights. Background static instability appeared to have little control on the convection vigor, since only isolated convection formed on the 15th despite a very moist and conditionally unstable atmosphere and little convective inhibition. The stronger background winds, while was still too weak to trigger mechanically-forced convection, may also have inhibited the convection on this day by advecting the temperature anomalies downwind.

To learn more about the dynamics of island convection, we performed cloud-resolving numerical simulations of the April 18th event using the WRF model. We chose this day for the simulations because it featured the strongest solar heating and most intense island convection. Four control simulations at different grid resolutions (1-km, 500-m, 250-m, and 125-m) were performed. The simulated surface conditions and flight track cloud parameters were compared to those observed during April 18th. The simulations suggest that a horizontal grid spacing of < 250 m was required to realistically represent the island convection. However, some model-observation disagreements

remained at this grid resolution. For instance, the simulated convection produced too much rainfall over the island likely due to errors in the microphysics or land-surface parameterization. In addition, the simulated vertical velocity variances along WKA Legs 3 and 4 were too weak possibly because of the errors in the location of the simulated convection and/or reduced surface heating due to the overly heavy simulated rainfall. The horizontal winds extrapolated along Legs 3 and 4 from the model also showed that the simulated elevated outflows were too weak compared to the observations, which might be due to overly high simulated cloud tops causing the main outflow layer to rise above the flight level. Although the simulations did not quantitatively agree with the observations in all respects, the simulations with grid spacing < 250 m agreed the best with both surface and aircraft observations. Thus, we used these simulations for a set of sensitivity experiments to quantify the impacts of various processes on the thermal convection.

The first set of sensitivity experiments quantified the individual contribution of surface thermal forcing and mechanical forcing to the island convection. While the results confirmed that mechanical forcing had little contribution on convection initiation on the 18th because the background winds were too weak to ascend the island's terrain, they also suggested that orography does not necessary enhance the thermal circulations in contrast to previous studies. We attributed this apparent weakening of thermal circulations over a mountainous island to the higher elevations, which caused their outflow to extend well into the free atmosphere. The stronger stability within this layer suppressed the descending outflow above the mountain crest, which weakened the whole circulation. The cumulus convection in the mountain case, however, was $\sim 30\%$ more

vigorous (in terms of the time-integrated vertical cloud mass flux) than that in the flat island case. This may have arisen from individual mountain peaks acting as local convergence zones where cumuli can readily initiate.

The second set of experiments quantified the impacts of wind velocity. We found that larger wind speeds and/or stronger cross-barrier wind components act to substantially reduce the circulation strength and associated convection intensity. These results confirmed the findings from previous studies (e.g Crook, 2001) that thermally-driven updrafts tend to weaken if air parcels spend less time over a heated surface. For similar reasons, the cumulus clouds were also less buoyant and vigorous under these situations.

In our third set of sensitivity tests, we quantified the feedbacks of various microphysical and radiative processes including cloud shadowing, precipitation, and latent-heat release within the cloud layer. While precipitation created cold pools that initially enhanced the cumulus convection, the convection eventually weakened as the cold air reduced the surface thermal forcing. In the absence of rain, both the thermal circulations and cumulus convection strengthened by ~10% compared to the control simulation. Turning off the cloud's effect on optical depth enhanced the thermal circulations by ~20% compared to the control simulation despite the rainfall nearly doubled. The vertical cloud mass flux also increased because 1) the clouds no longer shade the surface, thus they maintained their vigor as the air underneath remained warm and 2) more outflow boundaries were created to enhance the surface flow (not upslope flow) convergence. Eliminating cloud shadowing and precipitation altogether further increased the circulation strength and cumulus vigor. In addition, cloud shadowing appeared to have a greater negative feedback on the thermal circulations than

precipitation. Lastly, cloud latent-heat release appeared to enhance the thermal circulations since the island-scale horizontal mass flux was $\sim 15\%$ larger than that in a simulation with cloud microphysics turned off.

The final set of experiments evaluated the effects of cloud-layer stability on the thermal circulations. Nearly tripling the CAPE increased the island-scale horizontal mass flux by $\sim 20\%$ before the cloud shadowing and precipitation feedbacks weakened the island circulations. The strengthening of thermal circulation may be attributed to two processes: the first is associated with the greater latent-heat release by the more vigorous cumulus convection triggered, and the second relates to the reduced stable cloud layer descent of elevated outflows. In contrast, the island-scale horizontal mass flux and vertical cloud mass flux were reduced by $\sim 10\%$ and $\sim 25\%$ respectively when we reduced the CAPE by approximately a factor of 5.

The heat-engine theory's ability to predict the thermal circulation strength was verified using the results from two convection-inhibiting numerical simulations. The theory appeared to adequately estimate the circulation strength over a heated mountain. However, it performed poorly over a flat island. The error may have arisen from the assumption that the entire circulation was contained within the mixed layer, which neglected the stable descent above this layer. Over taller islands, the circulations extended deeper into the stable layer, which increased the degree of elevated stable descent over the island. This effect appeared strong enough to counter the tendency for mountains to generate stronger thermal circulations through their enhanced baroclinicity.

Appendix

A1. Island-scale divergence

The island scale divergence is defined as the averaged divergence over the island surface. By the divergence theorem, it is also equal to outflux of mass across the island perimeter (e.g., Geerts et al., 2008). The island parameter, s , is defined as its 1-m elevation contour (Fig. A1).

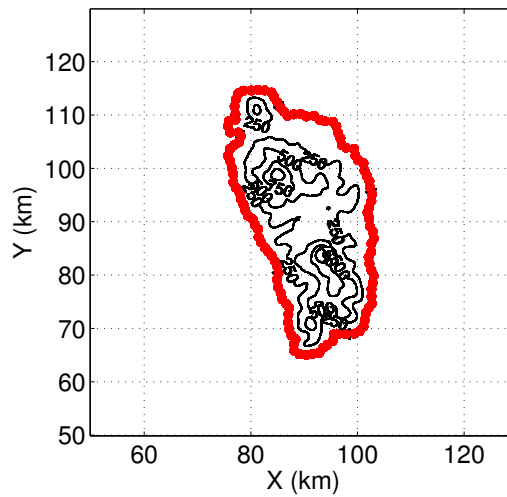


Figure A1. Dominica's 1-m elevation contour as represented in the simulations (filled red circles). Higher elevations are plotted in 250-m contours.

Before computing this quantity, we need the horizontal winds along the perimeter. To obtain these, we first perform a 2-D linear interpolation of the horizontal wind profiles to the points along the perimeter (Fig. A2). We then average the horizontal winds at two consecutive points along the perimeter to obtain the winds at the midpoint in between these points.

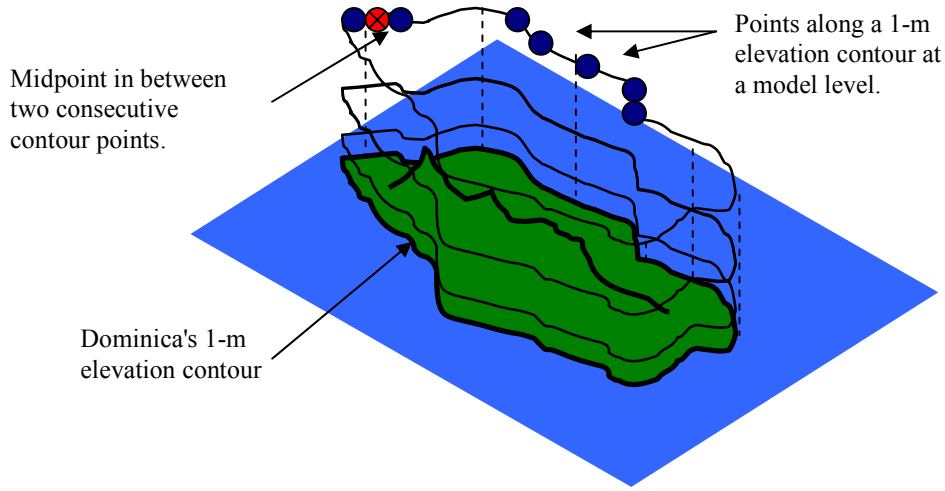


Figure A2. A schematic illustration of the 1-m elevation contours at every model level above Dominica. The blue circles denote the points along the island's perimeter in which the simulated horizontal winds are extracted onto. The red circle marks the midpoint between two consecutive contour points.

We then apply the divergence theorem (e.g Holton, 2004) to compute the island-scale divergence at each model level:

$$\delta = -\nabla \cdot \mathbf{v} = \frac{1}{A} \oint_s (\mathbf{v} \cdot \hat{\mathbf{n}}) ds \quad (\text{A1})$$

where \mathbf{v} is the horizontal wind vector, A is the area of Dominica ($\sim 7.50 \times 10^8 \text{ m}^2$), ds is the distance along the perimeter, and $\hat{\mathbf{n}}$ is the unit vector of normal to the perimeter (pointing outward from the island). Positive δ indicates flow divergence out of the island's perimeter. Conversely, negative δ indicates flow convergence into the island's perimeter. Thus, we expect the near-surface δ to be < 0 as daytime thermally-driven flows develop over Dominica.

A2. Vertically-integrated horizontal mass flux

The vertically-integrated horizontal mass flux (M_h) is the total horizontal mass flux into the island's perimeter below the lowest level of non-divergence. To obtain this quantity, we first apply the same procedures described in Section A1 to get the air density

and horizontal wind profiles at all points along the perimeter. The air density and horizontal winds profiles along the contour are then linearly interpolated onto 56 evenly-spaced levels from 100 m to 5600 m above sea-level.

Because daytime thermal circulations produce flow convergence at low-levels and divergence aloft, we vertically-integrate the horizontal mass flux from the first level up to the lowest level of non-divergence (the lowest level at which δ switches signs) to obtain a total horizontal mass flux into the island. Therefore, the overall calculation for this quantity is given by:

$$M_h = \int_{Z_0}^{Z_{\delta 0}} \left(\oint_s \rho (\mathbf{v} \cdot \hat{\mathbf{n}}) ds dh \right) \quad (\text{A2})$$

where Z_0 is the lowest interpolation level, $Z_{\delta 0}$ is the lowest level of non-divergence, ρ is the air density, and dh is the vertical distance between two levels. This quantity is proportional to the negative of island-scale divergence described in A1. If there is an island-scale divergence, then the horizontal mass flux is negative. Conversely, if there is an island-scale convergence, then the horizontal mass flux is positive.

A3. Integrated vertical cloud mass flux

The integrated vertical cloud mass flux (M_v) is the integrated vertical mass flux for all horizontal model grid points where the cloud water mixing ratio (q_c) is $> 0.1 \text{ g kg}^{-1}$, above land (elevation $> 1 \text{ m}$), and rising ($w > 0 \text{ m s}^{-1}$). To obtain this quantity at the WKA flight level (1800 m), we first linearly interpolate the vertical velocity, cloud water mixing ratio, and air density to a height of 1800 m. The vertical mass flux at a model grid point is given by:

$$M_{\text{vert.}} = \rho w dx dy \quad (\text{A3})$$

where ρ is the air density, w is the vertical velocity, and dx and dy are the model grid spacings in x - and y -dimensions, respectively. Finally, we integrate the vertical mass flux at all points that meet the definition of a rising cloud and to obtain M_v . M_v is typically positively correlated with M_h since the mass converging into the island's perimeter rises and triggers cumulus convection. M_v is also often slightly greater than M_h since clouds entrain surrounding air within the cloud layer.

Bibliography

- Abe, S. and T. Yoshida (1982): The effects of the width of a peninsula to the sea breeze, *J. Meteo. Soc. Japan*, 60, 1074-1084
- Aitkinson, B. W. (1981): *Meso-scale atmospheric circulations*, Academic Press, London
- Arritt, R. W. (1993): Effects of large-scale flow on characteristic features of the sea breeze, *J. App. Meteo.*, 32, 116-125
- Banta, R. M. (1984): Daytime boundary-layer evolution over mountainous terrain, Part I: observations of dry circulations, *Mon. Wea. Rev.*, 112, 340-356
- (1986): Daytime boundary-layer evolution over mountainous terrain. Part II: Numerical studies of upslope flow duration, *Mon. Wea. Rev.*, 114, 1112-1130
- (1990): Atmospheric processes over complex terrain, *Meteo. Mono.*, 23, Amer. Meteo. Soc.
- Barthlott, C., R. Burton, D. J. Kirshbaum, K. Hanley, E. Richard, J.-R. Chaboureau, J. Trentmann, B. Kern, H.-S. Bauer, T. Schwitalla, C. Keil, Y. Seity, A. Gadian, A. Blyth, S. Mobbs, C. Flamant, and J. Handwerker (2011): Initiation of deep convection at marginal instability in an ensemble of mesoscale models: a case-study from COPS, *Q. J. R. Meteorol. Soc.*, 137, 118-136
- , and D. J. Kirshbaum (2013): Sensitivity of deep convection to terrain forcing over Mediterranean islands, *Q. J. R. Meteorol. Soc.*, 139, 1762-1779
- Blyth, A. M. (1993): Entrainment in cumulus clouds, *J. App. Meteo.*, 32, 626-641
- Bohren, C. and B. Albrecht (1998): *Atmospheric thermodynamics*, Oxford University Press
- Bryan, G. H., J. C. Wyngaard, and J. M. Fritsch (2003): Resolution requirements for the simulation of deep moist convection, *Mon. Wea. Rev.*, 131, 2394-2416
- Caracena, F., R. A. Maddox, L. R. Hoxit, and C. F. Chappell (1979): Mesoanalysis of the Big Thompson storm, *Mon. Wea. Rev.*, 107, 1-17
- Carbone, R. E., W. A. Cooper, and W.-C. Lee (1995): Forcing of flow reversal along the windward slopes of Hawaii, *Mon. Wea. Rev.*, 123, 3466-3480
- , J. W. Wilson, T.D. Keenan, and J. M. Hacker (2000): Tropical island convection in the absence of significant topography. Part I: Life cycle of diurnally forced convection, *Mon. Wea. Rev.*, 128, 3459-3480
- Chen, Y.-L. and A. J. Nash (1994): Diurnal variation of surface airflow and rainfall frequencies on the island of Hawaii, *Mon. Wea. Rev.*, 122, 34-56
- , and J.-J. Wang (1995): The effects of precipitation on the surface temperature and airflow over the island of Hawaii, *Mon. Wea. Rev.*, 123, 681-694

- Crook, N. A. (2001): Understanding Hector: The dynamics of island thunderstorm, *Mon. Wea. Rev.*, 129, 1550-1563
- Damiani, R., J. Zehnder, B. Geerts, J. Demko, S. Haimov, J. Petti, G. S. Poulos, A. Razdan, J. Hu, M. Leuthold, and J. French (2008): The cumulus, photogrammetric, in situ, and Doppler observations experiment of 2006, *Bull. Amer. Meteor. Soc.*, 89, 57-73
- Demko, J. C., B. Geerts, Q. Miao, and J. A. Zehnder (2009): Boundary-layer energy transport and cumulus development over a heated mountain: An observational study, *Mon. Wea. Rev.*, 137, 447-468
- de Rooy, W. C., P. Bechtold, K. Frohlich, C. Hohenegger, H. J. J. Jonker, D. Mironov, A. P. Siebesma, J. Teixeira, and J.-I. Yano (2013): Review Article entrainment and detrainment in cumulus convection: an overview. *Q. J. R. Meteorol. Soc., Royal Meteor. Soc.*, 139, 1-19
- DOMEX webpage: The DOMinica EXperiment: Orographic Precipitation in the Tropics: <http://www.domex2011.com/home>
- Dominica Meteorological Service: Monthly Agro-Meteorological Bulletin April 2013, retrieved from: http://www.weather.gov.dm/agro_bulletin.php on November 2013
- Doyle, J. D. and D. R. Durran (2002): The dynamics of mountain-wave-induced rotors, *J. Atmos. Sci.*, 59, 186-201
- Frame, J., P. Markowski (2013): Dynamical influences of anvil shading on simulated supercell thunderstorms, *Mon. Wea. Rev.*, 141, 2802-2820
- Geerts, B., Q. Miao, and J. C. Demko (2008): Pressure perturbations and upslope flow over a heated, isolated mountain, *Mon. Wea. Rev.*, 136, 4272-4288
- Hagen, M., J. van Baelen, and E. Richard (2011): Influence of the wind profile on the initiation of convection in mountainous terrain, *Q. J. R. Meteorol. Soc.*, 137, 224-235
- Hanley, K. E., D. J. Kirshbaum, S. E. Belcher, N. M. Roberts, and G. Leoncini (2011): Ensemble predictability of an isolated mountain thunderstorm in a high-resolution model, *Q. J. R. Meteorol. Soc.*, 137, 2124-2137
- Heus, T., G. van Dijk, H. J. J. Jonker, and H. van den Akker (2008): Mixing in shallow cumulus clouds studied by Lagrangian particle tracking, *J. Atmos. Sci.*, 65, 2581-2597
- Holton, J. R. (2004): An introduction to dynamic meteorology, fourth edition, International Geophysics Series, 88, Elsevier

- Houze Jr., R. A. and P. V. Hobbs (1982): Organization and structure of precipitating cloud systems, *Adv. Geophys. Sci.*, Academic Press Inc.
- (1993): *Cloud dynamics*, Academic Press, San Diego
- (2012): Orographic effects on precipitating clouds, *Rev. Geophys.*, 50, RG1001
- Jiang, Q. (2003): Moist dynamics and orographic precipitation, *Tellus*, 55A, 301-316
- Johnson, R. H., P. E. Ciesielski, T. S. L'Ecuyer, and A. J. Newman (2008): Diurnal cycle of convection during the 2004 North American Monsoon Experiment, *J. of Climate*, 23, 1060-1078
- Kirshbaum, D. J. and R. B. Smith (2009): Orographic precipitation in the tropics: Large-eddy simulations and theory, *J. Atmos. Sci.*, 66, 2559-2578
- , and A. L. M. Grant (2012): Invigoration of cumulus cloud fields by mesoscale ascent, *Q. J. R. Meteorol. Soc.*, 138, 2136-2150
- (2013): On thermally forced circulations over heated terrain, *J. Atmos. Sci.*, 70, 1690-1703
- , and C.-C. Wang (2014): Boundary layer updrafts by airflow over heated terrain, *J. Atmos. Sci.*, 71, 1425-1442
- Leopold, L. B. (1949): The interaction of trade wind and seabreeze, Hawaii, *J. of Meteo.*, 6, 312-320
- Lin, Y.-L., (2007): *Mesoscale Dynamics*, Cambridge University Press
- Maddox, R. A., L. R. Hoxit, C. F. Chappell, and F. Caracena (1978): Comparison of meteorological aspects of the Big Thompson and Rapid City Floods, *Mon. Wea. Rev.*, 106, 375-389
- Mahrer, Y. and R. A. Pielke (1977): The effects of topography on sea and land breezes in a two-dimensional numerical model, *Mon. Wea. Rev.*, 105, 1151-1162
- Markowski, P. and Y. Richardson (2010): *Mesoscale meteorology in mid-latitudes*, Wiley-Blackwell, R. Meteo. Soc.
- Miglietta, M. M. and P. Rotunno (2012): Application of theory to simulations of observed cases of orographically forced convection rainfall, *Mon. Wea. Rev.*, 140, 3039-3052
- Miller, S. T. K., B. D. Keim, R. W. Talbot, and H. Mao (2003): Sea breeze: structure, forecasting, and impacts, *Rev. Geophys.*, 41, 1-131
- Minder, J. R., R. B. Smith, and A. D. Nugent (2013): The dynamics of ascent-forced orographic convection in the tropics: Results from Dominica, *J. Atmos. Sci.*, 70, 4067-4088

- Morton, B. R., Sir J. Taylor, F. R. S., and J. S. Turner (1956): Turbulent gravitational convection from maintained and instantaneous sources, *Proc. R. Soc. Lond. A.* 234
- Neumann, J. and Y. Mahrer (1971): A theoretical study of the land and sea breeze circulation, *J. Atmos. Sci.*, 28, 532-542
- Nguyen H. V., Y.-L. Chen, and F. Fujioka (2010): Numerical simulations of island effects on airflow and weather during the summer over the island of Oahu, *Mon. Wea. Rev.*, 138, 2253-2280
- Paluch, I. R. (1979): The entrainment mechanism in Colorado cumuli, *J. Atmos. Sci.*, 36, 2467-2478
- Purdum J. F. W. and J. G. Gurka (1974): The effect of early morning cloud cover on afternoon thunderstorm development, *Fifth Conference on Weather Forecasting and Analysis*, St. Louis, Amer. Meteo. Soc., 58-60
- Qian, T., C. C. Epifiano, and F. Zhang (2012): Topographic effects on the tropical land and sea breeze, *J. Atmos. Sci.*, 69, 130-149
- Raymond D. and M. Wilkening (1980): Mountain-induced convection under fair weather conditions, *J. Atmo. Sci.* 37, 2693-2706
- Robinson, F. J., M. D. Patterson, and S. C. Sherwood (2013): A numerical modeling study of the propagating of idealized sea-breeze density currents, *J. Atmos. Sci.*, 70, 653-668
- Rogers, R. R. and M. K. Yau (1989): *A short course in cloud physics*, 3rd E., Butterworth Heinemann
- Rotunno, R., and R. Ferretti (2001): Mechanisms of intense Alpine rainfall, *J. Atmos. Sci.*, 58, 1732-1749
- (2003): Orographic effects on rainfall in MAP cases IOP2b and IOP8, *Q. J. R. Meteorol. Soc.*, 129, 373-390
- Ruppert, J. H., R. H. Johnson, and A. K. Rowe (2013): Diurnal circulations and rainfall in Taiwan during SoWMEX/TiMREX (2008), *Mon. Wea. Rev.*, 141, 3851-3872
- Savijarvi, H. and S. Matthews (2004): Flow over small heated islands: A numerical sensitivity study, *J. Atmos. Sci.*, 61, 859-868
- Segal, M., J. F. W. Purdom, J. L. Song, R. A. Pielke, and Y. Mahrer (1986): Evaluation of cloud shading effects on the generation and modification of mesoscale circulations, *Mon. Wea. Rev.*, 114, 1201-1212

- , R. Avissar, M. C. McCumber, and R. A. Pielke (1988): Evaluation of vegetation effects on the generation and modification of mesoscale circulations, *J. Atmos. Sci.*, 45, 2268-2292
- Siebesma, A. P., C. S. Bretherton, A. Brown, A. Chlond, J. Cuxart, P. G. Duynkerke, H. Jiang, M. Khairoutdinov, D. Lewellen, C.-H. Moeng, E. Sanchez, B. Stevens, and D. E. Stevens (2003): A large-eddy simulation intercomparison study of shallow cumulus convection, *J. Atmos. Sci.*, 60, 1201-1219
- Skamarock, W. C., J. B. Klemp, J. Dudhia, D. O. Gill, D. M. Barker, M. G. Duda, X.-Y. Huang, W. Wang, J. G. Powers (2008): A description of the advanced research WRF version 3, NCAR Technical Note, National Center for Atmospheric Research, Boulder, CO
- Smith, R. B., P. Schafer, D. J. Kirshbaum, and E. Regina (2009): Orographic precipitation in the tropics: Experiments in Dominica, *J. Atmos. Sci.*, 66, 1698-1716
- , J. R. Minder, A. D. Nugent, T. Storelvmo, D. J. Kirshbaum, R. Warren, N. Lareau, P. Palany, A. James, and J. French (2012): Orographic precipitation in the tropics, The Dominica Experiment, *Bull. Amer. Meteor. Soc.*, 93, 1567-1579
- Smolarkiewicz, P., R. M. Rasmussen, and T. L. Clark (1988): On the dynamics of Hawaiian rainbands: island forcing, *J. Atmos. Sci.*, 45, 1872-1905
- , and R. Rotunno (1989) Low Froude number flow past three-dimensional obstacles. Part I: Baroclinically generated lee vortices, *J. Atmos. Sci.*, 46, 1154-1164
- Souza, E. P., N. O. Renno, and M. A. F. Silva Dias (2000): Convective circulations induced by surface heterogeneities, *J. Atmos. Sci.*, 57, 2915-2922
- Squires, P. (1958): Penetrative downdraughts in cumuli, *Tellus*, 10, 381-389
- , and J. S. Turner (1962): An entraining jet model for cumulo-nimbus updrafts, *Tellus*, 14, 422-434
- Tian, W.-S. and D. J. Parker (2002): Two-dimensional simulation of orographic effects on mesoscale boundary-layer convection, *Q. J. R. Meteorol. Soc.*, 128, 1929-1952
- (2003): A modeling study and scaling analysis of orographic effects on boundary layer shallow convection, *J. Atmos. Sci.*, 60, 1981-1991
- Wanatabe, H. and Y. Ogura (1987): Effects of orographically forced upstream lifting on mesoscale heavy precipitation: a case study, *J. of the Atmos. Sci.*, 44, 661-675
- Wang, Z., P. Wechsler, W. Kuetsner, J. French, A. Rodi, B. Glover, M. Burkhart, and D. Lukens (2009): Wyoming Cloud Lidar: instrument description and applications, *Optic Express*, 17, Opt. Soc. Amer.

Whiteman, C. D. (2000): Mountain meteorology fundamentals and applications, Oxford University Press, New York

World Sea Temperature: data retrieved on November 2013 from
<http://www.seatemperature.org/central-america/dominica/la-plaine-april.htm>

Wyoming Cloud Radar/Lidar webpage: <http://www-das.uwyo.edu/wcr>

University of Wyoming, College of Engineering, Dept. of Atmospheric Sciences,
Weather: <http://weather.uwyo.edu/upperair/sounding.html>, data retrieved on Oct. 2013.

Xian Z. and R. A. Pielke (1991): The effects of width of landmasses on the development of sea breezes, *J. App. Meteo.*, 30, 1280-1304

Yang Y., Y.-L. Chen, F., and M. Fujioka (2005): Numerical simulations of the island-induced circulations over the island of Hawaii during HaRP, *Mon. Wea. Rev.*, 133, 3693-3713

----, and Y.-L. Chen (2008): Effects of terrain heights and sizes on island-scale circulations and rainfall for the island of Hawaii during HaRP, *Mon. Wea. Rev.*, 136, 120-136